AD-A144 449 ASYMPTOTIC ANALYSIS OF OCEAN BOTTOM REFLECTED ACOUSTIC FIELDS(U) WOODS HOLE OCEANOGRAPHIC INSTITUTION MA H KAWAHARA MAY 84 WHOI-84-23 N00014-82-C-0152 1/2

UNCLASSIFIED F/G 20/1 NL

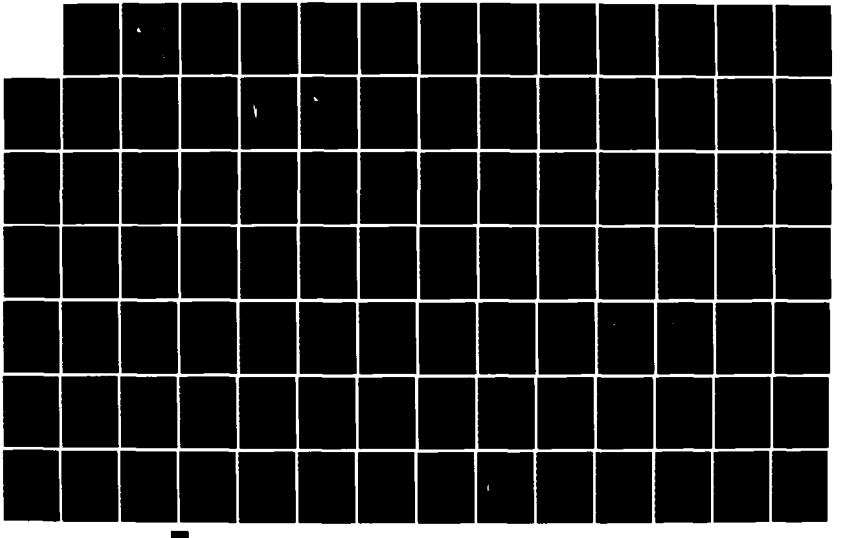

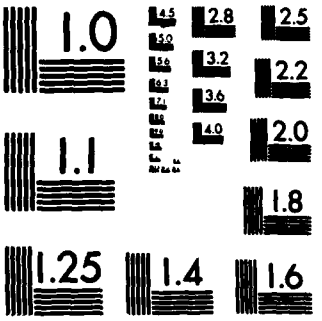

WHOI-84-23

Woods Hole Oceanographic Institution
Massachusetts Institute of Technology

Joint Program in Oceanography and Oceanographic Engineering

DOCTORAL DISSERTATION

Asymptotic Analysis of Ocean Bottom Reflected Acoustic Fields

by

Hiroshi Kawahara

May 1984

WHOI-84-23

Asymptotic Analysis of Ocean Bottom Reflected Acoustic Fields

by

Hiroshi Kawahara

Woods Hole Oceanographic Institution
Woods Hole, Massachusetts 02543

and

The Massachusetts Institute of Technology
Cambridge, Massachusetts 02139

May 1984

Doctoral Dissertation

Funding was provided by the Office of Naval Research under grant Number N00014-82-C-0152.

Approved for Distribution:

Robert C. Spindel, Chairman
Department of Ocean Engineering

Charles D. Hollister
Dean of Graduate Studies

ASYMPTOTIC ANALYSIS OF OCEAN BOTTOM REFLECTED ACOUSTIC FIELDS

by

Hiroshi Kawahara
B.S., 1979 Humboldt State University

SUBMITTED IN PARTIAL FULFILLMENT OF THE REQUIREMENTS FOR THE DEGREE OF DOCTOR OF SCIENCE

at the

MASSACHUSETTS INSTITUTE OF TECHNOLOGY

and the

WOODS HOLE OCEANOGRAPHIC INSTITUTION

May 1984

Signature of Author ..... Hiroshi Kawahara
Department of Ocean Engineering, Massachusetts Institute of Technology and the Joint Program in Oceanography/Oceanographic Engineering, Massachusetts Institute of Technology/Woods Hole Oceanographic Institution, May 1984

Certified by ..... George V. Frisk
George V. Frisk, Thesis Supervisor

Accepted by ..... Ole S. Madsen
Ole S. Madsen, Chairman, Joint Committee for Oceanographic Engineering, Massachusetts Institute of Technology/Woods Hole Oceanographic Institution

Thesis supervisor: George V. Frisk, Associate Scientist
Woods Hole Oceanographic Institution

Asymptotic Analysis of Ocean Bottom Reflected Acoustic Fields

Hiroshi Kawahara

Submitted in partial fulfillment of
the requirements for the degree of
Doctor of Science

at the

MASSACHUSETTS INSTITUTE OF TECHNOLOGY
and the
WOODS HOLE OCEANOGRAPHIC INSTITUTION

May, 1984

ABSTRACT

Pronounced spatial acoustic interference patterns versus horizontal range were observed near the deep ocean bottom from a 220-Hz CW point source also located near the bottom. This is a result of the direct water wave field interacting with a strongly reflected field from the ocean sediments. If the bottom structures are horizontally stratified media, the reflected field can be expressed by the Sommerfeld integral whose integrand is weighted by a total plane wave reflection coefficient.

In this thesis the reflected fields are analytically evaluated in order to understand the physical mechanism of the propagating waves through the bottom layer structure. Based on a canonical geoacoustic model, the Langer uniform asymptotic approximation is applied to evaluate the total plane wave reflection coefficient accurately. Then the Sommerfeld integral is evaluated by the method of steepest descents. The expression for the reflected field is fully analytic and provides physical insight into the understanding of energy partitioning in the sediments. With inclusion of the new method to analytically express a sound velocity profile shape based on measurements, the approximate solution provides a full analytic expression of the reflected field based on a realistic geoacoustic model.

Various geoacoustic models, with emphasis on changes in the shape of the sound velocity profile in the sediment layer, are examined and their parametric dependences on the associated reflected fields are investigated. The conditions neccessary for the shape of the profile to be important are also quantitatively defined and are demonstrated in theoretical data as well as in real data.

To Hiroko and Izumi

with love

ACKNOWLEDGEMENTS

The work discussed in this thesis has been a very exciting project and one which would not have been possible without the help and encouragement of my family, friends, and many great teachers and professionals. I would like to thank all of those who have contributed in one way or another to the completion of this thesis, but in particular I would like to thank the following people for their special contributions: Jim Lynch for editing the primary text of this thesis and his continuous moral support; Bob Spindel for being generous enough to purchase a personal computer for the writing of thesis and for serving as chairman in my thesis defense committee; Mike Wengrovitz for generating numerical results of the total reflected field and total reflection coefficient and for his help using the VAX 11/780 computer; Betsey Pratt for her help with graphics in this thesis; our parents in Japan for their financial and emotional support; Frank Ryan of S.A.I. for providing me with a computer code for Fock functions; Ralph Stephen for his many valuable discussions and for being a member of my thesis committee; Arthur Baggeroer for being my academic advisor at M.I.T. and for being a member of my thesis committee.

I was also very fortunate to be able to discuss philosophical and technical aspects of the problems treated in this thesis with such experts as Profs. Leopold Felsen of Polytechnic Institute of New York, Paul Richards of Columbia University, Keiiti Aki of M.I.T., and particularly Prof. David Stickler of Courant Institute of Mathematical Sciences, and I would like to thank them for their influence and inspiration. Prof. Stickler first suggested to me the application of the Langer uniform asymptotic approximation for computing the acoustic field inside the bottom layer when we were dining in a small Italian restaurant in Greenwich Village during Christmas time of 1982.

My entire academic experience at M.I.T./W.H.O.I. Joint Program was made possible by the continuous support and encouragement of my thesis supervisor George Frisk. Without his expertise and guidance not only this thesis but also other academic requirements in the program would never been completed. To my wife Hiroko, I am grateful for her love and patience, and sharing all of the good times and bad times with me during my years in the program.

Finally, I would like to acknowledge the financial support from the Education Office in Woods Hole Oceanographic Institution and the Office of Naval Research.

TABLE OF CONTENTS

LIST OF IMPORTANT SYMBOLS

$A_0^{(1),(2)}$	$= i\rho_1\gamma_0 W^{(1),(2)}(z = 0)$
$A_H^{(1),(2)}$	$= i\rho_1\gamma_2 W^{(1),(2)}(z = H)$
$B_0^{(1),(2)}$	$= -\rho_0 Q_0 \nu_0^{-1/2} W'^{(1),(2)}(z = 0)$
$B_H^{(1),(2)}$	$= -\rho_2 Q_H \nu_H^{-1/2} W'^{(1),(2)}(z = H)$
α, α_1	Grazing angles in the water column and in the layer at the ocean bottom, respectively
c_0, $c_1(z)$, c_2	Sound velocities in the water column, in the layer and in the basement, respectively
$\eta(z)$	Phase integral defined by $\int_z^z Q(z')\,dz'$ where $Q(z_t) = 0$
η_0, η_H	$\eta(z)$ evaluated at $z = 0$ and $z = H$, respectively
g	Reference sound velocity gradient in the layer
γ_0, γ_2	Vertical slownesses in the water column and in the basement, respectively
H	Depth of the subbottom interface
k_r	Horizontal component of the wave number
λ_1	Wavelength of acoustic signal within the layer
μ	Portion of the ray phase within the layer
$\nu(z)$	$= [3\omega\eta(z)/2]^{2/3}$
ν_0, ν_H	$\nu(z)$ evaluated at $z = 0$ and $z = H$, respectively
ω	Angular frequency of the source
P	Total ocean bottom reflected acoustic field
P_n	Reflected field due to the n-th multiple reflection
p	Horizontal slowness ($k_r = \omega p$)

p_s	Horizontal slowness at a saddle point
p_{sj}	Horizontal slowness at a saddle point for the j-th multiple reflection
p_c	p_s at caustic
ϕ_n	Ray phase for the n-th multiple reflection
$Q(z)$	Vertical slowness in the layer
Q_0, Q_H	$Q(z)$ evaluated at $z = 0$ and $z = H$, respectively
$R(p,\omega)$	Total plane wave reflection coefficient off the ocean bottom
$R_n(p,\omega)$	Partial plane wave reflection coefficient for the n-th multiple reflection
R_{01}	Local plane wave reflection coefficient off the ocean bottom for the incident wave in the water column
R_{12}	Local plane wave reflection coefficient off the subbottom for the incident wave in the layer
r	Horizontal range
ρ_0, ρ_1, ρ_2	Densities in the water column, in the layer and in the basement, respectively
S_U	$= Q_0 \nu_0^{-1/2}$
S_H	$= Q_H \nu_H^{-1/2}$
T_{01}	Local plane wave transmission coefficient from the water column to the layer
T_{10}	Local plane wave transmission coefficient from the layer to the water column
$V_n(p,\omega)$	Plane wave reflection coefficient for the n-th multiple reflection after the ray phase term is removed
$W^{(1),(2)}(x)$	Fock functions defined by $[Ai(-x) + iBi(-x)]$
Z	$= z + z_0$
z, z_0	Receiver and source heights above the bottom, respectively
z_t	Turning depth defined by $Q(z_t) = 0$

Chapter 1: Introduction

It has been observed in the deep ocean that the total acoustic field generated by a harmonic point source placed in the water column near the ocean bottom is characterized by strong interference between the field reflected off the bottom and the direct field through the water column. The amplitude of this total field thus shows a distinct spatial interference pattern with horizontal range(cf. Fig. 1.1).

This thesis involves the analytic computation of the bottom reflected acoustic field using assumed geoacoustic models in order to understand the mechanism of propagating waves in ocean bottom sediments. The analytic results obtained here are based on asymptotic approximations valid in the far field and characterize different types of rays which contribute to the total reflected field. Therefore, they provide physical insight into the understanding of energy partitioning in the sediments.

The methods developed in this thesis will be applied both to the examination of the fields generated by various "canonical" geoacoustic models and to actual experimental pressure field measurements made by Frisk and his co-workers[5]. Extensive tests to determine which major ray paths contribute to the total reflected field will be performed throughout horizontal range as well as an investigation of the effects of geoacoustic parameters on such rays.

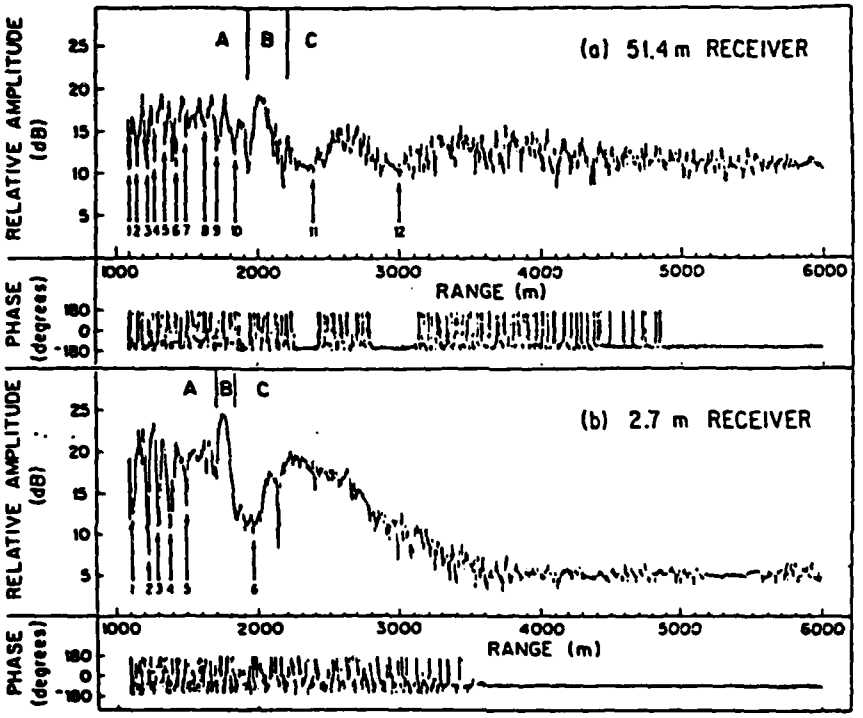

Fig. 1.1 A typical pressure field measurement (Ref. 5).

1.1 Background

1.1.1 Oblique incidence bottom acoustic experiments

A typical experimental configuration by Frisk et. al.[5] is shown in Fig. 1.2. A 220-Hz CW source is suspended on the trawl wire of the ship which slowly drifts away from a receiving system that consists of two receivers moored on the bottom. The source is maintained at about 100-200 m above the bottom as it moves away from the receivers out to a horizontal range of a few kilometers. By sampling the incoming signals at a sufficient rate, Frisk obtains spatially continuous acoustic fields near the bottom due to the time harmonic point source which is also placed near the bottom.

Since the source and receiver are placed relatively close to the bottom in the experiments as shown in Fig. 1.2, except at relatively short ranges, most of the rays interact at small grazing angles with the sediment layer with increasing sound velocity(cf. Fig. 1.3). This is not the case if the source and/or receiver are placed at a high elevation above the bottom, for example if both are at the surface or if the source is at the surface and the receiver at the bottom as done in more conventional deep-sea seismic experiments for ranges up to a few kilometers(cf. Fig. 1.4).

Spudich and Helmberger[11] computed the seismic responses of similar ocean bottom models covered by a 4-km thick water column in a frequency band of 1-30 Hz for both source and receiver located near the ocean surface. Step-function source responses were computed over the range of 2-20 km with the increment of 1 km. In their computation they

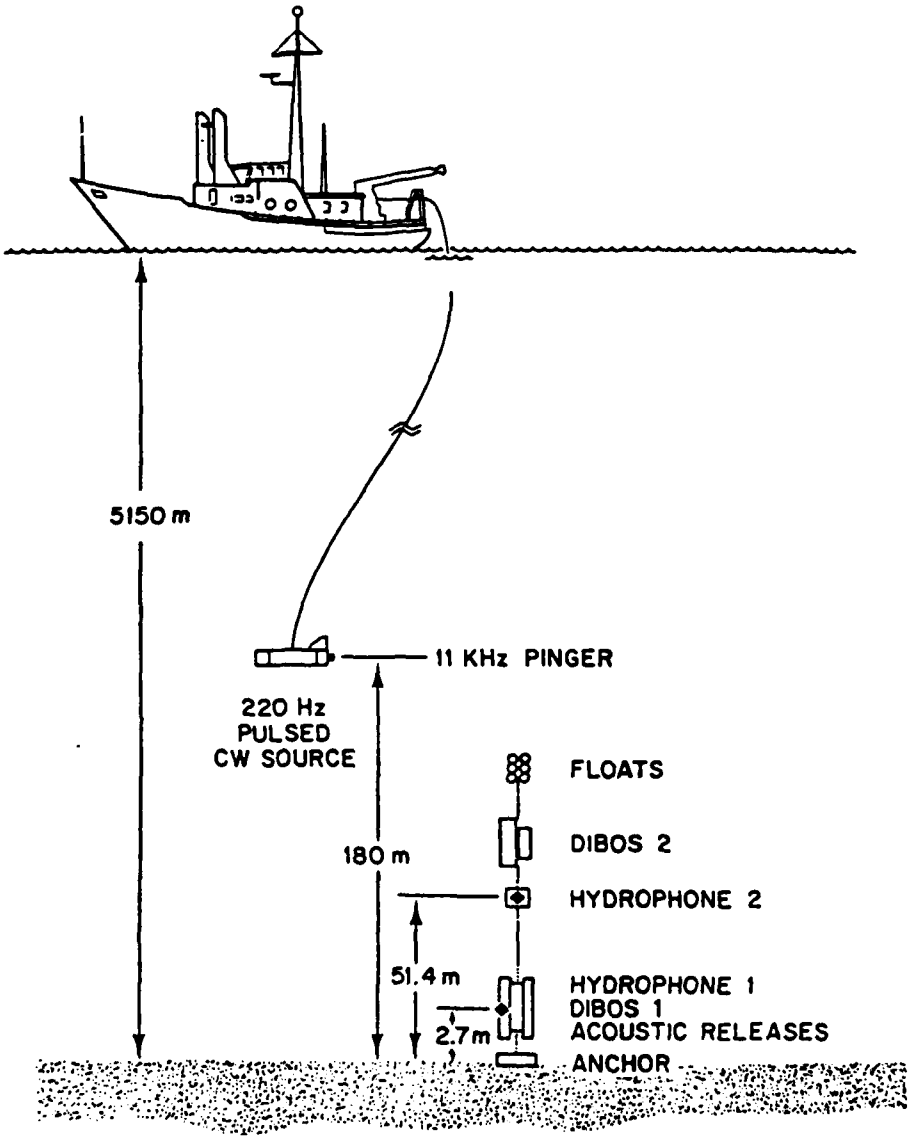

Fig. 1.2 A schematic of the experimental configuration (Ref. 5).

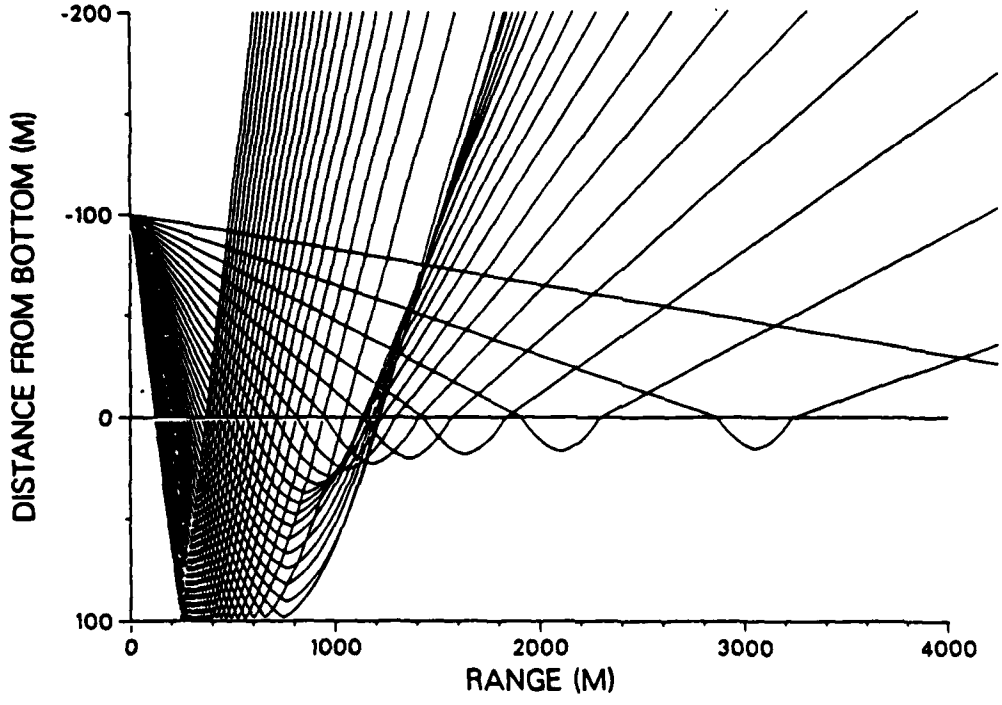

Fig. 1.3 A ray diagram for the case where the source and receiver are placed near the ocean bottom.

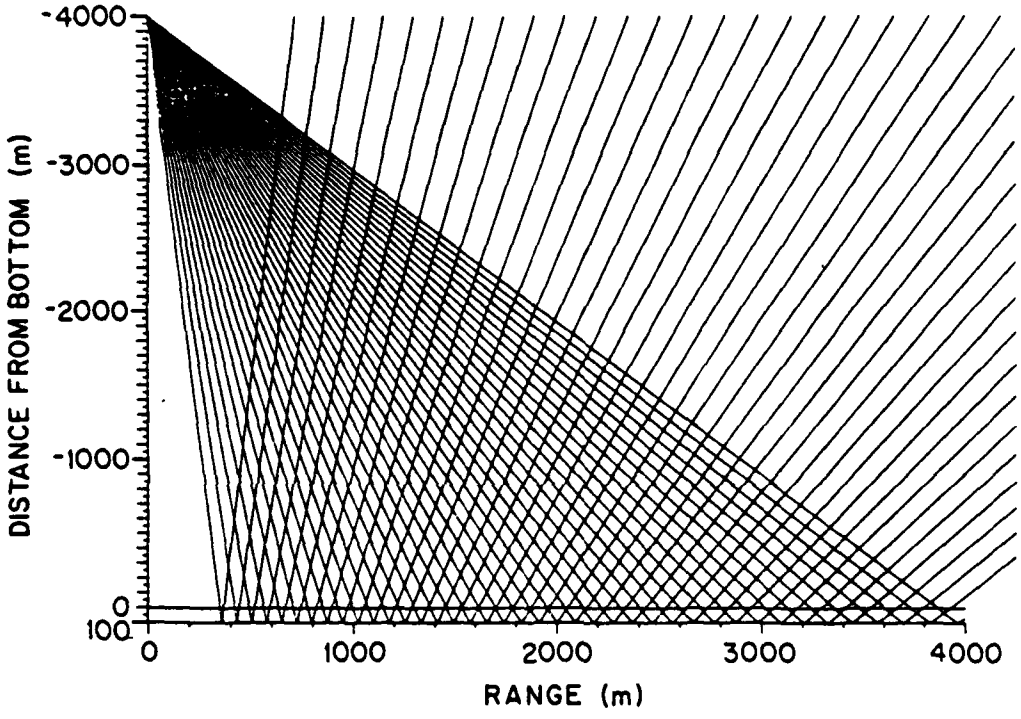

Fig. 1.4 A ray diagram for the case where the source and receiver are placed at the surface of the 4000 m-deep ocean.

applied the generalized ray theory[1] to major ray paths excluding any internal multiple reflections and absorption in the sediment layers, and concluded that the sediment layer gradient and its thickness were insignificant to the seismic responses. A major source of the effects they studied was the basement structure under the sediment layers. In these cases the rays interact with the sediments at steep angles and are therefore relatively insensitive to the details of the sediment velocity profile.

Because of these contrasting bottom acoustic interactions due to the different relative locations of the source and receiver with respect to the bottom as shown in Figs. 1.3 and 1.4, we shall not be concerned with geoacoustic models with multi-layered structures, but instead shall concentrate on the detailed profile shapes of a single layer. Also, for higher frequencies used in Frisk's experiments, the effect of absorption in the sediment layers now become more important, and the number of major ray paths may be greater for the close range fields where, for example, the effects of multiples may not be negligible.

Vidmar[13] and R. Chapman[3] have reported that for typical ocean bottom structures there is a minor energy-loss mechanism due to the presence of shear waves in the bottom for near grazing incidence. Also, in our experience with real data analysis, there has been success with geoacoustic models that exclude shear waves[5], and we shall therefore not include shear in our geoacoustic models.

1.1.1 Sommerfeld Integral and geoacoustic models of the bottom

For harmonic time dependence ($e^{-i\omega t}$), the reflected spatial part of the acoustic pressure field P in a homogeneous medium due to a point source placed in that medium, which lies over a second horizontally stratified medium can be expressed by the Sommerfeld integral[1,2]

$$P = \frac{i\omega}{2} \int_{-\infty}^{\infty} H_0^{(1)}(\omega p r) \frac{p}{\gamma_0} R(p,\omega) \exp[i\omega\gamma_0(z_0 + z)\, dp \qquad (1.1)$$

where p = horizontal slowness (ray parameter)

z_0, z = source and receiver heights above the boundary

r = horizontal range

$R(p,\omega)$ = plane wave reflection coefficient

γ_0 = vertical slowness in the source-receiver medium

$H_0^{(1)}$ = the zero-th order Hankel function of the first kind

ω = angular frequency of the source

Given the small sound velocity gradient in the water column in the deep ocean (typically less than .016 s^{-1}[10]), it is reasonable to assume that the water column is homogeneous, especially for experiments which involve small source and receiver heights. In many abyssal plain regions, one may also assume that the ocean bottom is horizontally stratified. In such cases, Eq. (1.1) is a valid expression for the bottom reflected acoustic fields.

The plane wave reflection coefficient R, which is the weighting factor in the integrand of the Sommerfeld integral, contains all of the

acoustic properties of the bottom as well as satisfying the boundary condition at the ocean bottom interface. The physical and mathematical complexity of R depends on the detailed geoacoustic properties of the bottom structure.

In order to obtain analytic solutions for P in Eq. (1.1), we must consider reasonably simple geoacoustic models. Yet such models must be realistic enough to generate fields which compare favorably to real data. Macpherson and Frisk[5] have obtained analytic expressions for the total field using the method of normal modes, but their geoacoustic model was a slab configuration, a homogeneous layer between two homogeneous halfspaces. Using a modified uniform asymptotic method, Stickler and Ahluwalia[12] obtained analytic solutions based on a more realistic model containing a layer with a $1/c^2$-linear profile between two homogeneous halfspaces. However, the sound velocities were required to be continuous at the layer boundaries, i.e. no discontinuities were allowed. In both cases, the geoacoustic models used as input to them lack some realistic features necessary to discuss real data. A more complete geoacoustic model should contain an inhomogeneous layer with a monotonically increasing sound velocity profile bounded by homogeneous halfspaces with arbitrary boundary conditions as shown in Fig. 1.5.

1.2 Asymptotic approximation of the Sommerfeld integral

Our goal is to evaluate the Sommerfeld integral analytically. This involves two steps. The first step is to obtain the reflection coefficient R based on our geoacoustic models and the second is to evaluate the integral. In order to obtain R, we must evaluate the field inside

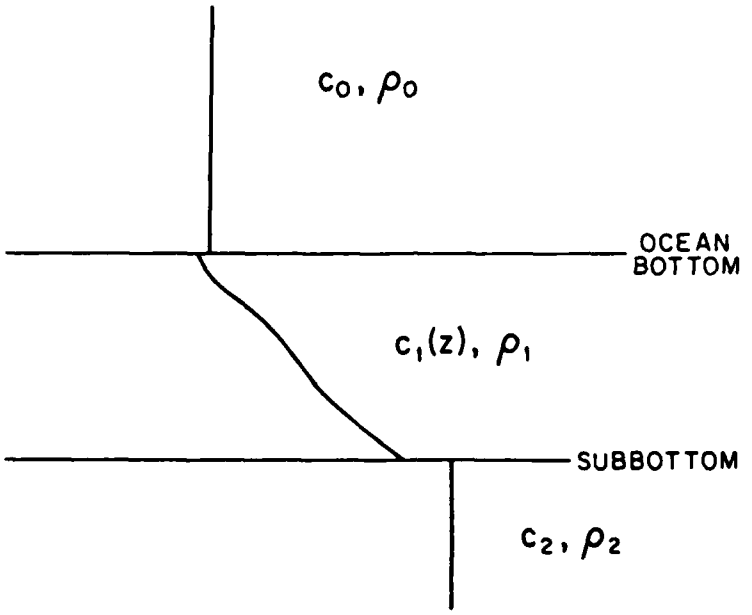

Fig. 1.5 A geoacoustic model considered in this thesis. The sound velocity in the layer monotonically increases with depth.

the layer. Provided that the sound velocity within the layer monotonically increases with depth, we can apply the Langer uniform asymptotic approximation(L.U.A.A.)[7, 8] to compute the field. The method has been applied by Cormier and Richards[4], and Kennett and Illingworth[6] in numerical seismic synthesis. The advantage of the L.U.A.A. is that, unlike the W.K.B.J. method, it is uniformly valid for any horizontal slowness (or equivalently horizontal component of the wave number) in a given medium for any profile shape as long as the sound velocity monotonically increases. Once the field inside the layer is obtained analytically, the analytic expression for the reflection coefficient R can be found easily from the boundary conditions.

It is of interest to understand the energy partitioning of propagating acoustic waves associated with various ray types as a function of horizontal range. In order to do this, we shall expand the total reflection coefficient in a series of partial reflection coefficients which have a straightforward physical ray-phase interpretation. Having done this, we shall evaluate the resulting series of Sommerfeld integrals by the method of steepest descents. The results are more accurate than that of ray theory and provide reflected fields readily associated with different ray types.

1.3 Overview

Chapter 2 focuses on the mathematical details of the analytic evaluation of the field in the layer using the L.U.A.A. Satisfying the boundary conditions, the total plane wave reflection coefficient will be then evaluated. Finally, the Sommerfeld integral will be evaluated us-

ing the method of steepest descents. The accuracy of these methods is also demonstrated by comparison with numerical results. Two types of interface waves, one along the ocean bottom interface and the other along the subbottom interface, are also discussed. An equation for the interface wave along the subbottom for the n-th multiple reflection is derived.

In Chapter 3, using the mathematical tools developed in Chapter 2, we examine a wide range of geoacoustic models by parametrically varying the layer thickness and other geoacoustic parameters, as well as the source-receiver geometry. We shall also discuss a simple but accurate analytic expression for the sound velocity profile, given in the form of c^3-linear in depth, based on measurements in order to make our geoacoustic models more realistic.

Chapter 4 is devoted to the discussion of caustics due to three different canonical profile shapes, the $1/c^2$, c and c^3-linear profiles. Caustic equations are derived for these profile shapes. It is shown that the top portion of the sound velocity profile in the layer is most critical for caustic formation based upon our geoacoustic models. The fields near the caustics are also derived and examined for these profile shapes. It will be shown that the amplitude variation of the fields near the caustic solely depends on the curvature of the caustic.

Finally, in Chapter 5, real data collected from field experiments will be analyzed using the technique developed in Chapter 2 and discussed using the knowledge obtained from the model studies in Chapter 3. It will be demonstrated that the recovery of geoacoustic parameters from measurements has a strong connection to the geometric orientation

of source and receiver.

References:

[1] Aki, K. and Richards, P. G., Quantitative Seismology-Theory and Methods, Vol. 1, Freeman, San Francisco, 1980.

[2] Brekhovskikh, L. M., Waves in Layered Media, 2nd ed., Academic Press, New York, 1980.

[3] Chapman, R. N., "Modeling ocean-bottom reflection loss measurements with the plane-wave reflection coefficient," J. Acoust. Soc. Am. 73, 1601-1607 (1983).

[4] Cormier, V. F. and Richards, P. G., "Full wave theory applied to a discontinuous velocity increases: The inner core boundary," J. Geophys. 43, 3-31 (1977).

[5] Frisk, G. V., Doutt, J. A. and Hays, E. E., "Bottom interaction of low-frequency acoustic signals at small grazing angles in the deep ocean," J. Acoust. Soc. Am. 69, 84-94 (1981).

[6] Kennett, B. L. and Illingworth, M. R., "Seismic waves in a stratified half space III. Piecewise smooth models," Geophys. J. R. astr. Soc. 66, 633-675 (1981).

[7] Langer, R. E., "The asymptotic solutions of ordinary linear differential equations to the second order, with special reference to a turning point," Trans. Am. Math. Soc. 67, 461-490 (1940).

[8] Langer, R. E., "Asymptotic solutions of a differential equation in the theory of microwave propagation," Commun. Pure Appl. Math. 3, 427-438 (1950).

[9] Macpherson, M. K. and Frisk, G. V., "The contribution of normal modes in the bottom to the acoustic field in the ocean," J. Acoust. Soc. Am. 68, 929-940 (1980).

[10] Medwin, H. and Clay, C. S., Acoustical Oceanography: Principles and Applications, John Wiley and Sons, New York, 1977.

[11] Spudich, P. K. P. and Helmberger, D. V., "Synthetic Seismograms From Ocean Bottoms," J. Geophys. Res. 84, 189-204 (1979).

[12] Stickler, D. C. and Ahluwalia, D. S., "Impedance calculations for a refracting layer," J. Acoust. Soc. Am. 66, 514-521 (1979).

[13] Vidmar, P. J., "The effect of sediment rigidity on bottom reflection loss in a typical deep sea sediment," J. Acoust. Soc. Am. 68, 634-638 (1980).

CHAPTER 2: Mathematical Formulation

Analytic solutions to the problem we have described in Chapter 1 will be discussed in great detail in this Chapter. Our mathematical treatment for the evaluation of the Sommerfeld integral given by Eq. (1.1) is based on asymptotic expansion techniques which assume that the receiver is many wavelengths away from the source.

Our asymptotic approximation to the reflected fields is twofold. The first step is to compute the total reflection coefficient, which is the weighting factor inside the Sommerfeld integral, by using Langer uniform asymptotic approximations. The results are accurate and yet the analytic solutions are general enough to treat various typical geoacoustic models. The second-step asymptotic approximation is to evaluate the Sommerfeld integral by the method of steepest descents with the reflection coefficients already evaluated. The final solutions for the reflected fields are completely analytic and are functions of the geoacoustic parameters and source-receiver geometries.

2.1 Computation of the Total Reflection Coefficient Using the Langer Uniform Asymptotic Approximation

The total reflection coefficient for the proposed geoacoustic model shown in Fig. 1.5 will be given after general solutions to the acoustic velocity potential in the sediment layer are evaluated using the Langer uniform asymptotic approximation (L.U.A.A.)[10]. Then it will be shown that the resulting closed form of the total reflection

coefficient may be reduced to ray theory results for certain regions of incident angles where ray theory is valid. This total reflection coefficient based on the L.U.A.A. will be compared to a numerical result generated by the Thomson-Haskell propagator-matrix method[1].

2.1.1 General Solutions

We will refer to the water column, the layer and the basement as medium 0, 1 and 2 respectively. First we consider the general solutions in medium 1. The acoustic time dependent velocity potential $W(x,y,z,t)$ satisfies the the following inhomogeneous wave equation

$$\left(\nabla^2 - \frac{1}{c_1^2(z)} \frac{\partial^2}{\partial t^2} \right) W(r,z,t) = 0$$

After the harmonic time dependence $e^{-i\omega t}$ is assumed, $W(r,z,t)$ can be written as

$$W(r,z,t) = \Phi(r,z)\, e^{-i\omega t}$$

After the horizontal terms are separated from $\Phi(r,z)$, we are left with the z-dependent potential $F_1(z)$ which satisfies the onedimensional Helmholtz equation,

$$\frac{d^2F_1(z)}{dz^2} + \omega^2 Q^2(z)\, F_1(z) = 0 \qquad (2.1)$$

where ω = angular frequency (rad/s)

and $$Q^2(z) = \frac{1}{c_1^2(z)} - p^2. \qquad (2.2)$$

Here $c_1(z)$ is the sound velocity profile in the medium 1 as a function of depth and p is the horizontal slowness or ray parameter. The horizontal wave number k_r can be given in terms of p as $k_r = \omega p$ and the vertical wave number k_z as $k_z = \omega Q$.

Solving for F(z) analytically for a given $c_1(z)$ is in general very difficult except for a few examples[5]. A more desirable solution, which does not have to be exact, but rather flexible in dealing with various acoustic properties in ocean bottom, may be found in a form of asymptotic approximation. We will now consider the following differential equation:

$$\frac{d^2G(z)}{dz^2} + \omega^2[Q^2(z) - E(z)]\, G(z) = 0 \qquad (2.3)$$

where E(z) is given by

$$E(z) = \frac{\Psi''}{\Psi}\ ; \qquad \psi = \eta^{1/6}\, Q^{-1/2} \qquad (2.4)$$

Here η is known as the phase integral and is given by

$$\eta(z) = \int_{z_t}^{z} Q(z')\, dz' \qquad (2.5)$$

where z_t is the turning depth defined by the condition,

$$Q(z_t) = \left[\frac{1}{c_1^2(z_t)} - p^2\right]^{1/2} = 0 \qquad (2.6)$$

In general, when absorption is included in the sound velocity profile, $c_1(z)$ is a complex function. Thus, z_t may be a complex number[6]. The phase integral in the complex z-plane can be evaluated along a contour such as one shown in Fig. 2.1. The branch cut due to the radical Q is present where the imaginary part of Q is zero. Since the contour always originates at the branch point z_t, there is no branch cut contribution involved and the integration is quite straightforward.

The basic argument of the L.U.A.A. is that if E(z) approaches zero as $\omega/[dc(z)/dz]$ becomes very large for any given p, then G(z) asymptotically approaches the desired solution F(z). Indeed it is possible to obtain such an E(z) as long as the following conditions are satisfied:

1. There is only one first-order turning point for a given p in the profile. A first-order turning point is defined as one for which $Q(z_t) = 0$, but $Q'(z_t) \neq 0$. Here the prime denotes the derivative with respect to z.
2. The profile $c_1(z)$ must be smooth [i.e. the condition given by Eq. (A.7)] near the turning point. Since this condition must be met for any p and associated z_t, $c_1(z)$ must be smooth everywhere.

In brief, $c_1(z)$ must be a smooth, monotonically increasing function. The acoustic properties within a layered structure of the ocean

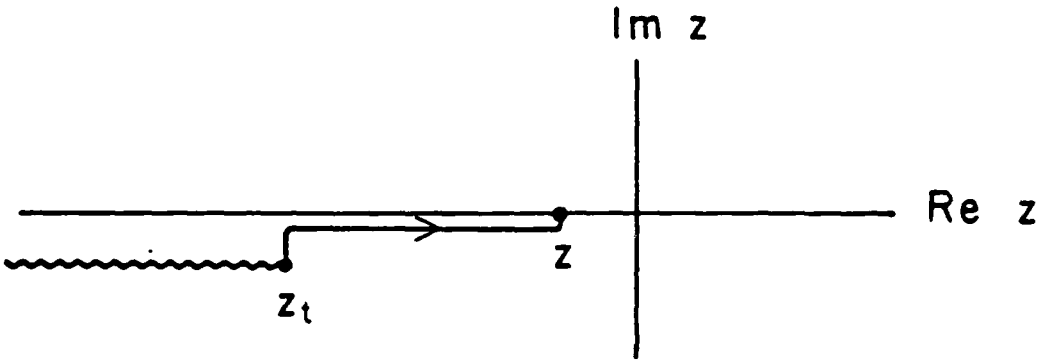

Fig. 2.1 The complex z-plane with a integration contour to evaluate the phase integral η. The branch point is located at $z = z_t$.

bottom typically satisfy these conditions.

The exact solutions of Eq. (2.3)[9] are given by

$$G_1(z) = Q^{-1/2}\nu^{1/4}\,\mathrm{Ai}(-\nu) \tag{2.7a}$$

$$G_2(z) = Q^{-1/2}\nu^{1/4}\,\mathrm{Bi}(-\nu) \tag{2.7b}$$

where $$\nu \equiv [\tfrac{3}{2}\,\omega\eta(z)]^{2/3} \tag{2.8}$$

Therefore, the z-component of the field in the layer for the given p becomes asymptotically

$$F_1(z) \sim Q^{-1/2}\nu^{1/4}[B_1\mathrm{Ai}(-\nu) + B_2\,\mathrm{Bi}(-\nu)] \quad \text{as } \omega \to \infty \tag{2.9}$$

The error analysis of the L.U.A.A. is discussed in Appendix A.

Since medium 0 is assumed to be homogeneous, the z-component of the general solutions for the velocity potential can be easily obtained and is given by

$$F_0(z) = A_1\, e^{i\omega\gamma_0 z} + A_2\, e^{-i\omega\gamma_0 z} \tag{2.10}$$

where $$\gamma_0 = (\frac{1}{c_0^2} - p^2)^{1/2} \tag{2.11}$$

Similarly, in medium 2

$$F_2(z) = C_1\, e^{-i\omega\gamma_2 z} \tag{2.12}$$

where $$\gamma_2 = (\frac{1}{c_2^2} - p^2)^{1/2} \tag{2.13}$$

Note that there is only one term in Eq. (2.12) in order to satisfy the radiation condition. A_1, A_2, B_1, B_2 and C_1 are arbitrary constant coefficients for a given p and remain to be found from appropriate boundary conditions, which will be discussed shortly. After multiplication by the horizontal component, the potential is given by

$$\Phi_i(r, z) = F_i(z)\, e^{i\omega pr};\ i = 0, 1, 2 \tag{2.14}$$

in the i-th medium for a given p.

2.1.2 Boundary Conditions

Since the pressure and vertical component of the motion of the particles must be continuous across the boundaries, $\rho_i\Phi_i$ and $d\Phi_i/dz$ must be equal at the interfaces in order to satisfy these conditions respectively. Thus we can obtain the following equations:

At z = 0 (the ocean bottom)

$$\rho_0(A_1 + A_2) = \rho_1[B_1G_1(0) + B_2G_2(0)] \tag{2.15}$$

$$i\omega\gamma_0(A_1 - A_2) = B_1G_1'(0) + B_2G_2'(0) \tag{2.16}$$

At z = H (the subbottom)

$$\rho_1[B_1G_1(H) + B_2G_2(H)] = \rho_2C_1e^{-i\omega\gamma_2H} \tag{2.17}$$

$$B_1 G_1'(H) + B_2 G_1'(H) = - iC_1 \omega \gamma_2 \, e^{-i\omega\gamma_2 H} \tag{2.18}$$

where $$G_1(z) = Q^{-1/2} \nu^{1/4} Ai(-\nu) \tag{2.19a}$$

$$G_2(z) = Q^{-1/2} \nu^{1/4} Bi(-\nu) \tag{2.19b}$$

Solving for A_1 assuming a unit amplitude in the incident wave ($A_2 = 1$), we finally obtain the total reflection coefficient for this geoacoustic ocean bottom model,

$$R(p) = \frac{(A_0^{(2)} - B_0^{(2)})(A_H^{(1)} - B_H^{(1)}) - (A_0^{(1)} - B_0^{(1)})(A_H^{(2)} - B_H^{(2)})}{(A_0^{(2)} + B_0^{(2)})(A_H^{(1)} - B_H^{(1)}) - (A_0^{(1)} + B_0^{(1)})(A_H^{(2)} - B_H^{(2)})} \tag{2.20}$$

where $$A_0^{(1),(2)} = i\rho_1 \gamma_0 W^{(1),(2)} \quad (z = 0) \tag{2.21a,b}$$

$$B_0^{(1),(2)} = -\rho_0 Q_0 \nu_0^{-1/2} W'^{(1),(2)} \quad (z = 0) \tag{2.22a,b}$$

$$A_H^{(1),(2)} = i\rho_1 \gamma_2 W^{(1),(2)} \quad (z = H) \tag{2.23a,b}$$

$$B_H^{(1),(2)} = -\rho_2 Q_H \nu_H^{-1/2} W'^{(1),(2)} \quad (z = H) \tag{2.24a,b}$$

with $Q_0 = Q(z=0)$, $Q_H = Q(z=H)$

$\nu_0 = \nu(z=0)$, $\nu_H = \nu(z=H)$

$$W^{(1),(2)}(\nu(z)) = Ai(-\nu) \mp iBi(-\nu) \tag{2.25a,b}$$

$$W'^{(1),(2)}(\nu(z)) = -\left(\frac{dAi(-\nu)}{d\nu} \mp \frac{dBi(-\nu)}{d\nu}\right) \tag{2.26a,b}$$

Here $W^{(1),(2)}$ are known as Fock functions[9]. The solutions may be given in terms of Hankel functions of the 1/3rd order. However, the advantage of using Fock functions is that because they are linear combinations of Airy functions, it is easier to evaluate them numerically than Hankel functions. In addition, similar to Hankel functions, their asymptotic expansions (see Appendix C) behave like propagating plane waves. In general, $W^{(1)}$ and $W^{(2)}$ are not complex conjugates of one another since ν as well as Ai and Bi may be complex numbers.

This asymptotic approximation of the total plane wave reflection coefficient given by Eq. (2.20) is valid for any shape of the sound velocity profile in the sediment layer as long as it is a slowly and monotonically increasing profile. Not only these conditions are met in geoacoustic modeling of a typical ocean bottom, but also this new plane wave reflection coefficient allows us to do more detailed geoacoustic modeling by providing some freedom in the choice of profile shapes. The total plane wave reflection coefficient based on this formulation is compared to the numerical result[13] generated by the Thomson-Haskell Propagator-Matrix method[1] for a typical case of interest (cf. Fig. 2.2) for a frequency of 220 Hz. As shown in Fig. 2.3, their agreement is so good that one may not distinguish one from the other.

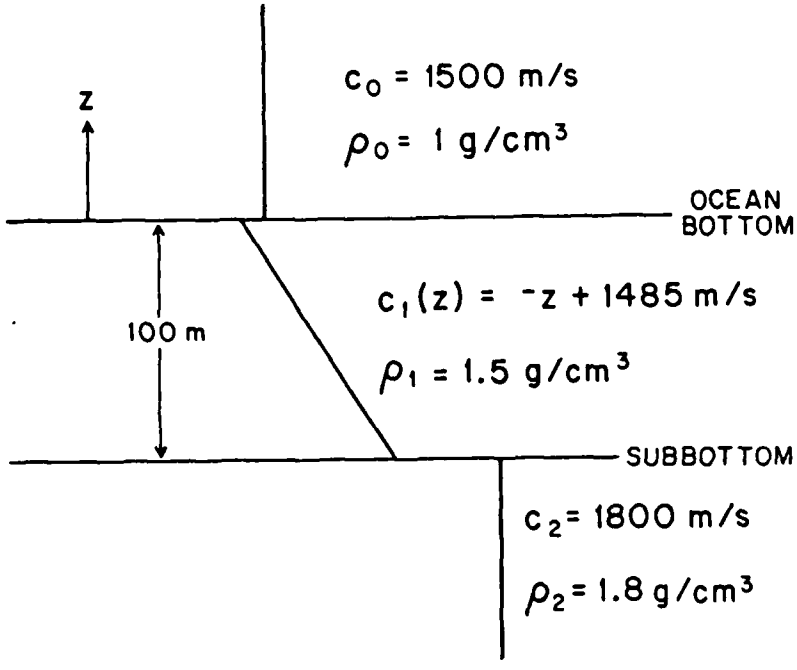

Fig. 2.2 A typical geoacoustic model. A frequency of 220 Hz is used.

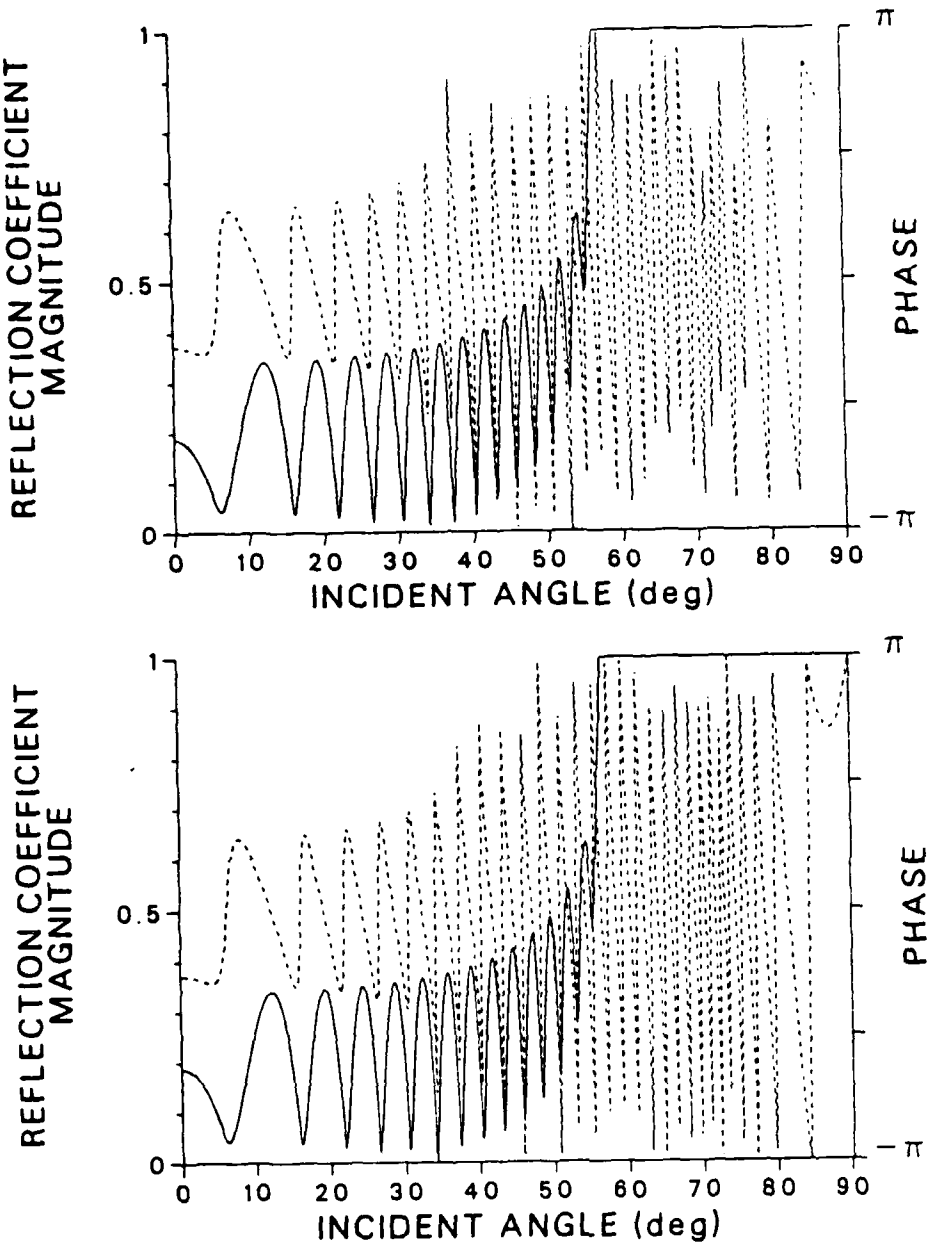

Fig. 2.3 The total reflected coefficients for the model shown in Fig. 2.2. (a) The Thomson-Haskel propagator-matrix method with a step size of 2-m in the layer. (b) The Langer uniform asymptotic approximation.

2.2 Physical Properties of Reflection Coefficients

2.2.1 Expansion of the Total Reflection Coefficient

In this section, the total reflection coefficient obtained using the L.U.A.A. will be decomposed into an infinite sum of partial reflection coefficients. It will be shown that each term represents its own unique physical property analogous to ray theory for special cases where the turning depths are away from both of the interfaces.

The procedure of the expansion is analogous to a ray expansion[11] which decomposes the total reflection coefficient into an infinite sum of reflection coefficients: First, we divide the numerator and denominator of Eq. (2.20) by

$$(A_0^{(2)} + B_0^{(2)})(A_H^{(1)} - B_H^{(1)})$$

to obtain

$$R(p) = \left[\frac{A_0^{(2)} - B_0^{(2)}}{A_0^{(2)} + B_0^{(2)}} - \frac{(A_0^{(1)} - B_0^{(1)})(A_H^{(2)} - B_H^{(2)})}{(A_0^{(2)} + B_0^{(2)})(A_H^{(1)} - B_H^{(1)})} \right] \times \left[1 - \frac{(A_0^{(1)} + B_0^{(1)})(A_H^{(2)} - B_H^{(2)})}{(A_0^{(2)} + B_0^{(2)})(A_H^{(1)} - B_H^{(1)})} \right]^{-1} \qquad (2.27)$$

Second, we perform a binomial expansion of the second bracket. This process may be justified by introducing a small positive imaginary part in $c_1(z)$ which makes the absolute value of the second term always

smaller than unity, and letting the imaginary part go to zero after the expan- sion. After a few more steps, R(p) becomes

$$R(p) = R_0 + \sum_{n=1}^{\infty} R_n \tag{2.28}$$

where

$$R_0 = \frac{A_0^{(2)} - B_0^{(2)}}{A_0^{(2)} + B_0^{(2)}} \tag{2.29}$$

$$R_n = \frac{4\rho_0\rho_1\gamma_0 Q_0 \nu_0^{-1/2}}{\pi (A_0^{(2)} + B_0^{(2)})^2} \quad \frac{A_H^{(2)} - B_H^{(2)}}{A_H^{(1)} - B_H^{(1)}}$$

$$X\left[\frac{(A_0^{(1)} + B_0^{(1)})(A_H^{(2)} - B_H^{(2)})}{(A_0^{(2)} + B_0^{(2)})(A_H^{(1)} - B_H^{(1)})}\right]^{n-1} \tag{2.30}$$

In order to obtain a physical interpretation of each term, we substitute the asymptotic forms of the Airy functions. The conditions for which the Airy functions may be expanded are equivalent to the condition that the turning depth for a given horizontal slowness p is many wavelengths away from either boundary. The first term, R_0 can then be reduced to

$$R_0 \sim \frac{\rho_1\gamma_0 - \rho_0 Q_0}{\rho_1\gamma_0 + \rho_0 Q_0} \tag{2.31}$$

This is simply the Rayleigh plane wave reflection coefficient in medium 0

over the homogeneous half space which is characterized by $c_1(z=0)$ and ρ_1. This is the plane wave reflection coefficient one would expect to obtain for the specularly reflected ray using ray theory. Similarly, for large ν, R_1 can be reduced to

$$R_1 \sim \begin{cases} T_{01}T_{10}R_{12}e^{2i\omega(\eta_0-\eta_H)} & z_t < H \\ T_{01}T_{10}e^{2i\omega\eta_0 - i\pi/2} & 0 > z_t > H \end{cases} \tag{2.32}$$

where T_{01}, T_{10} and R_{12} are local plane wave transmission coefficients and reflection coefficient across the medium 0 to 1, 1 to 0 and 1 to 2, respectively. This is the result one would obtain from ray theory for a ray which reflects off the subbottom or turns within the layer once, depending on the location of the turning depth. Notice the $-\pi/2$-phase shift associated with the refracted ray, a term which is often introduced as a correction in pure ray theory. In exactly the same manner R_n can be reduced to the following asymptotic form for $n > 1$.

$$R_n \sim \begin{cases} R_1[R_{10}R_{12}\, e^{2i\omega(\eta_0 - \eta_H)}]^{n-1} & z_t < H \\ R_1[R_{10}\, e^{2i\omega\eta_0 - i\pi/2}]^{n-1} & 0 > z_t > H \end{cases} \tag{2.33}$$

where R's and T's with two integer subscripts are local plane wave reflection and transmission coefficients at the interface indicated by their subscripts. From the phase in Eq. (2.33), it suggests that R_n behaves asymptotically in n like the n-th multiple which reflects or refracts n times in the layer. R_1 is a special case of R_n with $n = 1$.

Because of the physical interpretation obtained by using the asymptotic approximation, we may call R_0, R_1 and R_n the specular, the primary and the n-th multiple, respectively. The schematics of their physical properties are shown in Fig. 2.4.

We note that while reflection coefficients based on ray theory fail when the turning depth is very close to either interface, these new reflection coefficients based on the L.U.A.A. are uniformly valid for all values of p regardless of the locations of the corresponding turning depths. This is one of the most powerful features of the Langer reflection coefficients.

2.2.2 Comparison with Ray Theory Results

Interesting features of the Langer reflection coefficients as compared to reflection coefficients based on ray theory will be discussed next. In Figs. 2.5-2.7, the specular, primary and second multiple Langer reflection coefficients are compared to the ray theory results for a geoacoustic model shown in Fig. 2.2 at a frequency of 220 Hz.

Because of the small sound velocity drop at the ocean bottom, we observe a minimum amplitude in the specular reflection(cf. Fig. 2.5a) at a particular incident angle. According to ray theory we would expect the specular reflection coefficient to be zero at this angle(cf. Fig. 2.5b), which is the Brewster angle (angle of intromission) associated with two homogeneous media where the upper half-space has the properties ρ_0 and c_0, and the lower half-space has the properties $\rho_1 > \rho_0$ and $c_1(z = 0) < c_0$ [4]. However, the specular reflection coefficient does not become identically zero according to the L.U.A.A., but only becomes a

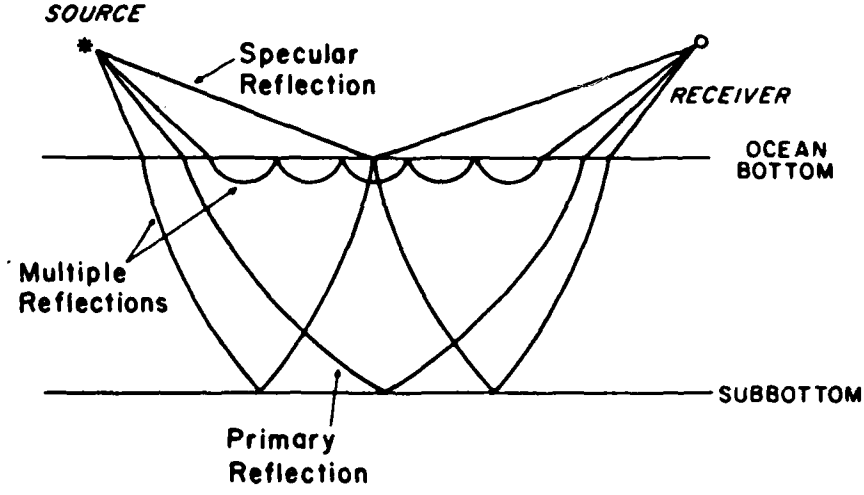

Fig. 2.4 Typical reflecting rays in the bottom.

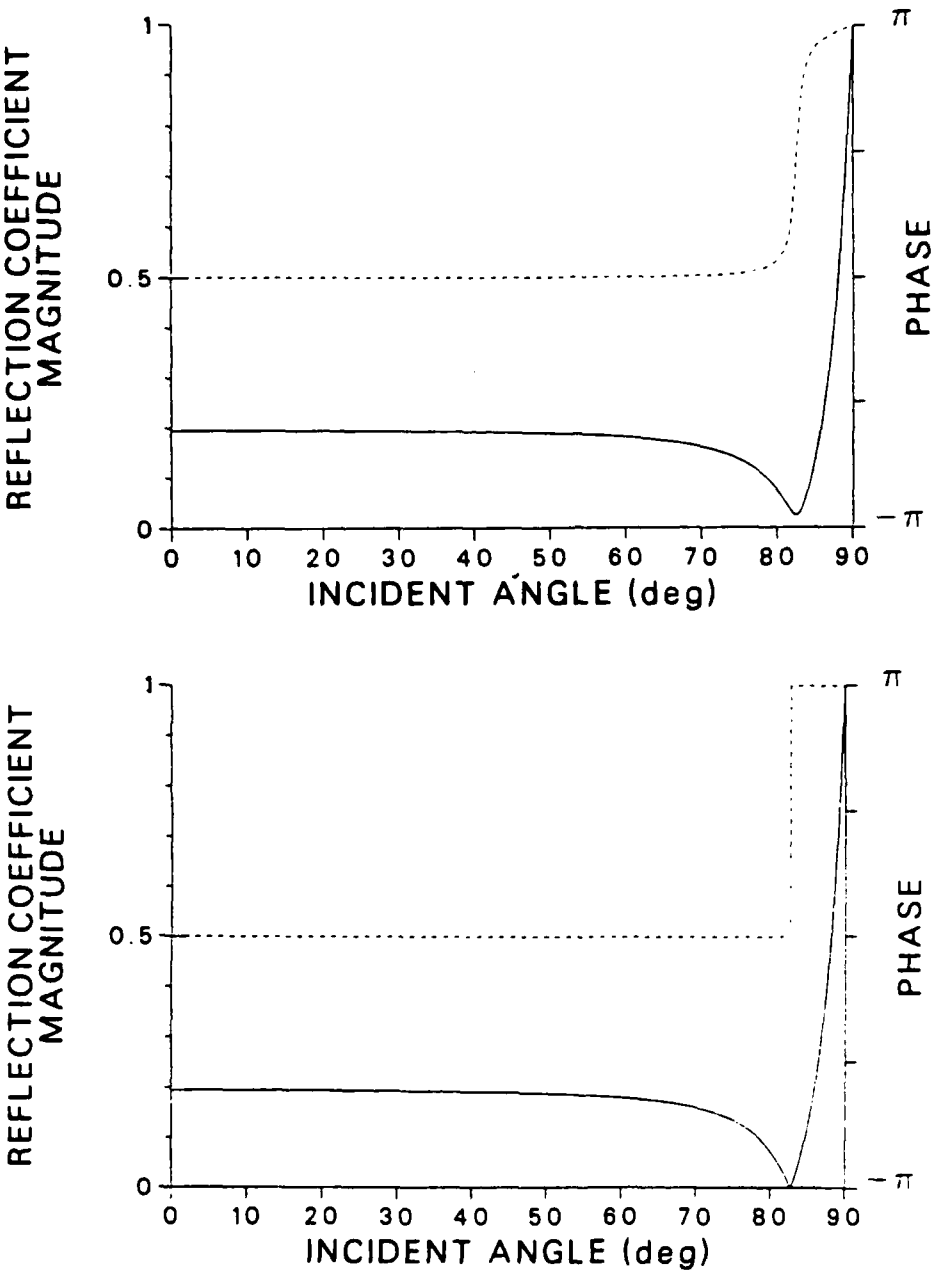

Fig. 2.5 The specular reflection coefficient. A comparison between (a)the L. U. A. A. and (b)ray theory for the model shown in Fig. 2.2. The frequency is 220 Hz.

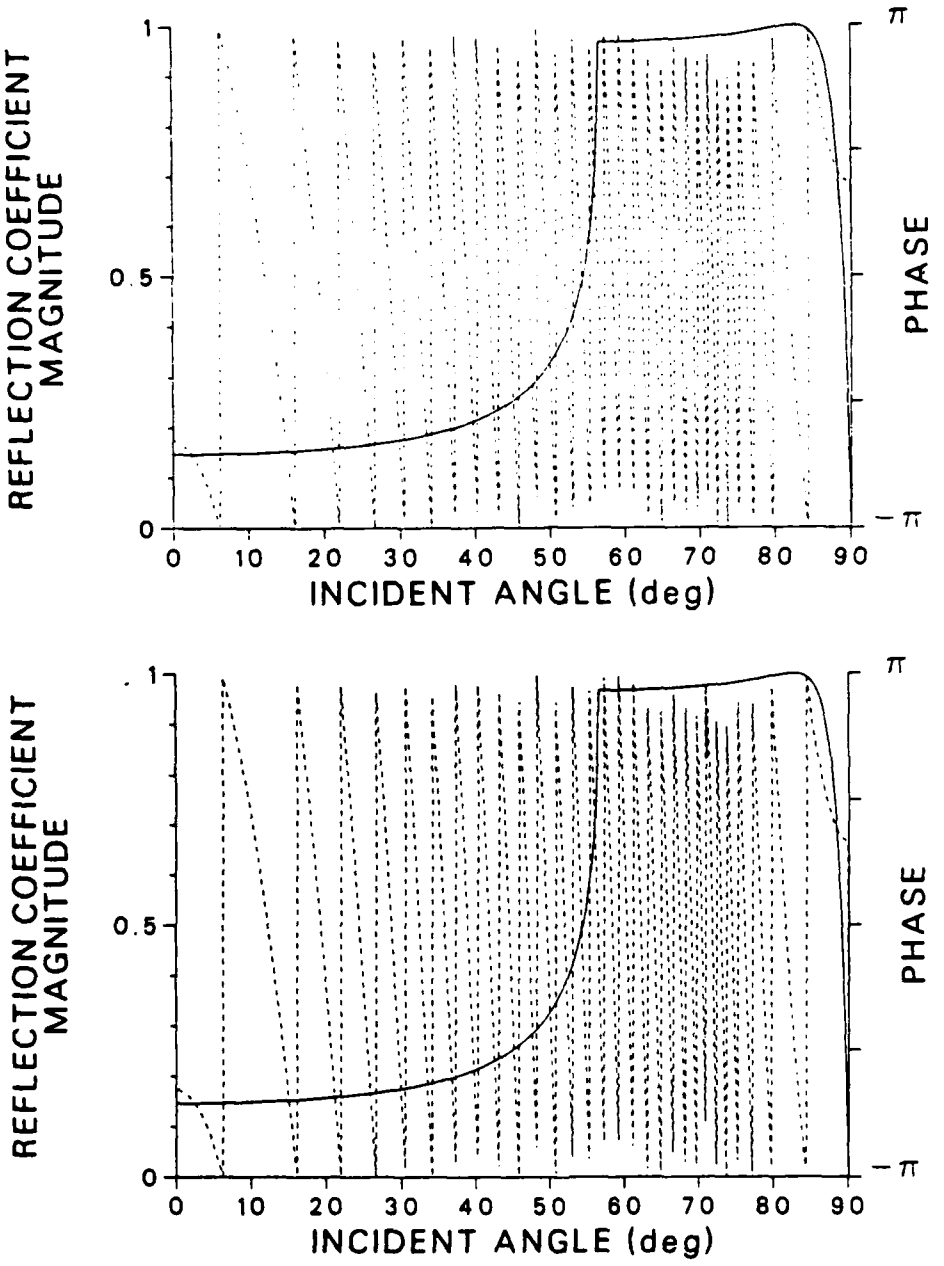

Fig. 2.6 The primary reflection coefficient. A comparison between (a)the L. U. A. A. and (b)ray theory for the model shown in Fig. 2.2. The frequency is 220 Hz.

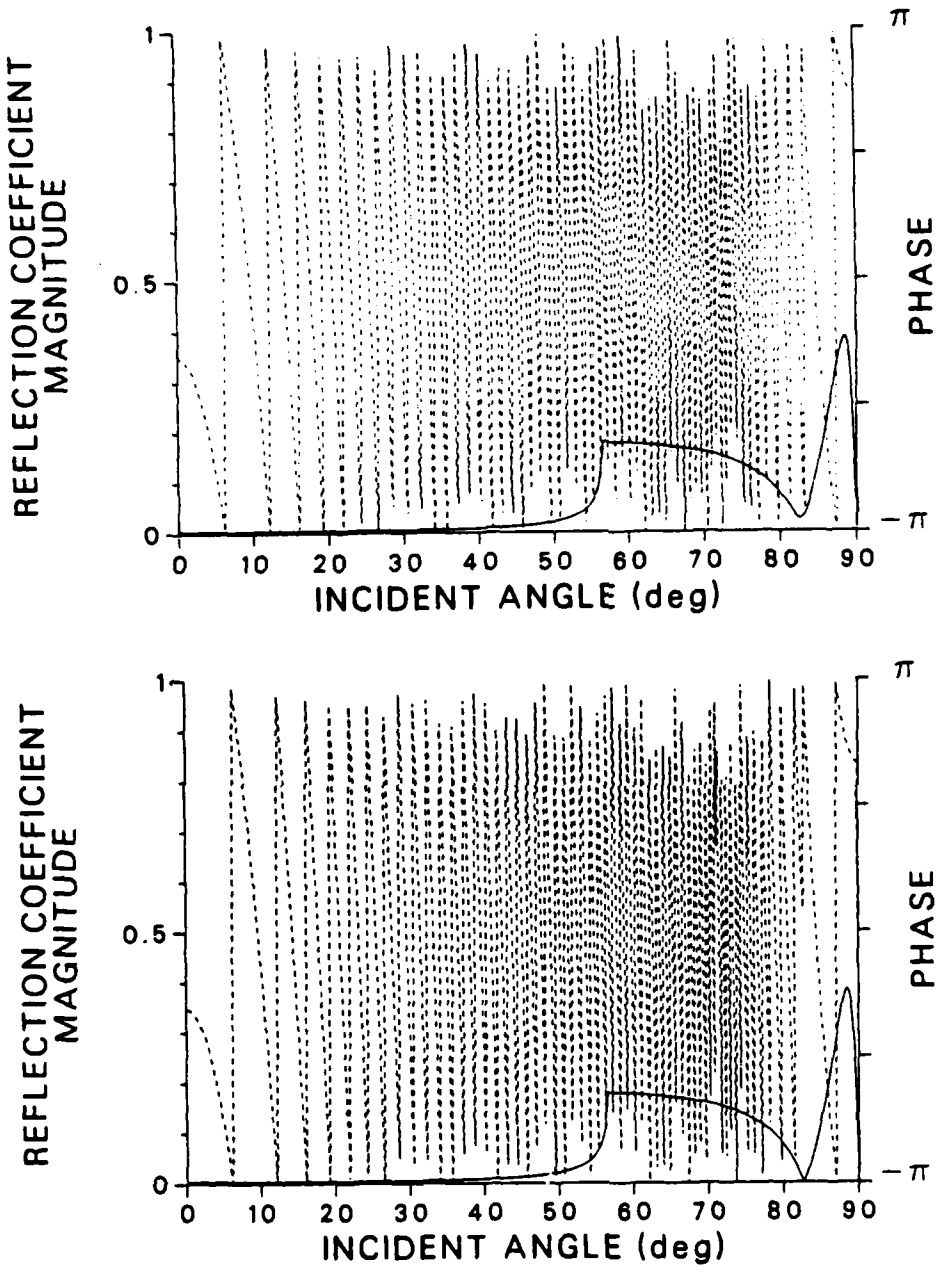

Fig. 2.7 The second multiple reflection coefficient. A comparison between (a)the L. U. A. A. and (b)ray theory for the model shown in Fig. 2.2. The frequency is 220 Hz.

minimum. This is due to the fact that the positive sound velocity gradient in the sediment layer prohibits total wave energy transmission even at the Brewster angle. This discrepancy is also observed in the plane wave reflection coefficients for the multiples(cf. Fig. 2.7).

Another interesting feature of the Langer reflection coefficients can be seen for the geoacoustic model shown in Fig. 2.8. Here the sound velocity is continuous at the water-bottom interface, but there is still a velocity gradient in the bottom and the densities in both media are the same. Ray theory predicts no specular reflection or multiple reflections associated with the water-bottom interface because there is no acoustic impedance discontinuity exists across that interface.

However, according to the Langer reflection coefficients, as shown in Fig. 2.9, one may still obtain non-zero reflection coefficients near grazing incidence. These unexpected results may be explained by the fact that the Langer reflection coefficients take into account not only the discontinuity in the acoustic impedance but also the discontinuity in the derivative of the acoustic impedance with respect to z. This is another example where the Langer reflection coefficients demonstrate their improved accuracy over ray theory based reflection coefficients for a stratified slowly varying medium.

2.3 Asymptotic Expansion of the Sommerfeld Integral by the Method of Steepest Descents

Our goal is to compute the reflected fields due to a harmonic point source, namely to obtain the leading order asymptotic behavior of the Sommerfeld integral, Eq. (1.1), by means of asymptotic approximation. So far we have found the closed form of R(p) in Eq. (1.1) for our

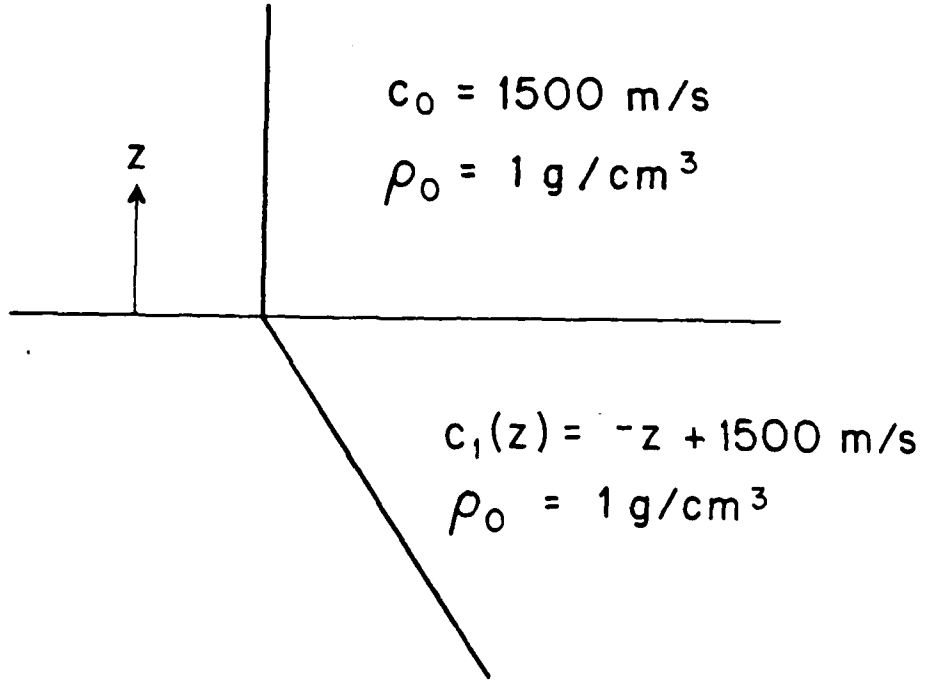

Fig. 2.8 Geoacoustic model with a interface where there are no discontinuities in sound velocity and density.

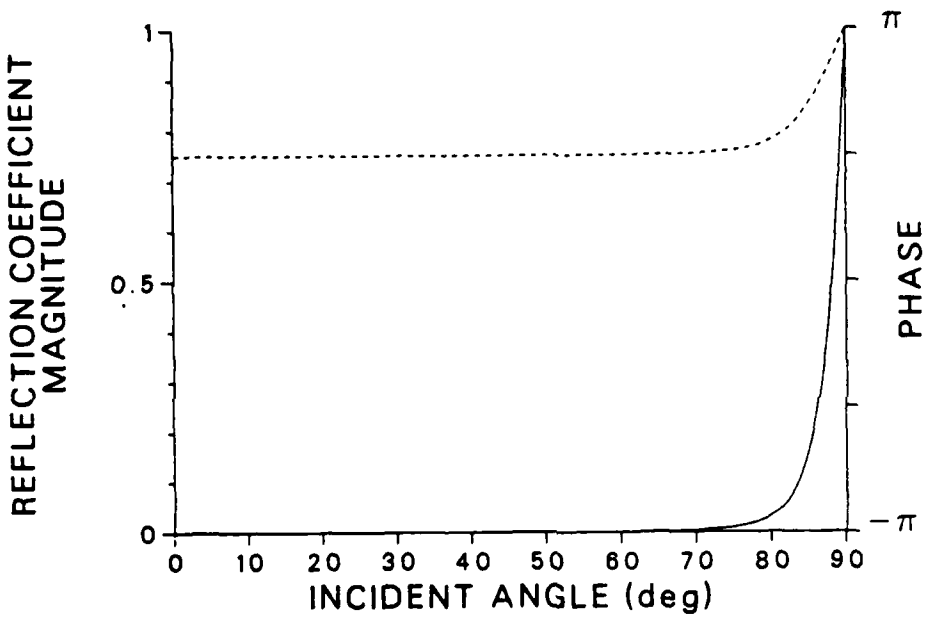

Fig. 2.9 The specular reflection coefficient for the geoacoustic model shown in Fig. 2.8. for the frequency of 220 Hz.

geoacoustic models, and further how to break up R(p) into an infinite number of terms each of which has a physical interpretation in terms of ray theory.

After substituting Eq. (2.28) in Eq. (1.1), we obtain a series of Sommerfeld integrals each of which contains R_n. An asymptotic form of each Sommerfeld integral can provide us an analytic expression for the reflected field as a function of horizontal range coupled with the physical properties of R_n associated with the integrand. While the coherent sum of these asymptotic forms of the integrals provides the total reflected field, we can also evaluate how the individual reflected fields contribute to the total reflected field along horizontal range for various sets of geoacoustic parameters and source-receiver geometries.

Thus, after the Hankel function is replaced with its asymptotic form,

$$H_0^{(1)}(\omega pr) \sim \left(\frac{2}{\pi\omega pr}\right)^{1/2} e^{i\omega pr - i\pi/4}; \qquad \omega pr >> 1,$$

our problem is to evaluate

$$P = \sum_{n=0}^{\infty} P_n$$

where
$$P_n = \sqrt{\frac{\omega}{2\pi r}}\, e^{i\pi/4} \int_{-\infty}^{\infty} R_n \frac{p^{1/2}}{\gamma_0} e^{i\omega[\gamma_0(z+z_0) + pr]}\, dp \qquad (2.34)$$

from which we obtain the reflected field representing the physical prop-

erty that R_n carries.

2.3.1 Mathematical Treatment before the Method of Steepest Descents is Applied

Fig. (2.10) shows the complex p-plane with branch points at $p = 1/c_0$ and $1/c_2$. (Only the $1/c_0$-branch point is present for P_0 containing R_0.) The branch cuts, known as the E.J.P. cuts[8], satisfy the condition that the imaginary parts of the radicals, p, γ_0 and γ_2 are zero. Notice that they are the only radicals that we must be concerned with in the process of deforming the integration contour to evaluate Eq. (2.34) even after the expansion of the total reflection coefficient. Unlike a slab configuration of homogeneous media[10], i.e. a homogeneous layer between two different homogeneous half spaces, we do not create additional branch points as a result of the ray expansion of the total reflection coefficient. Q_0 and Q_H may appear as radicals in R_n at first glance but with $\nu^{-1/2}$ there is no ambiguity in sign.

We shall apply the method of the steepest descents[2] to evaluate P_n. In order to do so we must rewrite P_n in the form of

$$I_n = \int_{-\infty}^{\infty} F_n(p)\, e^{i\omega\phi_n(p)}\, dp \; ; \quad \omega \to \infty \tag{2.35}$$

where F(p) must be a slowly varying function of p, compared to the complex exponential term in order for the method to be valid. When $n \neq 0$, this would not be the case if we made the direct substitutions

$$F_n(p) = R_n \frac{p^{1/2}}{\gamma_0}$$

$$\phi_n(p) = \gamma_0(z+z_0) + pr$$

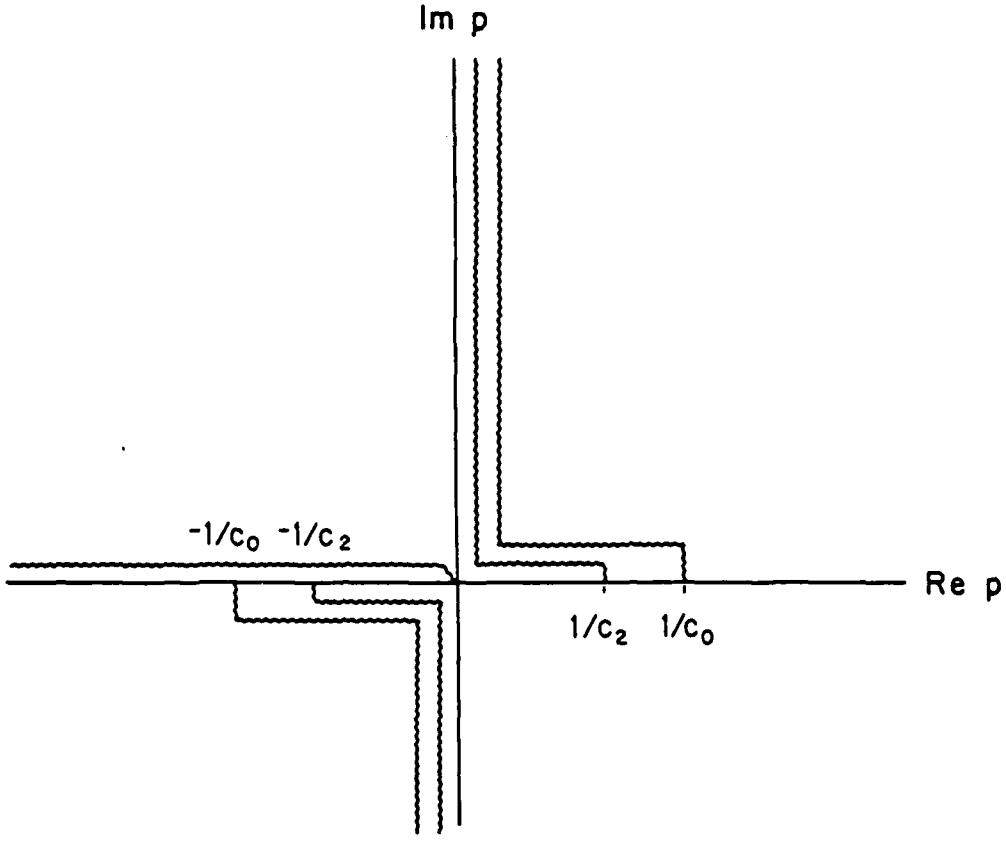

Fig. 2.10 The complex p-plane with the branch cuts.

because R_n is in general a very fast oscillatory function (See Fig. 2.6 or Fig. 2.7 for example). In order to convert Eq. (2.34) into the form of Eq. (2.35) satisfying the above requirement, the following substitutions are suggested:

$$F_n(p) = \frac{V_n\, p^{1/2}}{\gamma_0} \tag{2.36}$$

$$\phi_n(p) = \gamma_0(z + z_0) + pr + 2n\mu \tag{2.37}$$

where

$$V_n = R_n\, e^{-2i\omega n\mu} \tag{2.38}$$

with

$$\mu = \begin{cases} \displaystyle\int_{z_t}^{0} Q(z')\, dz' & 0 > z_t > H \qquad (2.39a) \\ \displaystyle\int_{H}^{0} Q(z')\, dz' & z_t < H \qquad (2.39b) \end{cases}$$

in which the phase term of R_n is estimated from the asymptotic behavior of R_n, which is identical to the ray phase, then separated from R_n and added to the complex exponential term in the integrand. Fig. 2.11 shows V_n vs. incident angle for the primary reflection coefficient of the geoacoustic model shown in Fig. 2.2. Compared to Fig. 2.6, the phase curve has been significantly stabilized. The only appreciable phase variation occurs between critical incidence and the angle at which the ray completely turns in the layer. Since V_n approaches R_n as μ

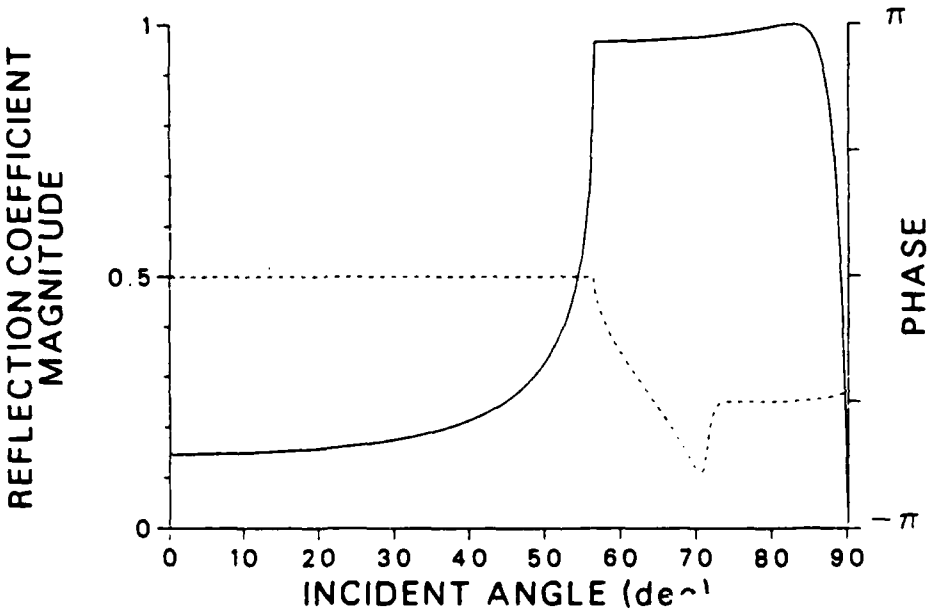

Fig. 2.11 The primary reflection coefficient for the model shown in Fig. 2.2 after the phase term $2n\mu$ is removed.

becomes very small[cf. Eq. (2.38)], the substitutions given by Eq. (2.36) through Eq. (2.38) are valid even when $n\omega\mu$ is not large.

2.3.2 Evaluation of P_n by the Modified Method of Steepest Descents - Saddle Point Contribution

Strictly speaking, a direct application of the method of steepest descents to the Sommerfeld integral with the Langer reflection coefficient, which is a function of p and ω, is not valid. However, by excluding the second derivative of V_n in the expansion, we may still apply the basic technique to obtain analytic solutions to the Sommerfeld integral whose accuracy is improved over the results obtained by ray theory. The detailed derivations and justifications are discussed in Appendix B, and here we only introduce the necessary formulation to obtain the asymptotic solution to the Sommerfeld integral of the n-th term.

First, we must find a saddle point p_s which satisfies

$$\phi_n'(p_s) = -\frac{p_s}{\gamma_0}(z + z_0) + r + 2n\mu'(p_s) = 0 \qquad (2.40)$$

This is equivalent to locating an eigenray connecting two fixed points. In some cases, there could be well separated multiple saddle points(but not a caustic), found for the same source-receiver geometry.

Second, we deform the integration contour passing through the saddle point(s) along which the real part of ϕ is constant and the imaginary part is positive. Such a deformed contour is shown in Fig. 2.12. As a result, the complex exponential term now becomes a decaying term along this deformed contour with a maximum at the saddle point. There-

fore, if the amplitude of the integrand is a well behaved function, the integration may be approximated by integrating through a small domain near the saddle point (marked with ")(" in Fig. 2.12), and the rest of the contribution asymptotically becomes zero.

Next we expand the integrand in a Taylor expansion in p about p_s, and Eq. (2.35) becomes

$$P_n \cong \int_{-\infty}^{\infty} dp \left[F_n(p_s) + F'_n(p_s)(p - p_s) + \frac{1}{2} F_m''(p_s)(p - p_s)^2\right]$$

$$\times \exp i\omega\left[\phi_n + \frac{1}{2}\phi_n''(p - p_s)^2 + \frac{1}{3!}\phi_n'''(p - p_s)^3 + \frac{1}{4!}\phi_n^{IV}(p - p_s)^4\right], \quad (2.41)$$

and the asymptotic expansion of Eq. (2.34) due to the saddle point P_{ns} up to the second order term becomes[2]

$$P_{ns} \sim e^{i\pi/4}\sqrt{\frac{1}{r}}\, e^{i\omega[\gamma_0(z+z_0) + p_s r]}$$

$$\times \sqrt{\frac{-1}{i\phi''_n(p_s)}}\, R_n(p_s) \left(\frac{p_s}{\gamma_0}\right)^{1/2} \left[1 + \frac{1}{2\omega} N\right] \quad (2.42)$$

where

$$N = \left.\frac{\phi_n''' F'_n}{\phi''^2_n F_n} + \frac{1}{4}\frac{\phi_n^{IV}}{\phi''^2_n} - \frac{5}{12}\frac{\phi'''^2_n}{\phi''^3_n} - \frac{F''_n}{\phi'' F_n}\right|_{p_s} \quad (2.43)$$

with

$$\phi''_n = -\frac{z + z_0}{c_0^2 \gamma_0^3} + 2n\mu'' \quad (2.44)$$

$$\phi_n''' = -\frac{3\,(z + z_0)\,p}{c_0^2 \gamma_0^5} + 2n\mu''' \tag{2.45}$$

$$\phi_n^{IV} = -2(z + z_0)\,\frac{1 + 4\,p^2 c_0^2}{c_0^4\,\gamma_0^7} + 2n\mu^{IV} \tag{2.46}$$

$$\frac{F_n'}{F_n} = \frac{V_n'}{V_n} + \frac{1}{2p} + \frac{p}{\gamma_0^2} \tag{2.47}$$

$$\frac{F_m''}{F_n} = \frac{V_n'}{V_n}\left[\frac{2p}{\gamma_0^2} + p^{-1}\right] + 2\gamma_0^{-2} + \frac{3p^2}{\gamma_0^4} - \frac{1}{4p^2} \tag{2.48}$$

where for $n = 0$

$$\frac{V_0'}{V_0} = \frac{R_0'}{R_0} = \frac{2(A_0^{(2)'}B_0^{(2)} - A_0^{(2)}B_0^{(2)'})}{A_0^{(2)^2} - B_0^{(2)^2}} \tag{2.49}$$

and for $n > 0$

$$\frac{V_n'}{V_n} = -\frac{p}{\gamma_0^2} + \frac{(Q_0\nu_0^{-1/2})'}{Q_0\nu_0^{-1/2}} + (n-1)\,\frac{A_0^{(1)'} + B_0^{(1)'}}{A_0^{(1)} + B_0^{(1)}}$$

$$+ n\,\frac{A_H^{(2)'} - B_H^{(2)'}}{A_H^{(2)} - B_H^{(2)}} - (n+1)\,\frac{A_0^{(2)'} + B_0^{(2)'}}{A_0^{(2)} + B_0^{(2)}} - n\,\frac{A_H^{(1)'} - B_H^{(1)'}}{A_H^{(1)} - B_H^{(1)}} - 2ni\omega\mu_n' \tag{2.50}$$

where

$$A_0^{(1),(2)'} = -i\rho_1\left[\frac{p}{\gamma_0} W^{(1),(2)}(\nu_0) + \gamma_0 W'^{(1),(2)}(\nu_0)\,\nu_0'\right] \qquad (2.51a,b)$$

$$B_0^{(1),(2)'} = -\rho_0\left[S_0' W'^{(1),(2)}(\nu_0) + S_0\nu_0\nu_0'\, W_{1/2}(\nu_0)\right] \qquad (2.52a,b)$$

$$A_H^{(1),(2)'} = -i\rho_1\left[\frac{p}{\gamma_2} W^{(1),(2)}(\nu_H) + \gamma_2 W'^{(1),(2)}(\nu_H)\,\nu_H'\right] \qquad (2.53a,b)$$

$$B_H^{(1),(2)'} = -\rho_2\left[S_H' W'^{(1),(2)}(\nu_H) + S_H\,\nu_H\nu_H'\, W^{(1),(2)}(\nu_H)\right] \qquad (2.54a,b)$$

where
$$S_0 = Q_0\,\nu_0^{-1/2} \qquad (2.55a)$$

$$S_H = Q_H\,\nu_H^{-1/2} \qquad (2.55b)$$

The above formula, Eqs. (2.41) through (2.55), are also valid for complex sound velocities to include absorption. In this case, a complex saddle point must be found from Eq. (2.40) where the phase integral μ is evaluated for a complex turning depth z_t. We also point out that Eq. (2.41) is the contribution from a single saddle point. Thus, if more than a single saddle point exists, their contributions must be evaluated and summed.

If N is set equal to zero[cf. Eq. (2.42)], the result becomes a ray solution except R_n is more accurately evaluated by the L.U.A.A. It is necessary to include the correction term N in order to be consistent with the order of accuracy provided by the Langer formulation

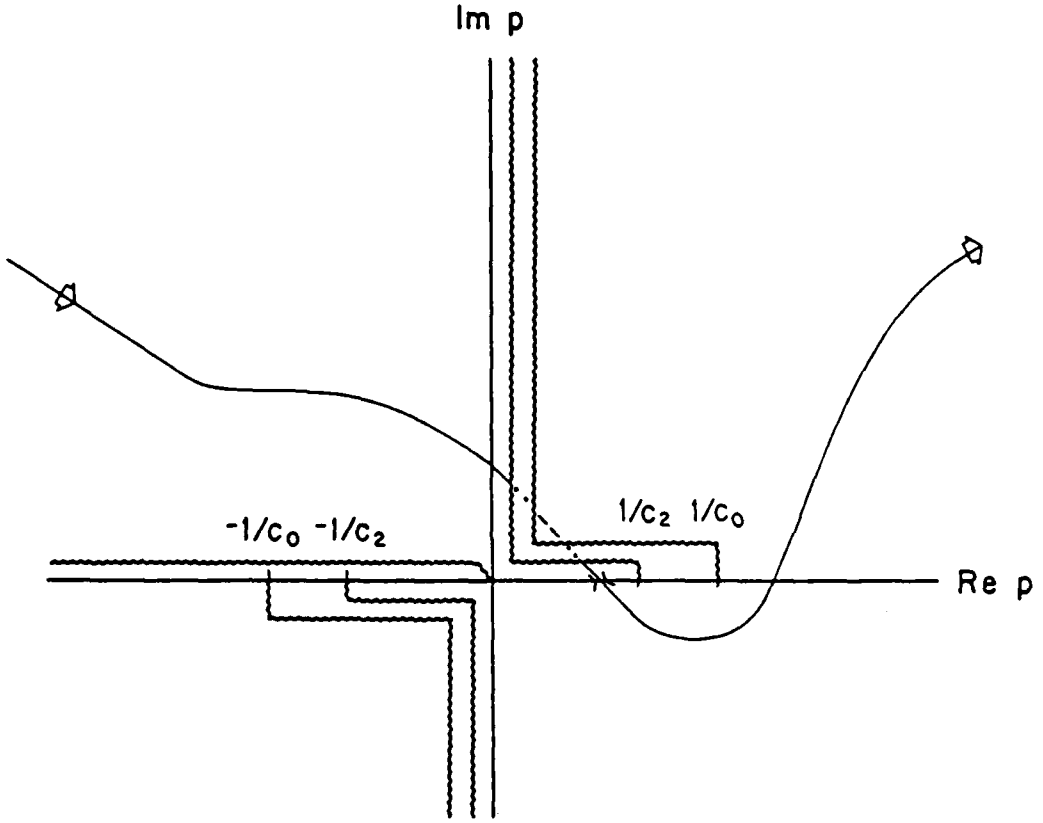

Fig. 2.12 The steepest descents path in the complex p-plane for a pre--critical incidence.

which is valid up to order $1/\omega$ (See Appendix A). However, using the same argument, evaluation of higher order terms in Eq. (2.42) or more accurate integration of Eq. (2.34) by a numerical method would not increase the accuracy of the result given by Eq. (2.42).

2.3.3 Interface Waves

Dealing with two different types of interfaces in our geoacoustic models, we consider two physically and mathematically different types of interface waves; one propagates along the ocean bottom interface where the medium containing the incident wave is homogeneous and overlies an inhomogeneous halfspace, while the other propagates along the ocean sub-bottom where the medium containing the incident wave is inhomogeneous and overlies a homogeneous halfspace.

The first type of interface waves, known as an interference head wave, has been extensively studied by Cerveny and Ravindra[5]. It is the result of a coherent sum of many multiples which have closely located shallow turning depths (cf. Fig. 2.13).

By definition[7], the interference head wave propagates along the interface such that the upper halfspace is homogeneous with the sound velocity c_0 and the lower halfspace has the acoustic property as $c_1(z) = a + bz$ where $a > c_0$ and $b, z > 0$. However, unless a limiting case where b approaches 0 in $c_1(z)$ is considered, the mathematical arguments are identical for the case where $c_1(0)$ is greater or less than c_0, and both are the contributions from the multiples.

We have observed that there are no additional branch points created as the result of the expansion of the total reflection coeffi-

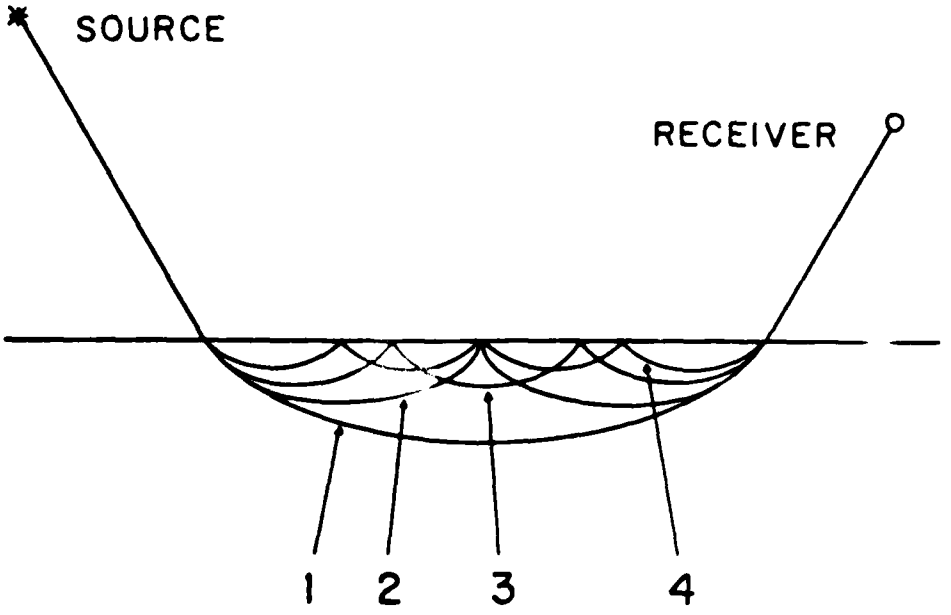

Fig. 2.13 Rays of multiples which turn at relatively shallow depths in the layer.

cient. Thus, unlike head waves from the branch cut contribution[4] for two homogeneous halfspaces, the interference head waves are special cases of the saddle point contributions to the total reflected field. Therefore, the amplitudes of the interference head waves are proportional to the reciprocal of the range, not the range squared.

The presence of the second type of interface wave is due to the branch cut contribution as the S.D.P. crosses the branch point at $p = 1/c_2$ (but never at $p = 1/c_0$), and the contour must be deformed to go around this branch cut so that the end points of the integration path may remain on the correct Riemann sheet(cf. Fig. 2.14). The technique to evaluate the asymptotic behavior of the contour integration around the branch cut is completely analogous to that of Lamb's problem[1], [12] where the method of steepest descents is applied. The asymptotic approximation of the interface wave due to the n-th multiple including the primary reflection, P_{nL} is given, as expected, by

$$P_{nL} \sim \frac{8i}{\pi^2 \omega}\left[\frac{(-B_H^{(1)}B_H^{(2)})(A_0^{(1)}+B_0^{(1)})}{A_0^{(2)}+B_0^{(2)}}\right]^{n-1} \frac{\rho_0\rho_1^2\rho_2 S_0 S_H}{r^{1/2}(nL)^{3/2}c_2}$$

$$\times \frac{e^{i\omega[\gamma_0(z+z_0)+r/c_2]}}{(A_0^{(2)}+B_0^{(2)})^2(A_H^{(1)2}-B_H^{(1)2})^n} \qquad (2.56)$$

where L is the horizontal distance the interface wave propagates along the subbottom for each subbottom interaction(cf. Fig. 2.15). As r becomes large so does nL, and P_{nL} algebraically decays proportional to $1/r^2$. Although Eq. (2.56) is the leading order term of the asymptotic

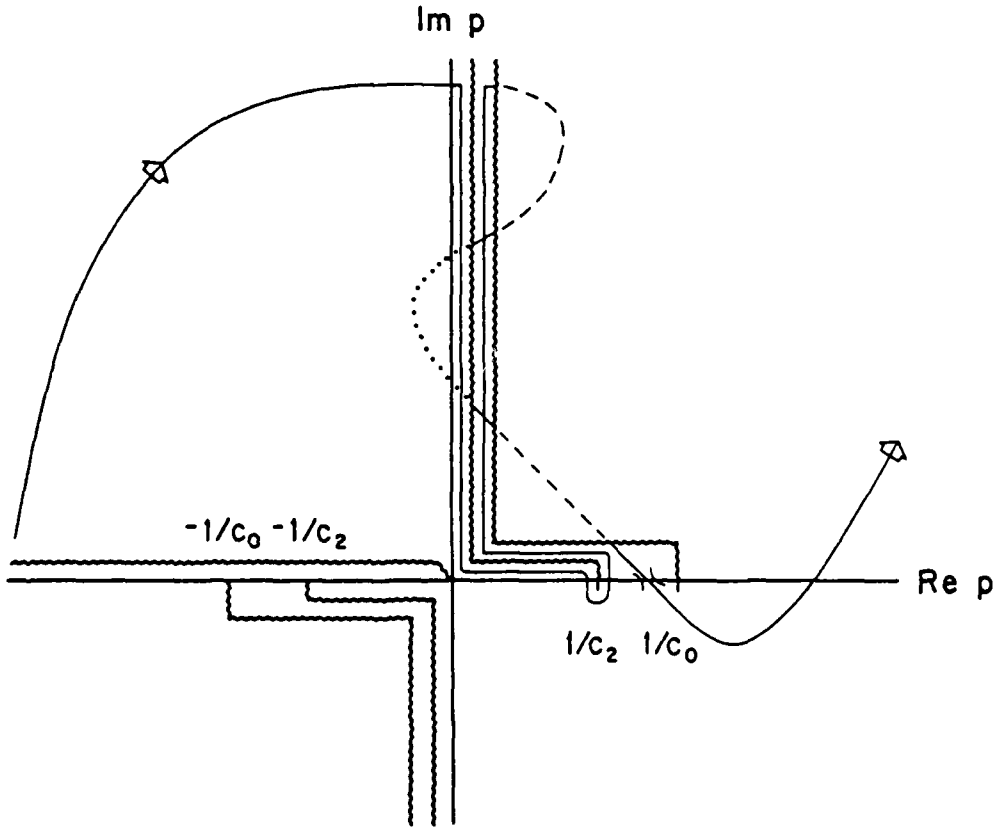

Fig. 2.14 The branch cut integration contour for a post critical incidence.

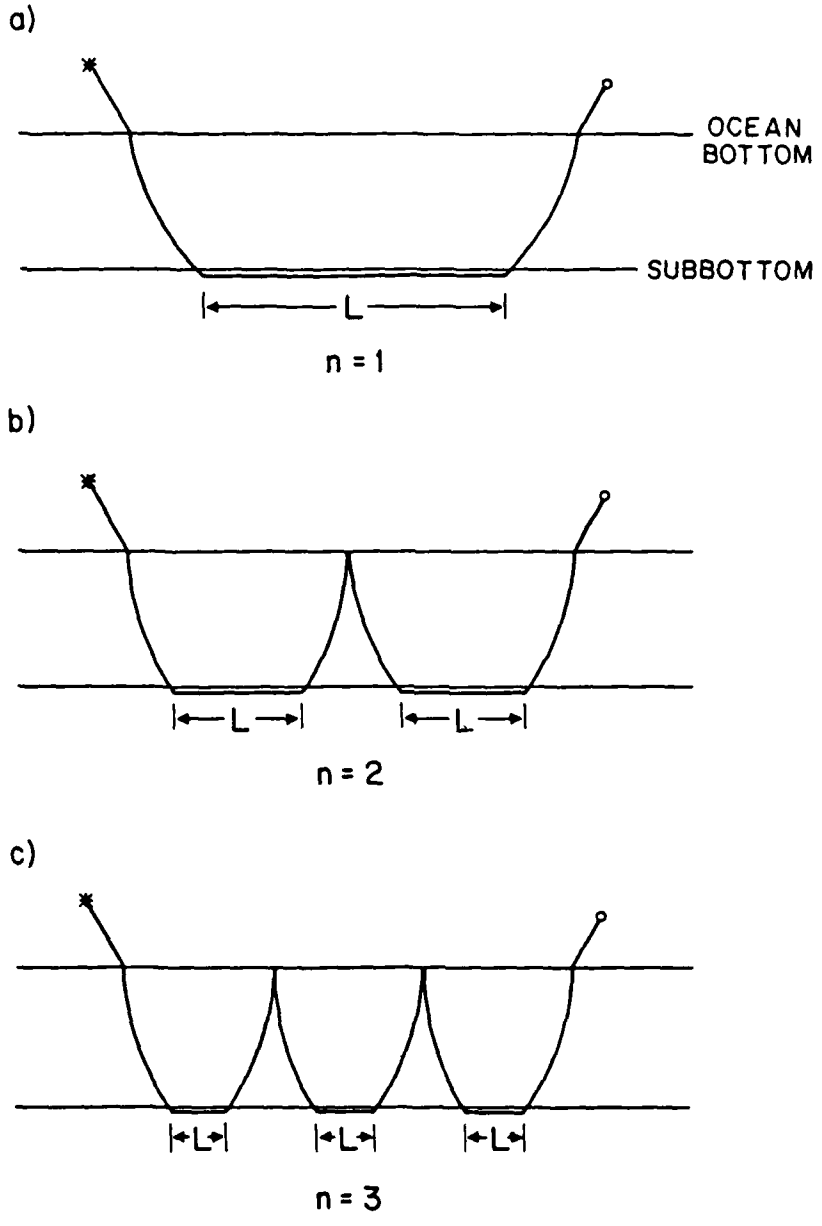

Fig. 2.15 Ray interpretation of the interface waves propagating along the subbottom interface. (a) The primary reflection, (b) the 2nd multiple reflection and (c) the 3rd multiple reflection.

expansion of P_{nL} , it is of order $1/\omega$. Thus, this is all we can expect from the Langer reflection coefficients.

The total subbottom interface wave contribution is given by the sum of the branch cut contributions of P_{nL} as their S.D.P.'s cross the branch point. Again, like the saddle point contribution, Eq. (2.56) is valid for any inhomogeneous layer as long as it satisfies the conditions necessary for the Langer reflection coefficient.

2.4 Limitation of the Asymptotic Expansion of P_n

The total reflected fields at two different values of $z + z_0$ are computed from the geoacoustic model shown in Fig. 2.7. The results are compared to the ones generated by a numerical Hankel transform method [12](cf. Fig. 2.16). They show good agreement except at a few rigions of horizontal ranges where the asymptotic solutions to the primary and multiple reflections break down at the critical incidence and caustics.

As discussed in Secs. 2.3.1 and 2.3.2, in order for the method of steepest descents to be valid, F(p) must be a smooth well-behaved function. Although F(p) can be made sufficiently smooth at most incident angles by separating out the complex phase term, the rapid change in amplitude and phase near critical incidence is still a problem. Since $V'_n(p)$ at critical incidence becomes large, the correction term N becomes unstable. This is also true for reflections at very small grazing angles. The second problem is that N blows up as $\phi''(p_s)$ approaches zero. This is the condition corresponding to caustic formation.

In the complex p-plane, the first problem is due to the fact that the saddle point is located too close to the branch point, $1/c_2$ or $1/c_0$.

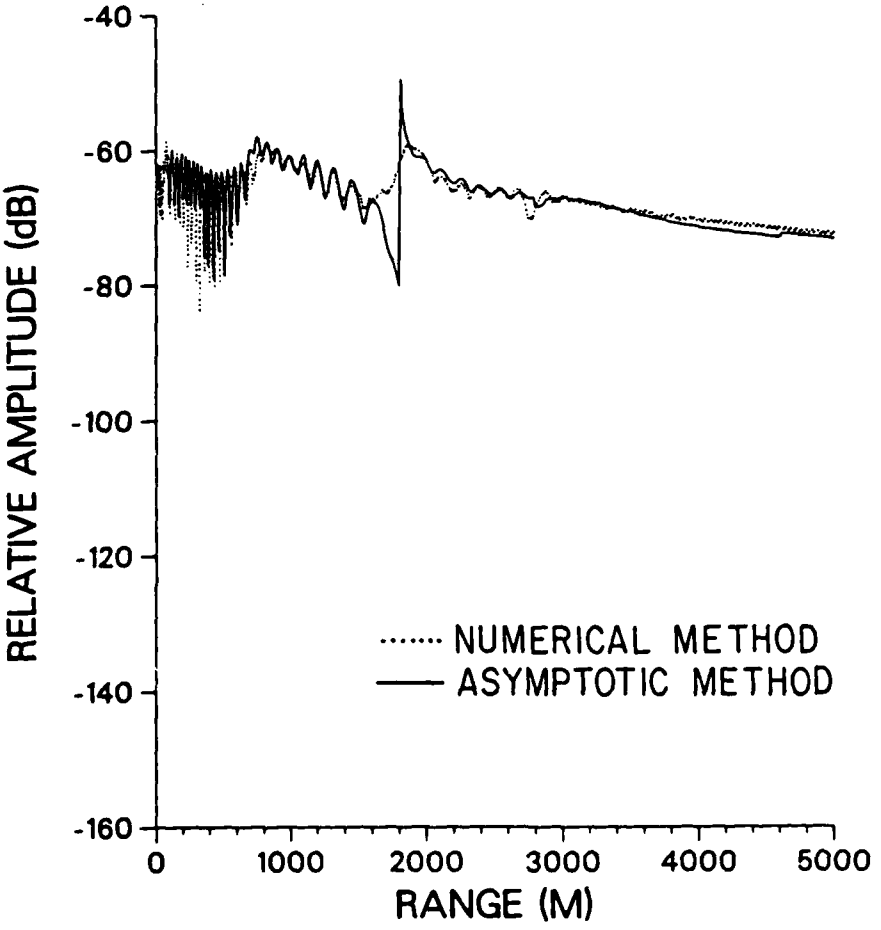

Fig. 2.16a A comparison between the asymptotic method and the numerical Hankel transform method at $z + z_0 = 250$ m for the geoacoustic model shown in Fig. 2.2.

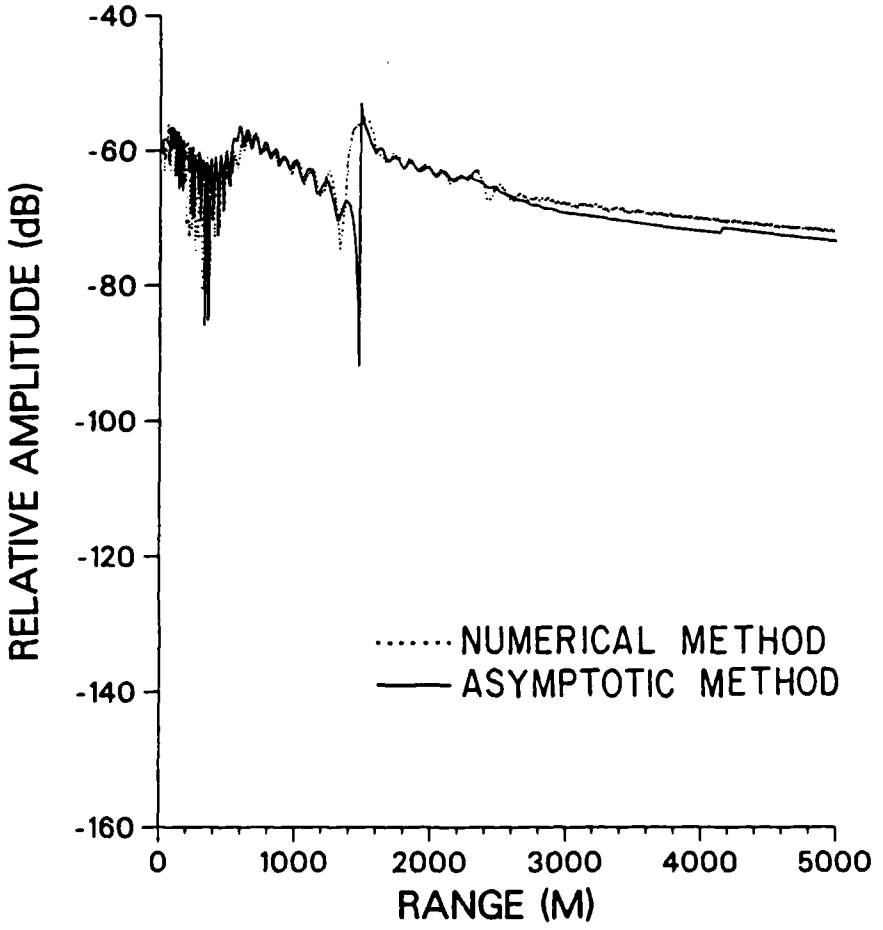

Fig. 2.16b A comparison between the asymptotic method and the numerical Hankel transform method at $z + z_0 = 150$ m for the geoacoustic model shown in Fig. 2.2.

For the second problem, the S.D.P. passing through the saddle point is no longer a straight line near the saddle point, but branches out with $\pi/3$ angles (cf. Fig. 2.17). Thus the expansion along the straight line(cf. Fig. 2.12), which resulted in Eq. (2.41), is no longer valid at the caustic saddle point and breaks down.

For either case another alternative must be taken in order to evaluate P_n for such regions of p. A uniform asymptotic expansion of the integral across the critical points [3] may be applied for these cases, but it is very difficult to obtain any physical interpretation from the results which involve special functions. Thus, the argument for obtaining analytic solutions for these special conditions becomes very weak. Therefore, our choice here is to numerically integrate along a slightly modified S.D.P. as shown in Fig. 2.18 under these circumstances.

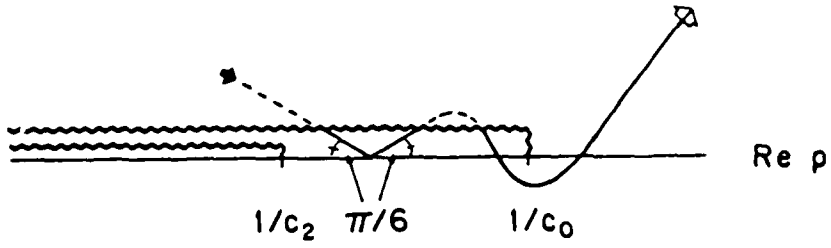

Fig. 2.17 The steepest descents for a saddle point corresponding to a caustic field.

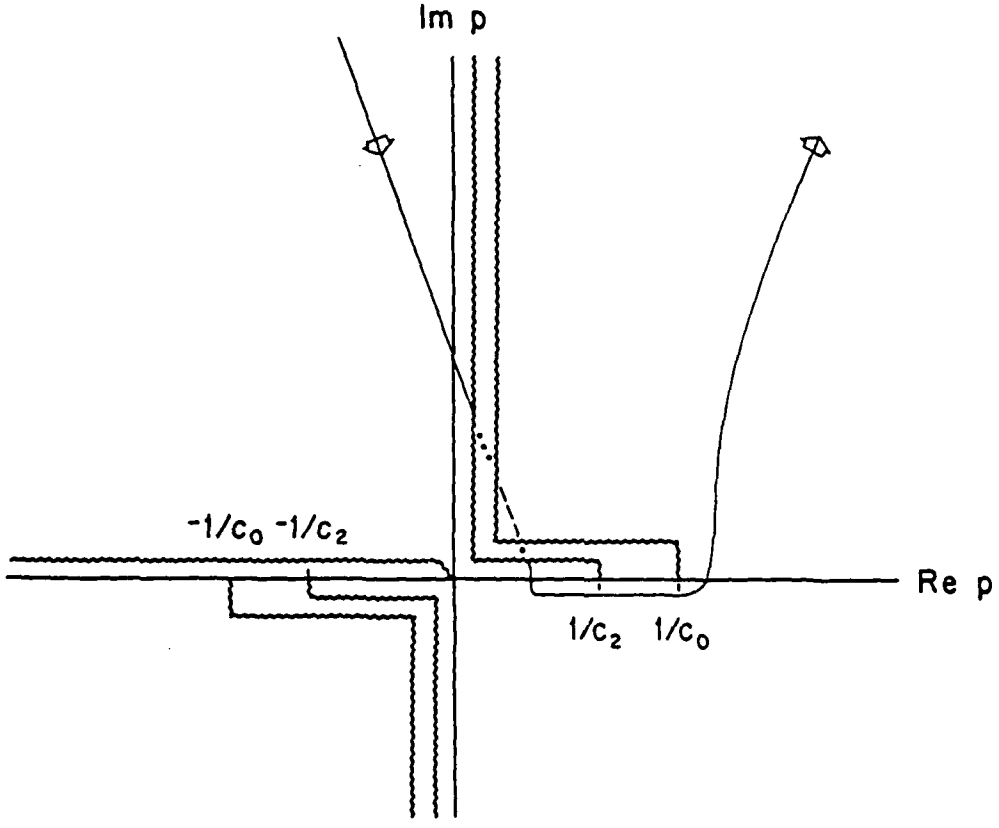

Fig. 2.18 A suggested deformed contour for a numerical evaluation of the Sommerfeld integral.

References:

[1] Aki, K. and Richards, P. G., Quantitative Seismology-Theory and Methods, Vol. 1, Freeman, San Francisco, 1980.

[2] Bender, C. M. and Orszag, S. A., Advanced Mathematical Methods for Scientists and Engineers, McGraw-Hill, New York, 1978.

[3] Bleistein, N. and Handelsman, R. A., Asymptotic Expansions of Integrals, Holt, Rinehard and Winston, New York, 1975.

[4] Brekhovskikh, L. M., Waves in Layered Media, 2nd ed., Academic Press, New York, 1980.

[5] Bucker, H. P., "Sound Propagation in a Channel with Lossy Boundaries," J. Acoustical Soc. Amer. 48, 1187-1194 (1970).

[6] Budden, K. G., Radio Waves in the Ionosphere, Cambridge University Press, Cambridge, 1961.

[7] Cerveny, V. and Ravindra, R., Theory of Seismic Head Waves, University of Toronto Press, Toronto, 1971.

[8] Ewing, W. M., Jardetzky, W. S. and Press, F., Elastic Waves in Layered Media, McGraw-Hill, New York, 1957.

[9] Fock, V. A., Electromagnetic Diffraction and Propagation Problems, Pergamon Press Ltd., London, 1965.

[10] Langer, R. E., "Asymptotic solutions of a differential equation in the theory of microwave propagation," Commun. Pure Appl. Math. 3, 427-438 (1950).

[11] Tamir, T. and Felsen, L. B., "On Lateral Waves in Slab Configurations and Their Relation to Other Wave Types", IEEE Trans. Ant. Propag. AP-13, 410-422, (1965).

[12] Reference[4] pp. 241-252.

[13] Wengrovitz, M. S., private communication.

Chapter 3: Geoacoustic Models and Reflected Fields

In Sec. 2.1 the total plane wave reflection coefficients for our geoacoustic models were derived using the Langer Uniform Asymptotic Approximation (L.U.A.A.). Then, using the Langer reflection coefficients, we derived reflected fields due to a time harmonic point source in Sec. 2.3. We shall next derive the phase integrals for the profile shapes of interest.

After examining the full analytic solutions for the reflected fields, particularly the asymptotic behavior of the fields at long ranges, we can estimate important parameters to study various cases. We shall then apply the above results to study energy partitioning of eigenrays for the ocean bottom geoacoustic models.

3.1. Profile Types in the Sediment Layer

The formulae for the reflection coefficient given by Eq. (2.20) and the asymptotic expansion of the reflected fields given by Eq. (2.42) through (2.59) are all based on an ocean bottom geoacoustic model consisting of a layer with a slowly varying sound velocity (of any shape) above a homogeneous infinite halfspace. Therefore, the only parameter which must be found is the phase integral η defined by Eq. (2.5). This quantity may be calculated numerically, but it is instructive to derive, where possible, an analytic expression in order to obtain full analytic solutions for the reflected fields and to investigate the physical effects of the geoacoustic parameters upon the reflected fields. We shall

limit our cases to three different profile shapes for which analytic expressions for the phase integral and its derivatives are obtainable.

a) $1/c_1^2$-Linear Profile

For this case

$$\frac{1}{c_1^2(z)} = a_1 z + b_1 \tag{3.1}$$

where a_1 and b_1 are arbitrary parameters. This profile type is one of the most commonly used for modeling slowly varying inhomogeneous media because exact analytic solutions for the field are available in the form of Airy functions. Also, the Langer reflection coefficients become exact for this profile type as E(z) in (2.3) vanishes everywhere. Even though one might argue that the shape of this profile does not necessarily represent actual profile shapes observed in real ocean bottom sediments, it will be shown in Sec. 3.2.3 that this is a good approximation to the correct ones as long as the layer thickness and sound velocity gradient are small.

The analytic expressions, for the first, second, third and fourth-order derivatives of eta with respect to p for this profile type are given below:

$$\eta_1 = \frac{2}{3a_1} Q^3 \tag{3.2}$$

$$\frac{d\eta_1}{dp} = -\frac{2p}{a_1} Q \tag{3.3}$$

$$\frac{d^2\eta_1}{dp^2} = \frac{2}{a_1 c_1^2(z)} \frac{2p^2 c_1(z) - 1}{Q} \tag{3.4}$$

$$\frac{d^3\eta_1}{dp^3} = \frac{2p}{a_1 c_1^2(z) Q^3} [3 - 2p^2 c_1^2(z)] \tag{3.5}$$

$$\frac{d^4\eta_1}{dp^4} = \frac{b}{a_1 c_1^4(z) Q^5} \tag{3.6}$$

where $Q = [1/c_1^2(z) - p^2]^{1/2}$.

b) c_1-linear Profile

For this case

$$c_1(z) = a_2 z + b_2 \tag{3.7}$$

where a_2 and b_2 are arbitrary parameters.

This is another common profile shape, a straight line between two fixed endpoints. Formulae for the phase integral and derivatives for this profile are given by

$$\eta_2 = \frac{1}{a_2} [c_1(z)Q - \ln(\frac{1 + c_1(z)Q}{pc_1(z)})] \tag{3.8}$$

$$\frac{d\eta_2}{dp} = \frac{c_1(z)Q}{a_2 p} \tag{3.9}$$

$$\frac{d^2 n_2}{d p^2} = - (a_2 c_1(z) Q p^2)^{-1} \tag{3.10}$$

$$\frac{d^3 n_2}{d p^3} = - \frac{1}{a_2 c_1(z) p} \left(\frac{1}{Q^2} - \frac{2}{p^2}\right) \tag{3.11}$$

$$\frac{d^4 n_2}{d p^4} = - \frac{3}{a_2 c_1(z) p^4 Q^5} (2Q^4 - p^2 Q^2 + p^4) \tag{3.12}$$

c) c_1^3-Linear Profile

For this case

$$c_1^3(z) = a_3 z + b_3 \tag{3.13}$$

where a_3 and b_3 are arbitrary parameters.

This rather unusual linear expression for the sound velocity is added to our analysis in order to investigate more realistic geoacoustic models derived from measurements[3]. The sound velocity in the bottom may be given as a function of one-way travel time t from direct measurements and is often expressed in terms of polynomials in t. From these expres- sions, Hamilton has studied sonobuoy bottom reflection data and statis- tically obtained a form for the sound velocity as a function of depth which he fitted with third-order polynomials[2]. As seen in Fig. D.1, the major characteristic of the "Hamilton profile" is that the sound velocity gradient near the ocean bottom is larger than that of the deep- er portion of the profile - this is just the opposite of the behavior for the case of the $1/c_1^2(z)$-linear profile.

It has been found by the author that the "Hamilton profile" may be

well approximated by a simple linear expression as introduced here. From the given coefficients of a third-order polynomial in t, one may obtain a_3 and b_3 in (3.13) from the formula provided in Appendix D. Their agreement is quite good even in the deep portion of the profile where the maximum error is expected (See Fig. D.1). The validity of this rather simple approximation is also discussed in Appendix D.

The analytic expressions for η and its derivatives may be easily obtained and are given by

$$\eta_3 = -\frac{c_1^3(z)Q^3}{a_3 p^2} \tag{3.14}$$

$$\frac{d\eta_3}{dp} = \frac{c_1(z)Q}{a_3 p}\left[2p^{-2} + c_1^2(z)\right] \tag{3.15}$$

$$\frac{d^2\eta_3}{dp^2} = -\frac{3}{a_3 p^4 c_1(z)Q}\left[2 - p^2 c_1^2(z)\right] \tag{3.16}$$

$$\frac{d^3\eta_3}{dp^3} = -\frac{3}{a_3 c_1(z) p^5 Q^3}\left[12p^2 - 3p^4 c_1^2(z) - \frac{8}{c_1^2(z)}\right] \tag{3.17}$$

$$\frac{d^4\eta_3}{dp^4} = -\frac{3}{a_3 c_1(z) p^6 Q^3}\left[20Q^2 + 19c_1^2(z)Q^4 - 4p^2 + 7p^2 c_1^2(z)Q^2\right] \tag{3.18}$$

Similarly, a profile whose form is c^M-linear with M = 2, 4 or 5 also provides simple analytic expression for the phase integral. The general rule is that the greater M is, the greater the gradient near the ocean bottom. These profiles may be used instead of the c^3-linear form, depending on the size of the curvature of the profile shape to be

modeled. We choose to study the c^3-linear profile because it demonstrates the best agreement with the measurements reported by Hamilton.

In order to study the effects due solely to the profile shapes, we fix the end points of the profiles so that the difference in characteristic acoustic impedance across each interface remains the same. Once the endpoints of the sound velocity in the layer are fixed, the coefficients of the linear equation for each profile shape are automatically fixed.

3.2 Important geoacoustic parameters in modeling

In this section, applying the mathematical results obtained in Chapter 2 and profile shapes chosen for the layer in Sec. 3.1, we shall discuss the effects of geoacoustic parameters on the reflected fields and thus establish guidelines to choose appropriate examples of geoacoustic models. Since we have obtained closed forms for the reflected fields based on the geoacoustic models, we can discuss the direct parametric dependence of our solutions for some limiting cases.

The major quantities which are primarily responsible for the field amplitudes for a given geoacoustic model are $\phi''^{-1/2}(p_s)$ and $R_n(p_s)$ [cf. Eq. (2.42)]. The first one controls the geometric spreading and the other the amplitude of the plane wave corresponding to the particular saddle point. Since we have fixed the endpoints of the layer profile in modeling, the boundary conditions at both of the interfaces remain the same. This leads to the condition that the asymptotic behavior of the amplitude of the reflection coefficient R_n is independent of the profile shape as derived in Eqs. (2.31) and (2.32).

Therefore, ϕ'' is the only quantity which sensitively responds to the change in profile shape for fixed boundary conditions. In order to investigate how related geoacoustic parameters affect this quantity, we shall next examine the analytic expression of ϕ'' for a limiting case, though its behavior is valid for a large portion of horizontal ranges where the incident angle approaches grazing.

3.2.1 Geometric Spreading Near Grazing Incidence

In this subsection we shall demonstrate from the profile shapes we have chosen that ϕ'' strongly depends on the sound velocity gradient at the top of the layer and becomes independent of the profile shape near grazing incidence.

When an eigenray of a primary or multiple reflection enters the ocean bottom near grazing, it turns within the layer at relatively shallow depth. The associated phase integral is calculated by integrating from $z = z_t$ to $z = 0$. Let us consider $d^2\phi/dp^2$ for the $1/c_1^2$-linear profile case

$$\phi'' = -\frac{z + z_0}{c_0^2 \gamma_0^3} + 2n \left.\frac{d^2\eta_1}{dp^2}\right|_{z=0} \tag{3.19}$$

where the first term corresponds to the water path and the second term corresponds to the layer-path given by Eq. (3.4). After replacing p and Q with $c_1(z)/\cos\alpha_1$ and $c_1(z)/\sin\alpha_1$ respectively, we rewrite Eq. (3.4) as

$$\left.\frac{d^2\eta_1}{dp^2}\right|_{z=0} = -\frac{2}{a_1 c_1(0)} \frac{2\cos^2\alpha_1 - 1}{\sin\alpha_1} \tag{3.20}$$

where α_1 is the grazing angle in the layer at z = 0. We next differentiate both sides of Eq. (3.1) with respect to z to obtain

$$\frac{2}{a_1 c_1(0)} = -\left.\frac{c_1^2(0)}{\frac{d c_1}{d z}}\right|_{z=0}. \tag{3.21}$$

After we substitute Eq. (3.21) in Eq. (3.20), we obtain

$$\left.\frac{d^2\eta_1}{d p^2}\right|_{z=0} = -\frac{c_1^2(0)}{\frac{dc_1(0)}{dz}\sin\alpha_1}(2\cos^2\alpha_1 - 1). \tag{3.22}$$

Since we are considering the case of small grazing incidence, the small angle approximations to the leading order terms may replace the trigonometric functions and Eq. (3.22) becomes

$$\left.\frac{d^2\eta_1}{a p^2}\right|_{z=0} \sim -\frac{c_1^2(0)}{\frac{dc_1(0)}{dz}\alpha_1}. \tag{3.23}$$

The minus sign is due to the fact that positive z is defined to be upward in the water column, and therefore the velocity gradient in the layer is negative.

Interestingly, the expressions derived for $d^2\eta/dp^2$ for the c_1-linear and c_1^3-linear profiles become identical to the one given by Eq. (3.23) when small angle approximations are made. Since we have fixed $c_1(0)$ (and $c_1(h)$) for all profile shapes, the only variable is the

sound velocity gradient at the ocean bottom for the rays which completely turn within the layer.

The effect of this is expected to be more critical when the sum of the source and receiver heights is sufficiently small so that the first term on the right hand side of Eq. (3.19) does not dominate ϕ''. In order to quantitatively determine the condition where the water-path term does not dominate ϕ'', we shall again consider the case of small grazing incidence and assume that $c_0 \equiv c_1(0)$ at the bottom. Then, we obtain from Eq. (3.19) that

$$z + z_0 << 2n\,\alpha^2 c_0/(dc_1(0)/dz) \tag{3.24}$$

where α is the grazing angle of the n-th multiple in the water column.

For a gradient of 1 s^{-1}, the right hand side of Eq. (3.24) becomes less than 100 m for the primary reflection(n = 1). As the order of the multiple reflection increases, i.e. n in Eq. (3.19) increases and/or the sound velocity gradient at the bottom decreases, the layer-path contribution increases. Therefore, a larger value for $(z + z_0)$ satisfies Eq. (3.24).

3.2.2 Geoacoustic Models with Large Layer Thickness

We have just learned that geometric spreading, particularly at long ranges, is strongly affected by the sound velocity gradient at the bottom. In order to obtain a wide range in the sound velocity gradients among the three profile shapes, while keeping the same boundary conditions at both interfaces, one must have a relatively large layer thick-

ness and sound velocity gradient.

For the given endpoints, the sound velocity gradients of the $1/c_1^2$ and c_1^3-linear profiles are given in terms of the endpoint-sound velocities, $c_1(0)$ and $c_1(H)$ by

$1/c_1^2$-linear:
$$\frac{dc_1(0)}{dz} = -\frac{c_1^3(0)}{2H}\left[c_1^{-2}(H) - c_1^{-2}(0)\right] \tag{3.25}$$

c_1^3-linear:
$$\frac{dc_1(0)}{dz} = \frac{c_1^{-2}(0)}{3H}\left[c_1^3(H) - c_1^3(0)\right], \tag{3.26}$$

respectively, where H is the layer thickness.

We next define a "reference gradient" g by the gradient of the c_1-linear profile since it is constant throughout the layer. Then, $c_1(H)$ is given by

$$c_1(H) = Hg + c_1(0). \tag{3.27}$$

After the above expression for $c_1(H)$ is substituted, Eqs. (3.25) and (3.26) become

$$\frac{dc_1(0)}{dz} = \frac{c_1(0)}{2H}\left\{1 - c_1^2(0)[Hg + c_1(0)]^{-2}\right\} \tag{3.28}$$

$$\frac{dc_1(0)}{dz} = \frac{c_1^{-2}(0)}{3H}\left\{[Hg + c_1(0)]^3 - c_1^3(0)\right\}, \tag{3.29}$$

respectively. Now it can be easily shown for both expressions for the gradient $dc_1(0)/dz$ that

$$\frac{dc_1(0)}{dz} \to 0 \qquad \text{as } g \to 0 \qquad \text{for any H,} \tag{3.30}$$

and

$$\frac{dc_1(0)}{dz} \to g \qquad \text{as } H \to 0. \tag{3.31}$$

Therefore, if g and/or H become small, the variations in the velocity gradient at the bottom and thus the entire profile shapes become close to one another.

Fig. 3.1 shows the three profile shapes between fixed end points in the layer whose thickness is 500 m with $g = 1.5\ s^{-1}$. For this example the gradients of $1/c_1^2$, c_1 and c_1^3-linear profiles at the bottom are $0.8333\ s^{-1}$, $1.5\ s^{-1}$ and $2.375\ s^{-1}$ respectively. However, if the layer thickness is reduced to 50 m, they become $1.395\ s^{-1}$, $1.5\ s^{-1}$ and $1.576\ s^{-1}$, respectively, for the same reference gradient at the bottom. When g is small, the differences in sound velocity gradient become smaller even though the layer thickness is increased to 500 m (cf. Fig. 3.2).

One interesting non-dimensional parameter of our geoacoustic model is the layer thickness divided by the average wavelength, denoted by $H/\langle\lambda_1\rangle$. A large layer thickness not only provides substantial variations among profile shapes between the endpoints but also sets a large value for this parameter for reasonably high frequencies. The other extreme case, namely the layer thickness being comparable to or even smaller than the wavelength, is also of interest and we shall examine

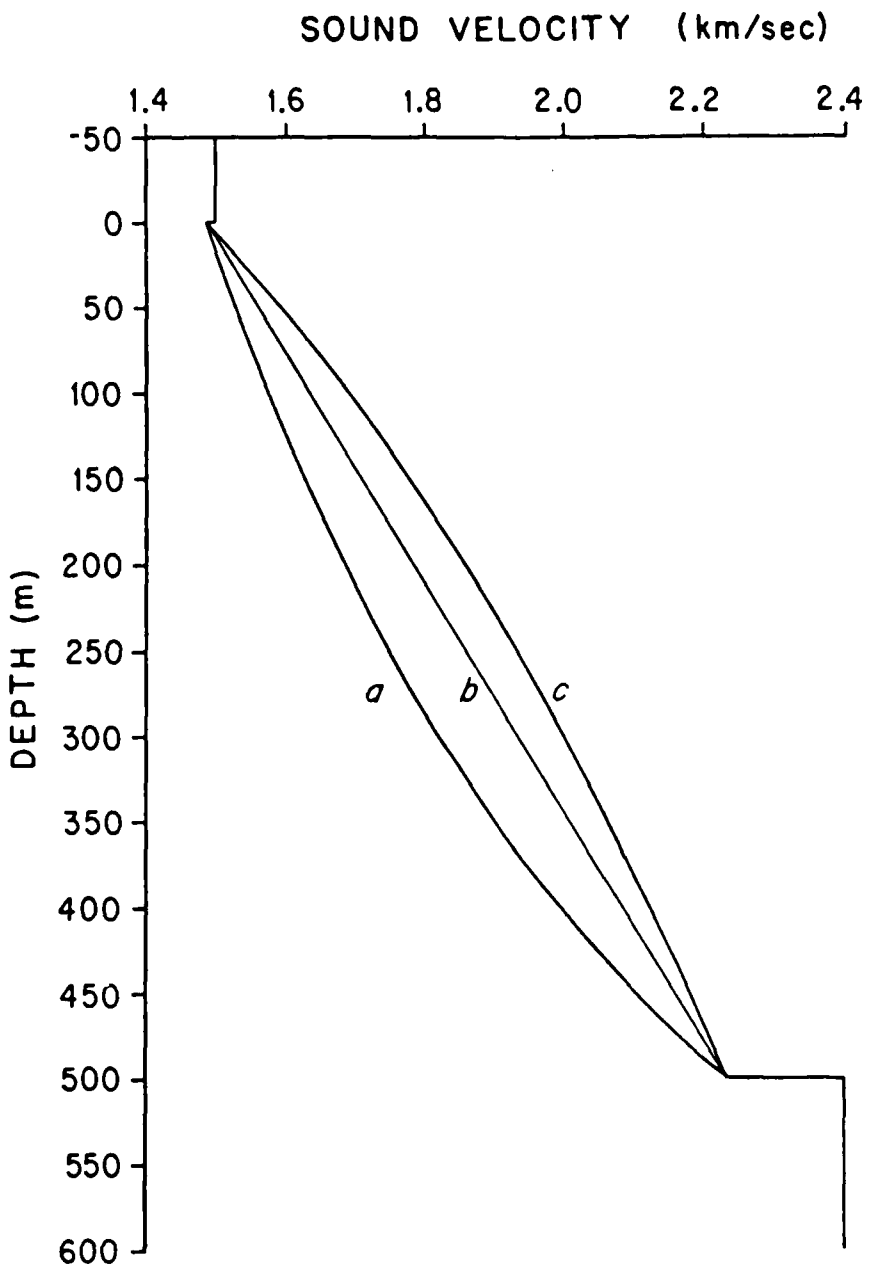

Fig. 3.1 Three different profile shapes for g = 1.5 s^{-1}. (a) The $1/c^2$, (b) c and (c) c^3-linear types.

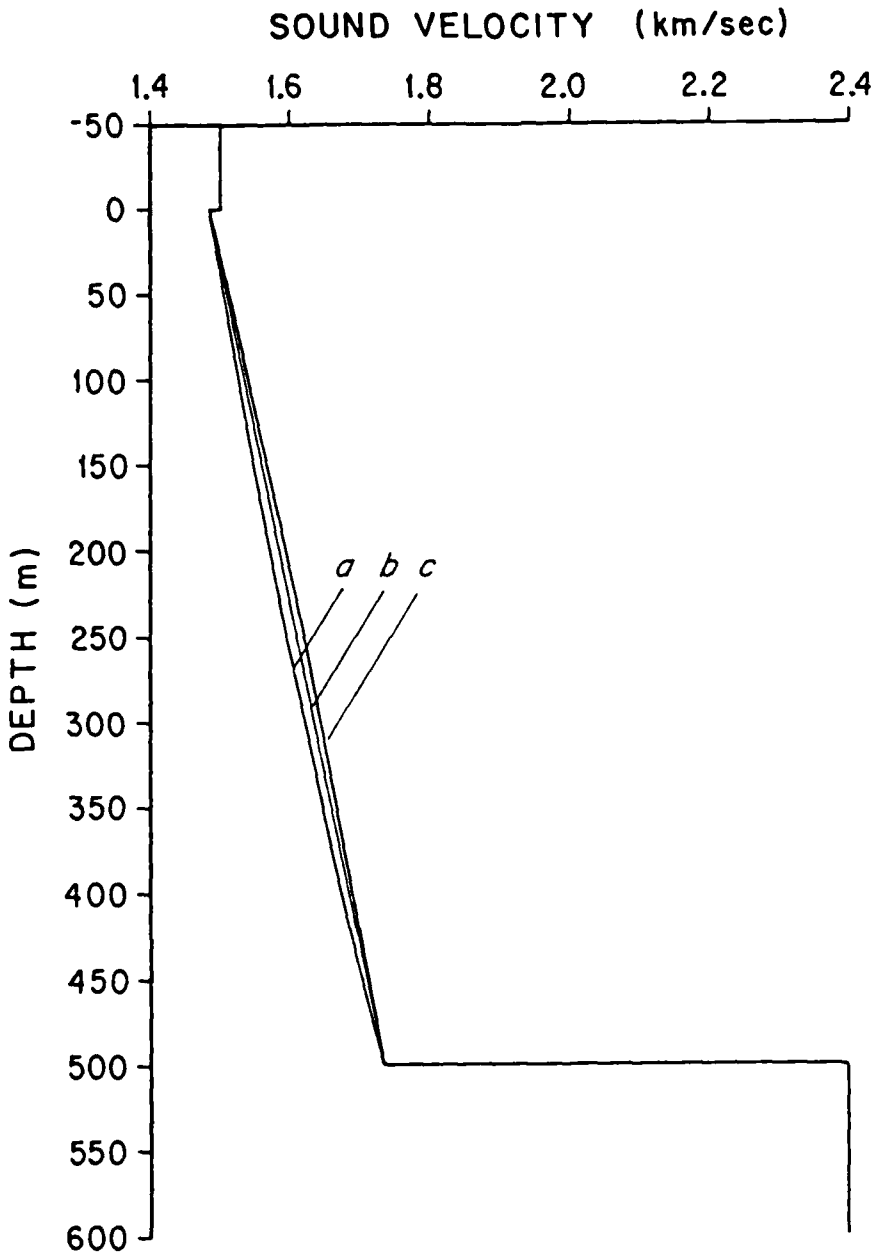

Fig. 3.2 Three different profile shapes for g = 0.5 s^{-1}. (a) The $1/c^2$, (b) c and (c) c^3-linear types.

geoacoustic models whose layer thicknesses are varied according to the size of this quantity in Sec. 3.3.

3.2.3 Geoacoustic models

While we shall use a large layer in order to study the effects of different profile shapes, we shall model a small layer with a single profile type since the exact profile shape does not matter much for fixed endpoint velocities and a small layer thickness. We shall choose the $1/c_1^2$-linear profile for thin layer cases since for this profile the Langer reflection coefficients become exact.

Based on the modeling considerations discussed in this section, we propose studying the following geoacoustic models, where we also assume a one percent sound velocity drop at the top of the layer, a phenomenon often encountered in deep ocean bottom experimental data[1]:

Model I: Thin layer model with a 5-m layer and a 2 s^{-1}-gradient

Model II: Small layer models with a 50-m layer and
- a) a 0.5 s^{-1}-gradient,
- b) a 1.5 s^{-1}-gradient.

Model III: Thick layer model with a 500-m layer,
a .5 s^{-1}-reference gradient, and
- a) a $1/c^2$-linear profile,
- b) a c^3-linear profile.

Model IV: Thick layer model with a 500-m layer,
a 1.5 s^{-1}-reference gradient, and
a) a $1/c^2$-linear profile
b) a c^3-linear profile

The quantity $H/\langle\lambda_1\rangle$ is 0.1, 1 and 10 for Models I, II, and III and IV, respectively.

3.3 Reflected Fields for The Geoacoustic Models

We still have to fix two more parameters in our examples, namely the source frequency and the source-receiver geometry. Regarding the source frequency, relatively high frequencies must be used in order for the asymptotic expansion to be valid. A frequency of 220 Hz is used for all of the examples since it is the frequency that has been used in the field experiments by Frisk[1].

The value of the sum of the source and receiver heights off the ocean bottom Z is defined as

$$Z = z + z_0.$$

This has also been varied in actual field experiments, the typical range being 125-250 meters from the ocean bottom. For the reflected fields this is a single parameter. If the direct field due to the water path is included in the total fields, the source and receiver heights must be given separately.

The reflected fields are grouped into three different ray types; the

specular reflection, primary reflection and multiple reflections. A schematic of these rays is shown in Fig. 3.3. The total reflected field is evaluated from the coherent sum of all of the above fields.

In order to obtain the reflected fields due to the multiples the infinite series of Sommerfeld integrals for the multiples may be truncated at the m-th term so that the following condition holds:

$$\sum_{j=0}^{m} R_j \cong \sum_{j=0}^{\infty} R_j = R_{TOTAL};\ 0 < p_{s_j} < p_{s_0} \qquad (3.31)$$

where p_{s0} is the saddle point for the specularly reflected field and p_{sj} is the saddle point for the j-th multiple. This is a more rigorous truncation criterion than truncating the terms whose contributions are below a certain level after each of the multiple fields is computed because it guarantees that the total reflection coefficient in the Sommerfeld integral is well approximated before the integration is evaluated.

3.3.1 Model I: Geoacoustic Model with Thin Layer

A geoacoustic model with a 5-meter thick layer and a sound velocity gradient of 2 s^{-1} (cf. Fig. 3.4) was used to generate the reflected fields for Z = 100 m as shown in Fig. 3.5. Since the layer thickness is smaller than the average wavelength in the layer (6.77 m), pure ray theory should not work well. Even though the use of ray theory may not be valid in interpreting the reflected fields, the ray theory based expansion of the total reflection coefficient is still valid and we can still evaluate each of the Sommerfeld integrals for the R_n's.

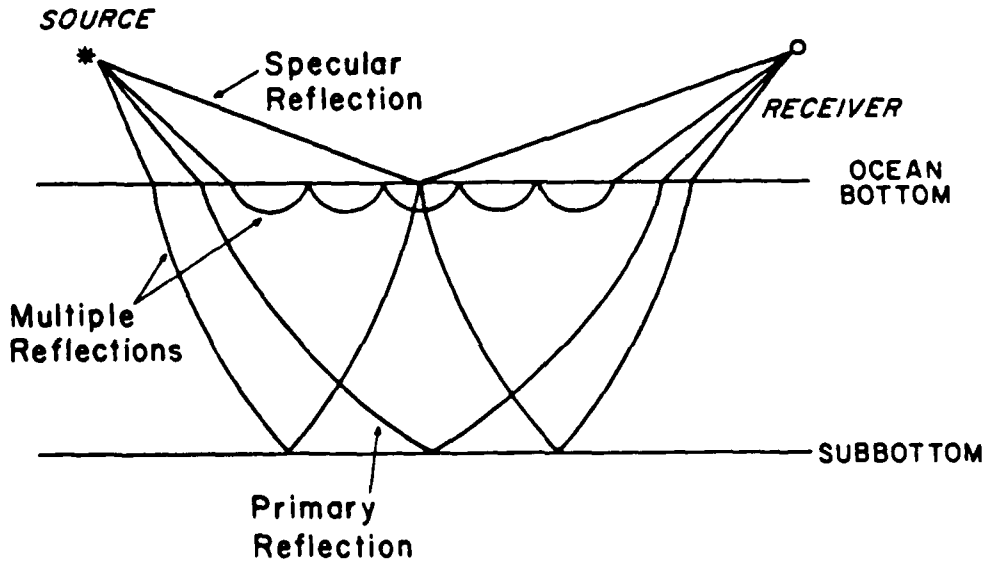

Fig. 3.3 Typical reflecting rays in the geoacoustic model.

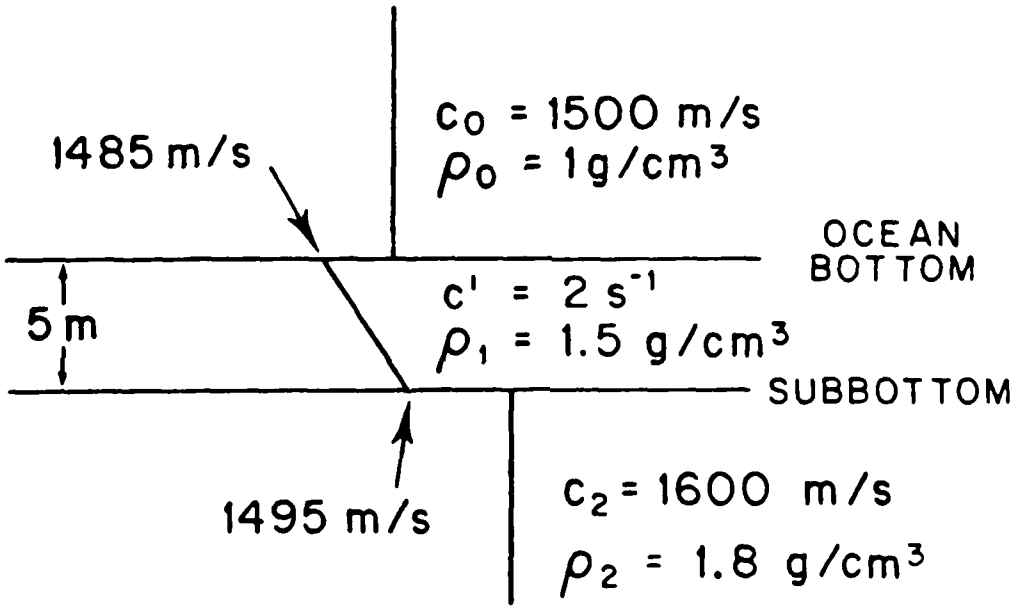

Fig. 3.4 A thin layer-model with a 5-m layer.

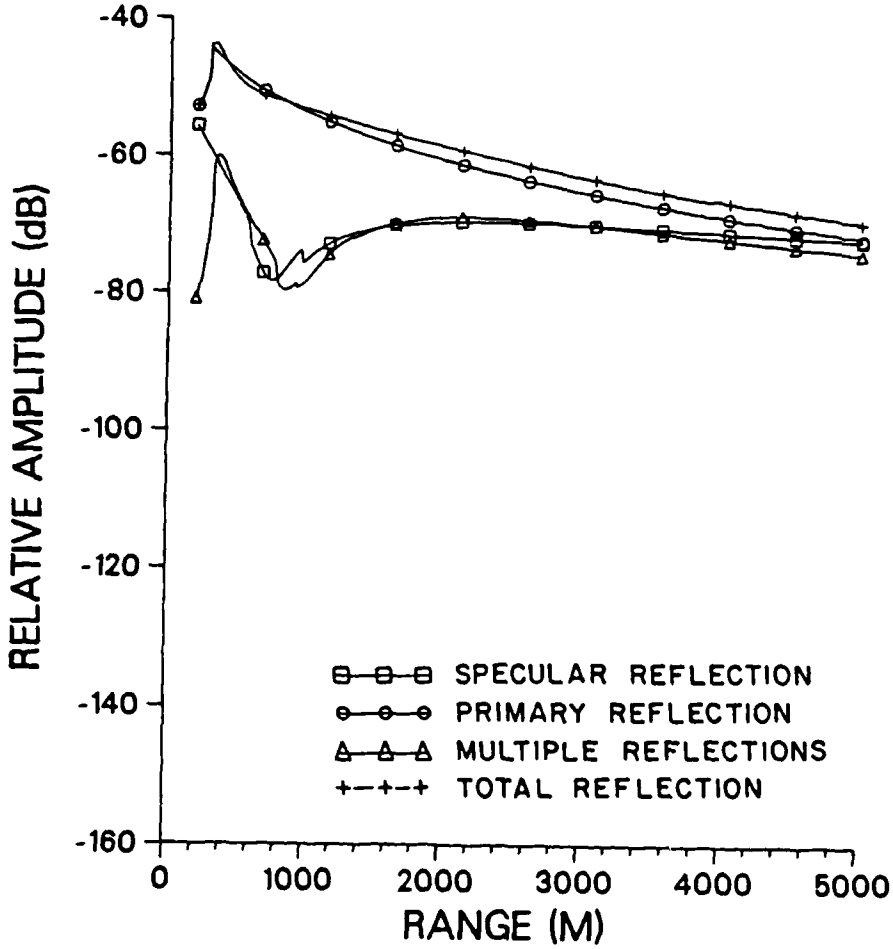

Fig. 3.5 The reflected fields for the Model I at $z + z_0 = 100$ m.

Performing this analysis, we see that the primary reflection dominates the total reflected field up to a horizontal range of 5000 m. Fig. 3.6 shows a ray diagram of the primary reflections. There is no caustic generated because of the thin layer. The specular and multiple reflections are of about equal level, though both are substantially smaller than the primary reflection for most ranges. As the incident angle approaches grazing, the field amplitudes of all of the reflection types become almost equal. Since the differences in ray path between the different arrivals are very small for the chosen source-receiver geometry, i.e. the water column is twenty times thicker than the bottom layer, their corresponding saddle points are very close to each other at any given range. This is confirmed by observing that the specular and multiple returns exhibit minima which appear at the same incident angle in their reflection coefficient plots (similar plots are shown in Figs. 2.5 and 2.6), at closely located ranges near 800 m. A ray diagram of the primary reflections is shown in Fig. 3.6.

We conclude from the above observations that the effect of the thin layer, even with a rather strong sound velocity gradient (such as 2 s^{-1} in our example), is weak and that the reflected field is dominated by the subbottom with which the primary reflection has the strongest interaction except at ranges associated with incidence very close to grazing.

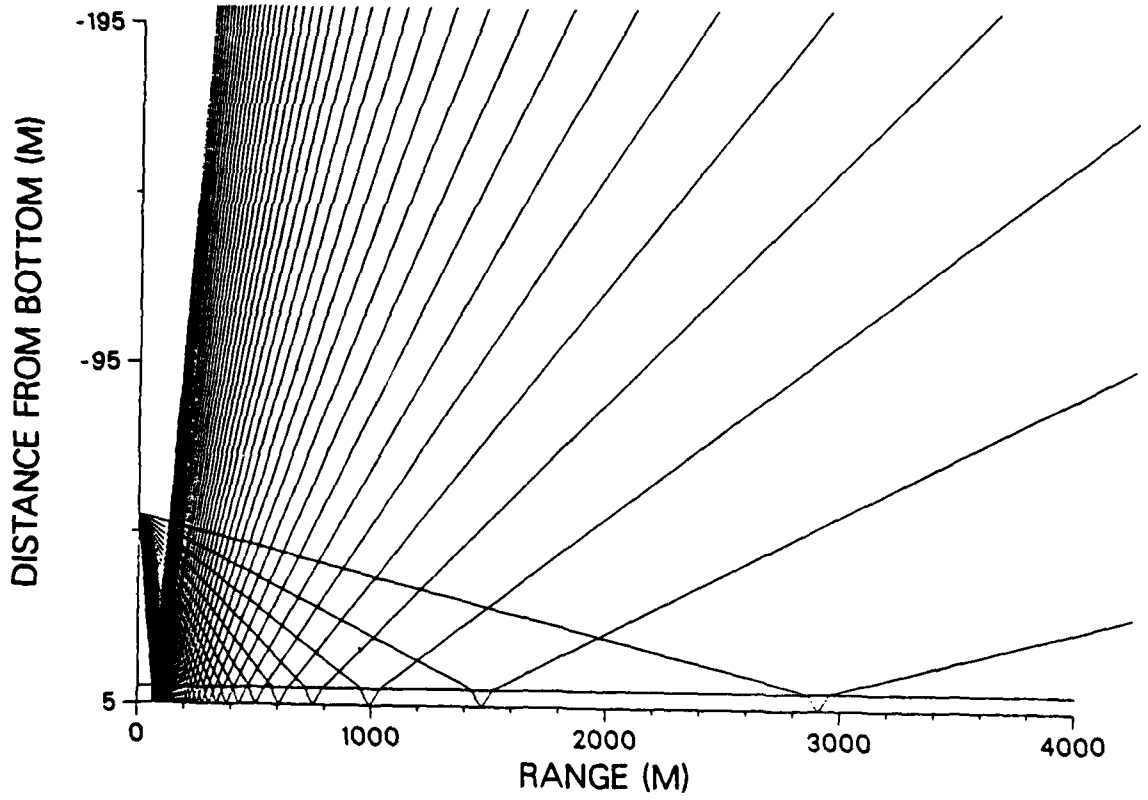

Fig. 3.6 A ray diagram of the primary reflections for the Model I.

3.3.2 Model II: Small layer thickness with variable source--receiver heights

The Models IIa and IIb, corresponding to two different sound velocity gradients, 0.5 s^{-1} and 1.5 s^{-1}, respectively(cf. Fig. 3.7), are considered for two different values of source-receiver height. The reflected fields at Z = 50 m and Z = 100 m for the first model are shown in Fig. 3.8, while the fields for the second model for these values of Z are also shown in Fig. 3.9.

For both models highly oscillatory amplitude variation is seen at close ranges (r < 500m). This is due to the strong interaction between the specular and primary reflections. As the specular reflection approaches its minimum amplitude, the effect of the multiples becomes more pronounced and alters the curve of the total reflected field which is now dominated by the primary reflection.

Beyond a range of about 2000 m, the primary reflection decays with range because the amplitude of the reflection coefficient for the primary reflection starts decaying as it approaches grazing incidence(cf. Fig. 3.10b) as well as the geometric spreading increases. The specular reflection maintains a steady level due to a sharp increase in the reflection coefficient amplitude (cf. Fig. 3.10a) countering the loss due to geometric spreading. In both models the primary reflection dominates for most ranges at Z = 100 m.

However, at Z = 50 m in both models, the specular reflections become dominant over the primary reflection at mid-ranges (2500-3500 m). This is due to the fact that when Z is reduced to 50 m, the water--path contribution to the geometric spreading becomes less, and thus the

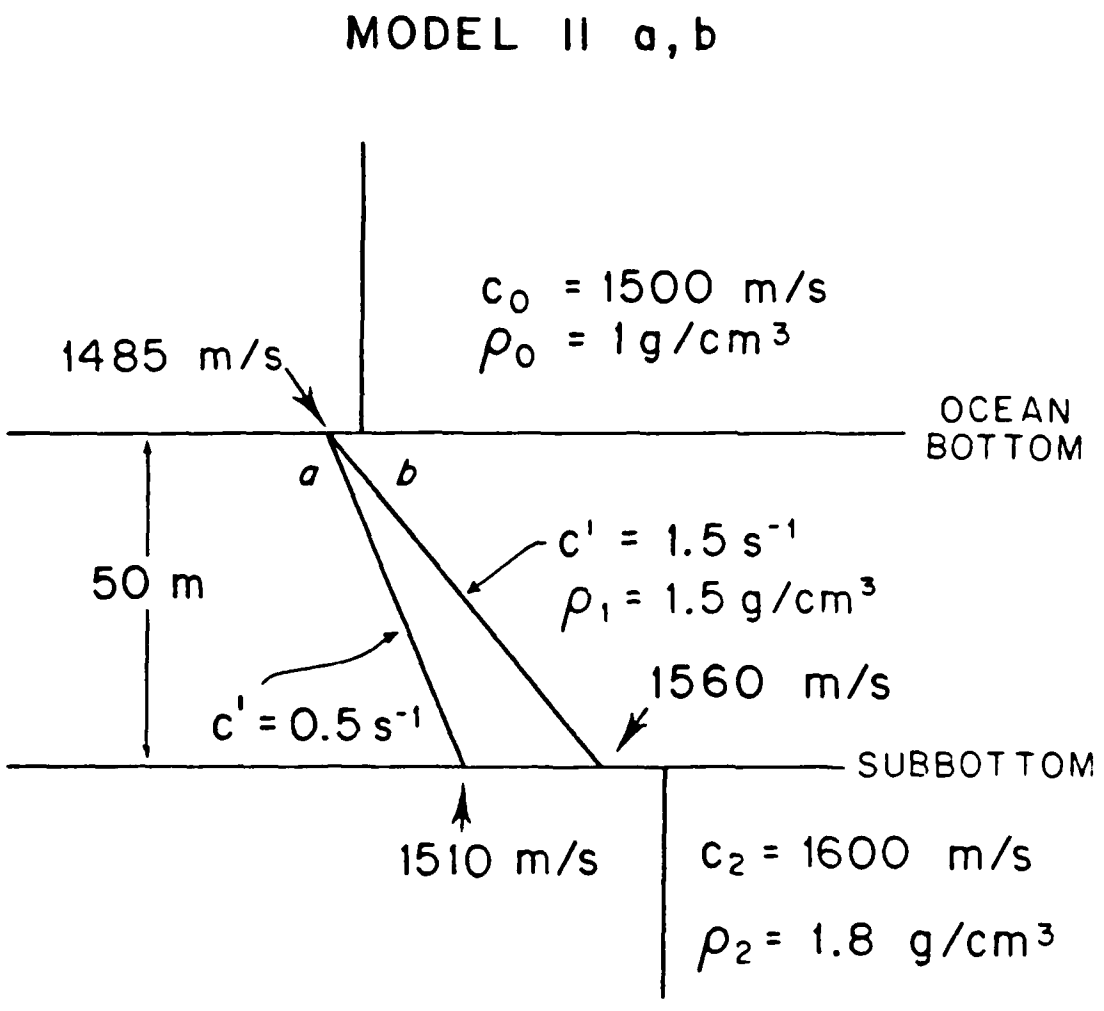

Fig. 3.7 A small layer models with a 50-m layer, and (a) g = 0.5 s^{-1}, (b) g = 1.5 s^{-1}.

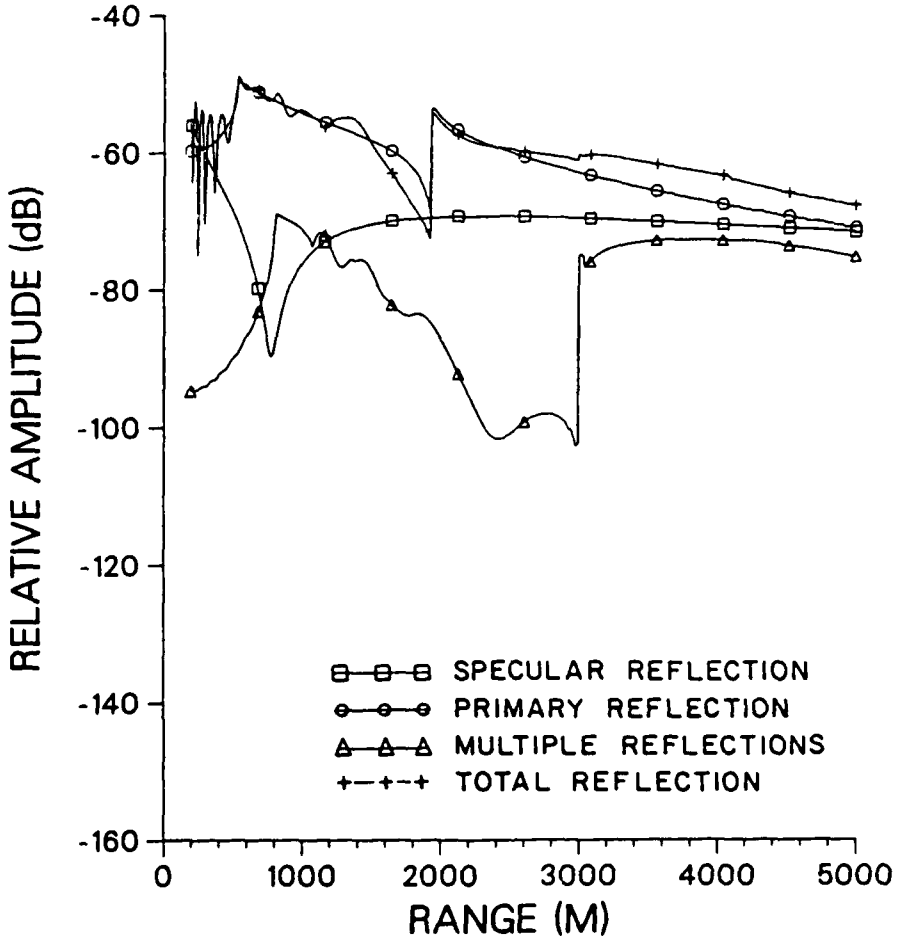

Fig. 3.8a The reflected fields for the Model IIa at $z + z_0 = 100$ m.

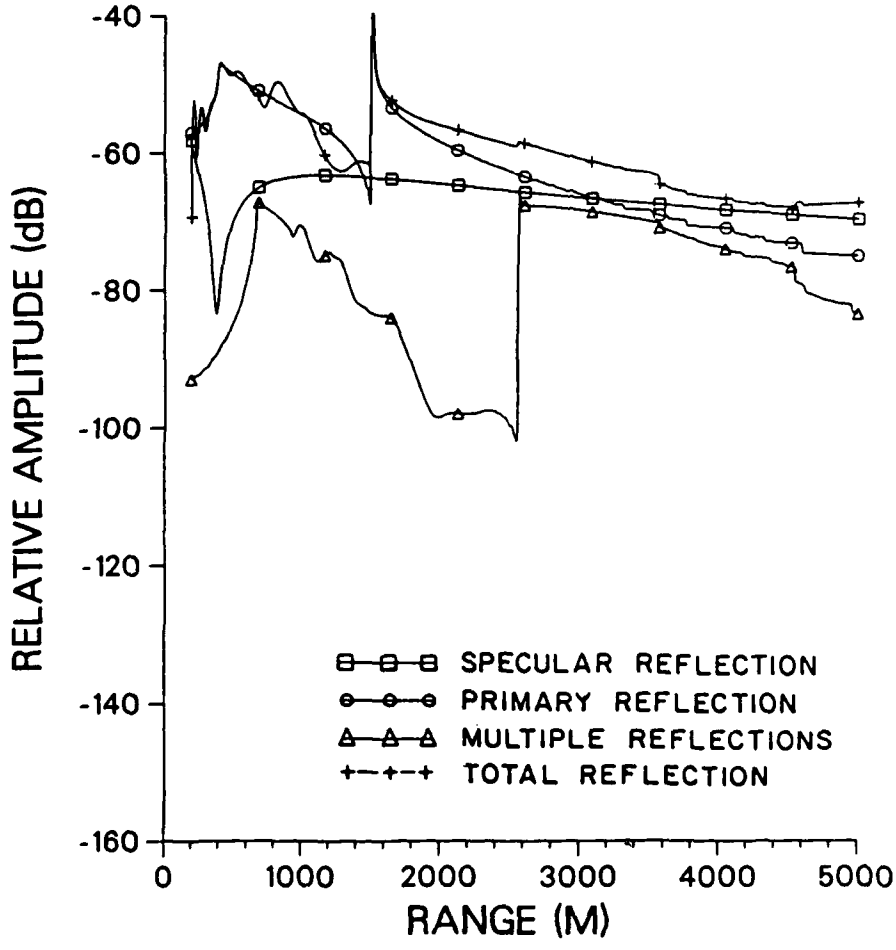

Fig. 3.8b The reflected fields for the Model IIa at $z + z_0 = 50$ m.

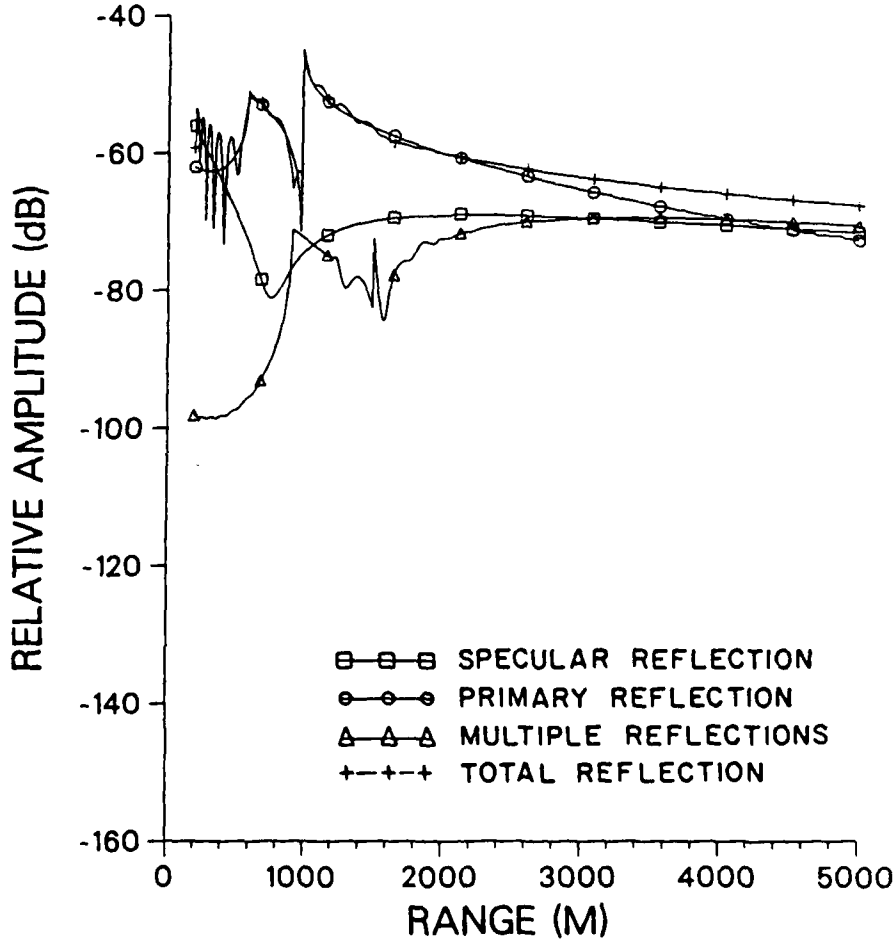

Fig. 3.9a The reflected fields for the Model IIb at $z + z_0 = 100m$.

AD-A144 449 ASYMPTOTIC ANALYSIS OF OCEAN BOTTOM REFLECTED ACOUSTIC 2/2
FIELDS(U) WOODS HOLE OCEANOGRAPHIC INSTITUTION MA
H KAWAHARA MAY 84 WHOI-84-23 N00014-82-C-0152

UNCLASSIFIED F/G 20/1 NL

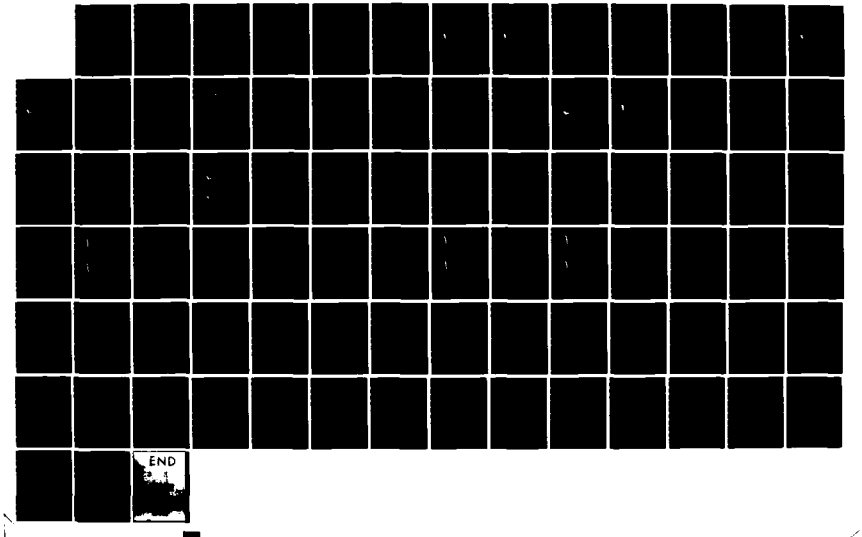

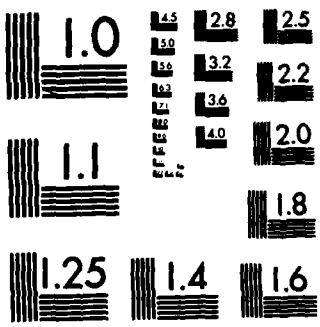

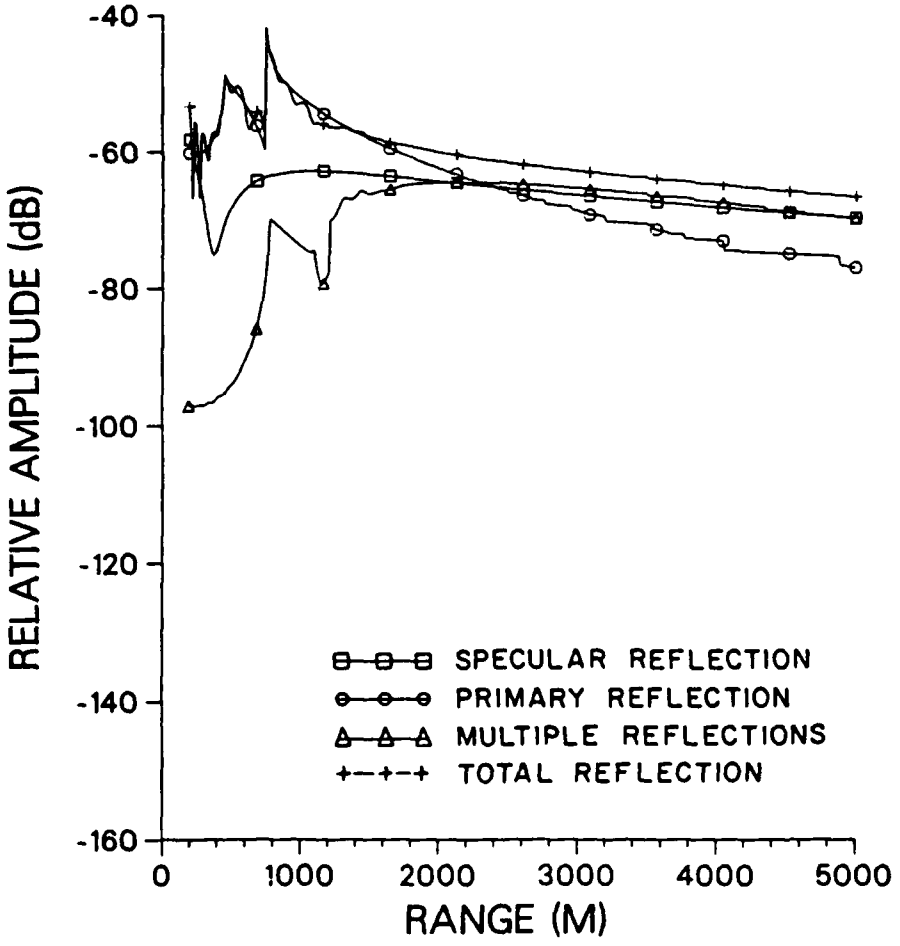

Fig. 3.9b The reflected fields for the Model IIb at $z + z_0 = 50$ m.

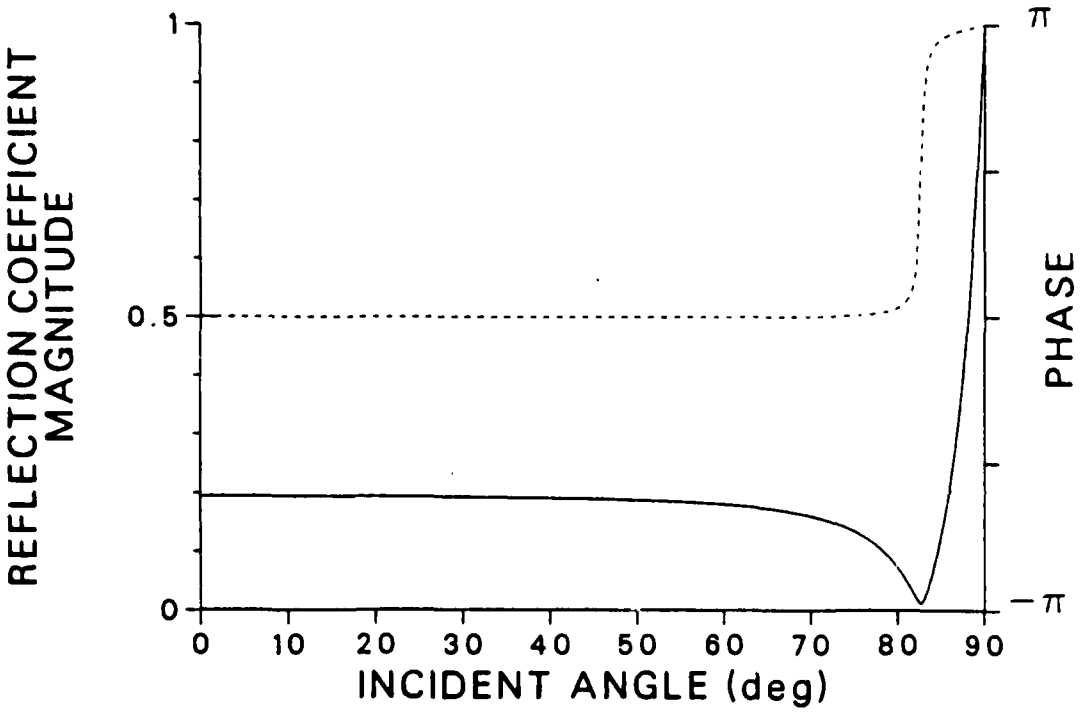

Fig. 3.10a The specular reflection coefficient for the Model IIa.

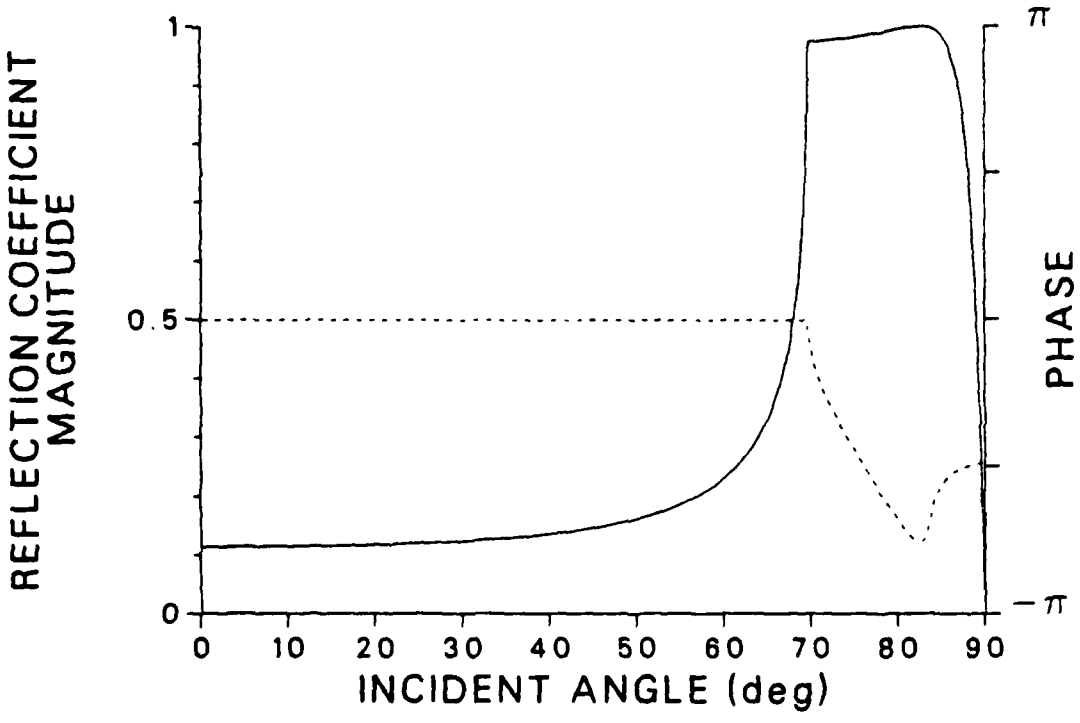

Fig. 3.10b The primary reflection coefficient for the Model IIa.

contribution of the layer-path to the total geometric spreading is more emphasized.

The sharp peak in the primary reflection seen at range 1500 m in Fig. 3.8b (Model IIa) indicates caustic formation near the ocean bottom. However, as Z increases to 100 m, it disappears. This disappearance of the caustic is due to the presence of the subbottom and there exists a caustic cut-off between these depths. Section 4.2 will treat this problem in more detail.

Due to the small velocity gradient in Model IIa the field contribution from the multiples is small even at long ranges ($r > 3000$ m). However, when the velocity gradient is increased to 1.5 s^{-1}, as shown in Model IIb, their contribution becomes one of the major ones even at relatively close ranges for small Z (cf. Fig. 3.9b). Therefore, a large sound velocity gradient at the bottom and a small Z contribute to a larger multiple field amplitude.

3.3.3 Model III: Thick Layer with Small Gradient

Two different profile shapes are consider in this model: $1/c^2$ and c^3-linear(cf. Fig. 3.11). As discussed in Sec. 3.2.2 and shown in Fig. 3.2, a small reference gradient(.5 s^{-1} in this model) creates only small differences in the profile shapes. However, even a small difference in profile shape can make large differences in the geometric spreading at long ranges. The large layer thickness makes it possible to form a caustic extending into the water column(cf. Fig. 3.12). In this case the total reflected fields are characterized by the fields beyond the caustics formed by the primary and multiples(cf. Fig. 3.13),

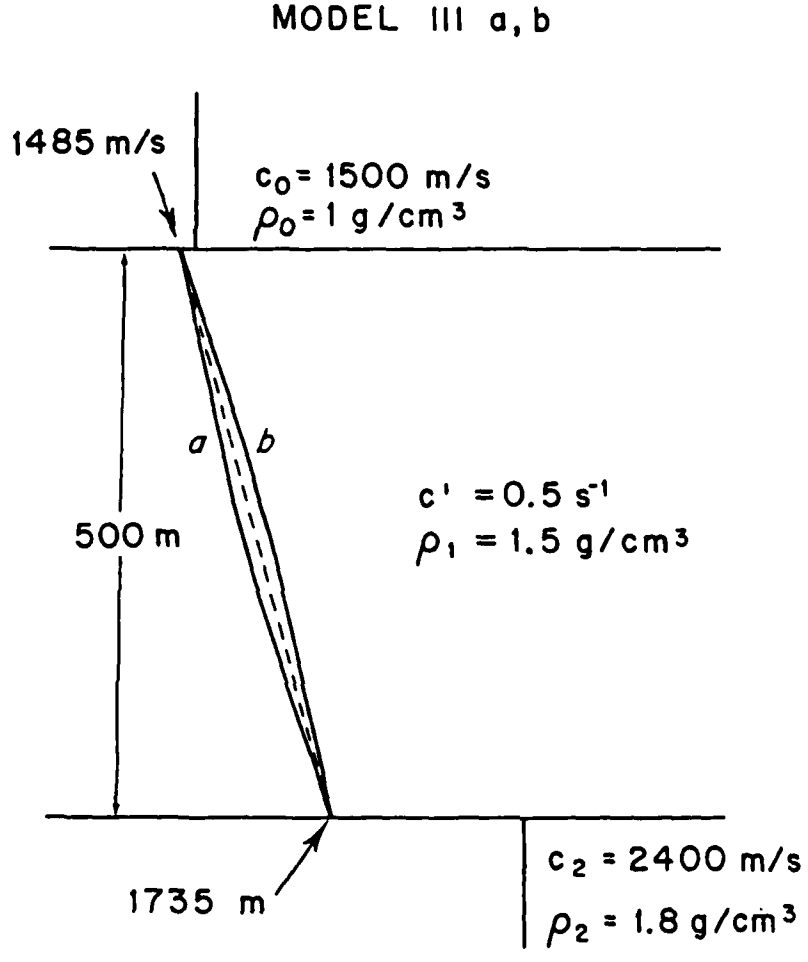

Fig. 3.11 A thick layer model with a 500-m layer where g = 0.5 s^{-1}. (a) The $1/c^2$-linear and (b) the c^3-linear profiles.

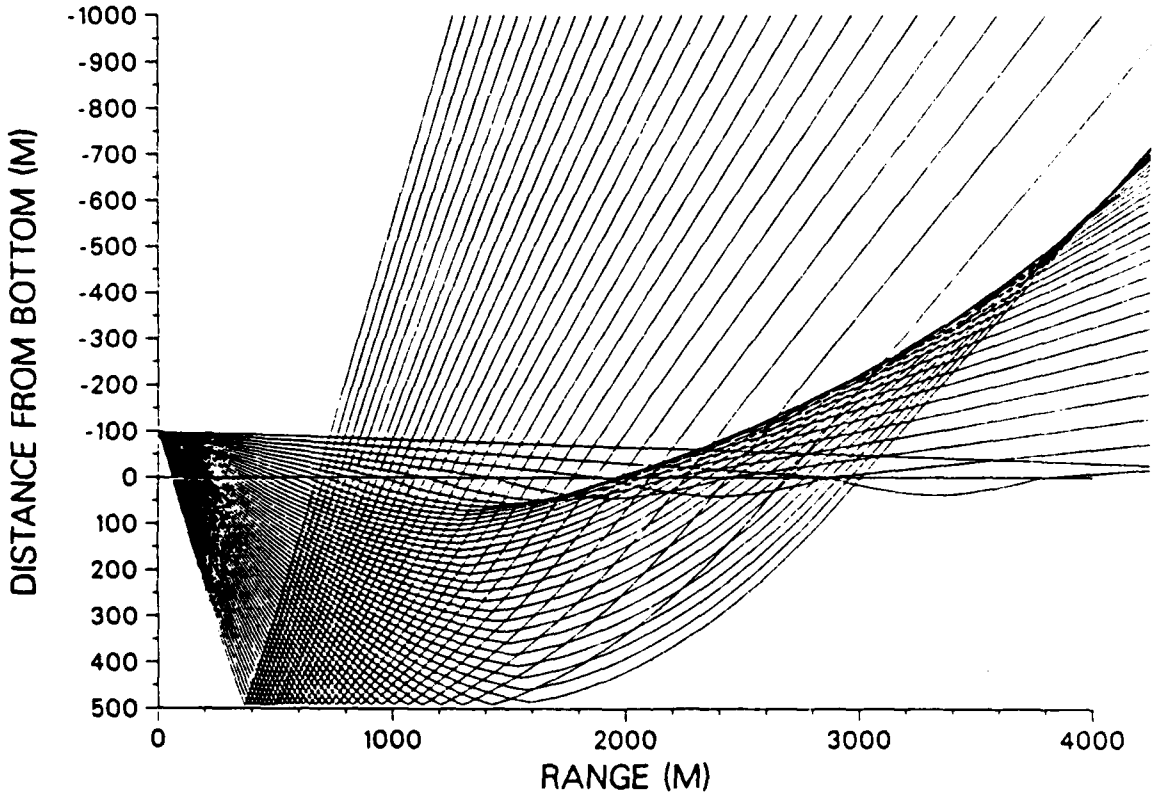

Fig. 3.12a A ray diagram of the primary reflections for the Model IIIa.

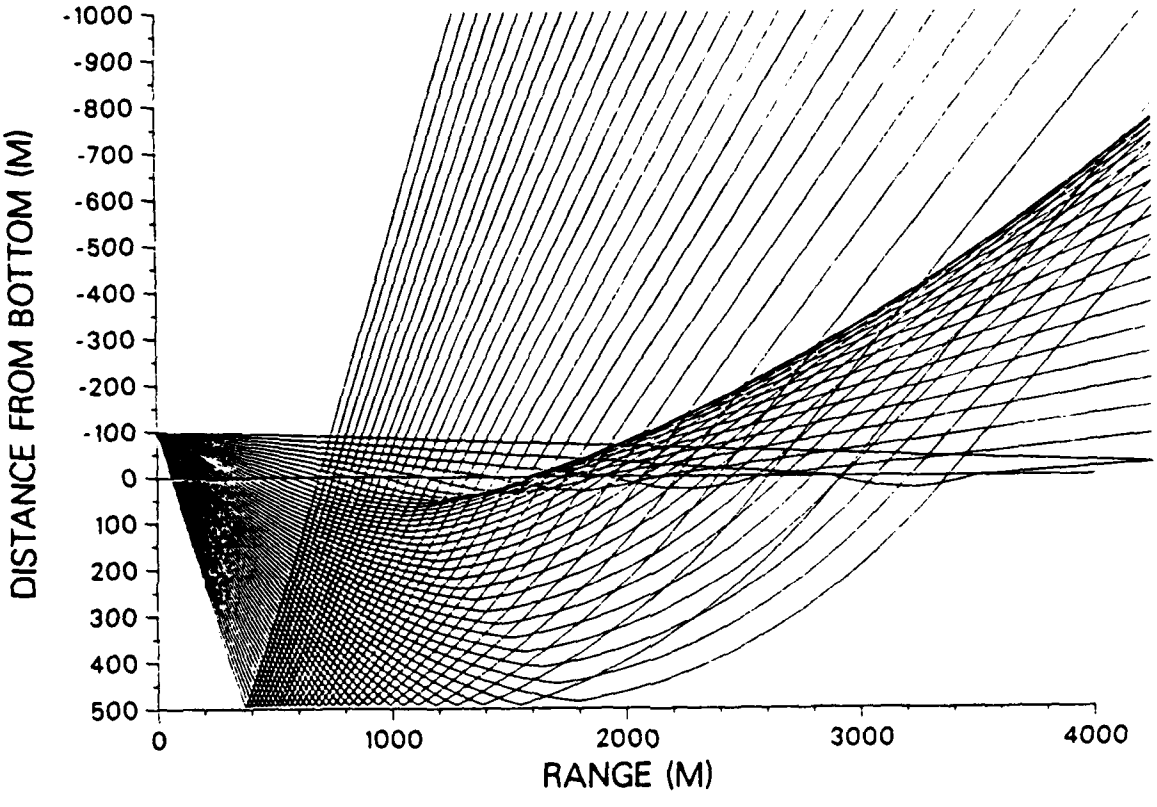

Fig. 3.12b A ray diagram of the primary reflections for the Model IIIb.

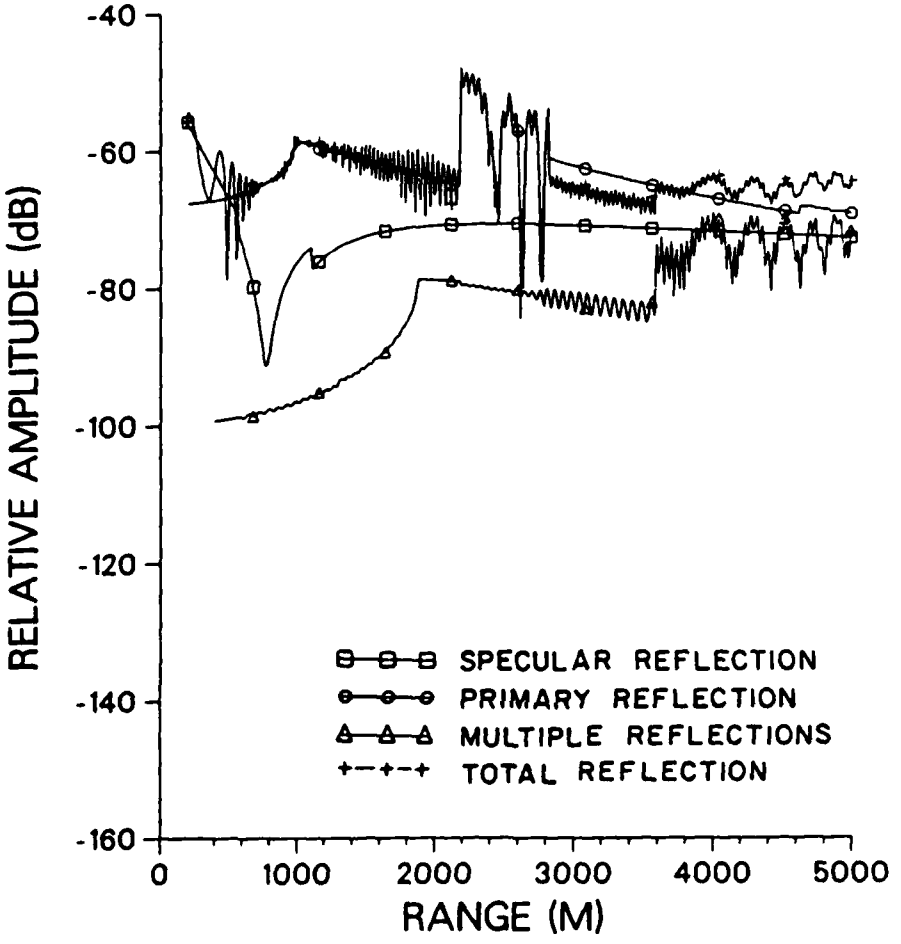

Fig. 3.13a The reflected fields for the Model IIIa at $z + z_0 =$ 100 m.

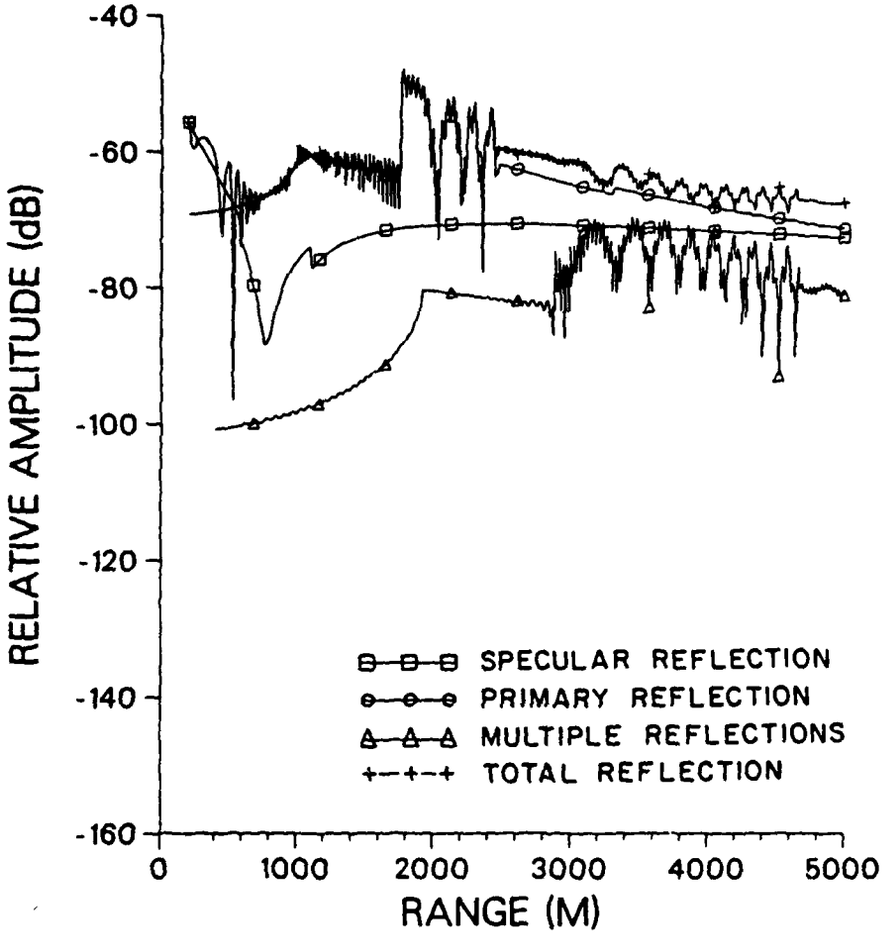

Fig. 3.13b The reflected fields for the Model IIIb at $z + z_0 = 100$ m.

while the overall field amplitudes of all reflection types are very similar otherwise.

These strongly interfering primary and multiple reflection amplitudes, which result from caustic formations, are due to multi-saddle point contributions(cf. Sec. 2.3.2). The difference in locations of the appearance of these features are very clear in both profile types. However, the patterns of the amplitudes of both primary and multiples are almost identical in both profile types. The similarity in the field amplitudes near the caustic will be discussed in Sec. 4.3.

3.3.4 Model IV: Thick Layer with Large Gradient

The sound velocity gradient at the top of the layer varies strongly in this model, given that the boundary conditions at both of the interfaces are the same(cf. Fig. 3.14). As shown in Figs. 3.15 and 3.16, the caustic formations of the primary reflections are quite different in the $1/c^2$ and c^3-linear layer cases. In each case the interference patterns due to multi-saddle points characterize the behaviors of the primary and multiple reflections(cf. Fig. 3.17). In the $1/c^2$-linear case shown in Fig. 3.15 the caustic has two branches and a cusp at the point where they meet. The interference of the primary reflections only takes place within the ranges surrounded by the caustic branches. In the case of the c^3-linear profile, there is only one caustic branch which extends into the water column up to the caustic cut-off point (cf. Sec. 4.2). For large layer thickness, the caustic branch can extend to large distances above the ocean bottom. Thus the interference of the primary reflections can extend to longer horizontal

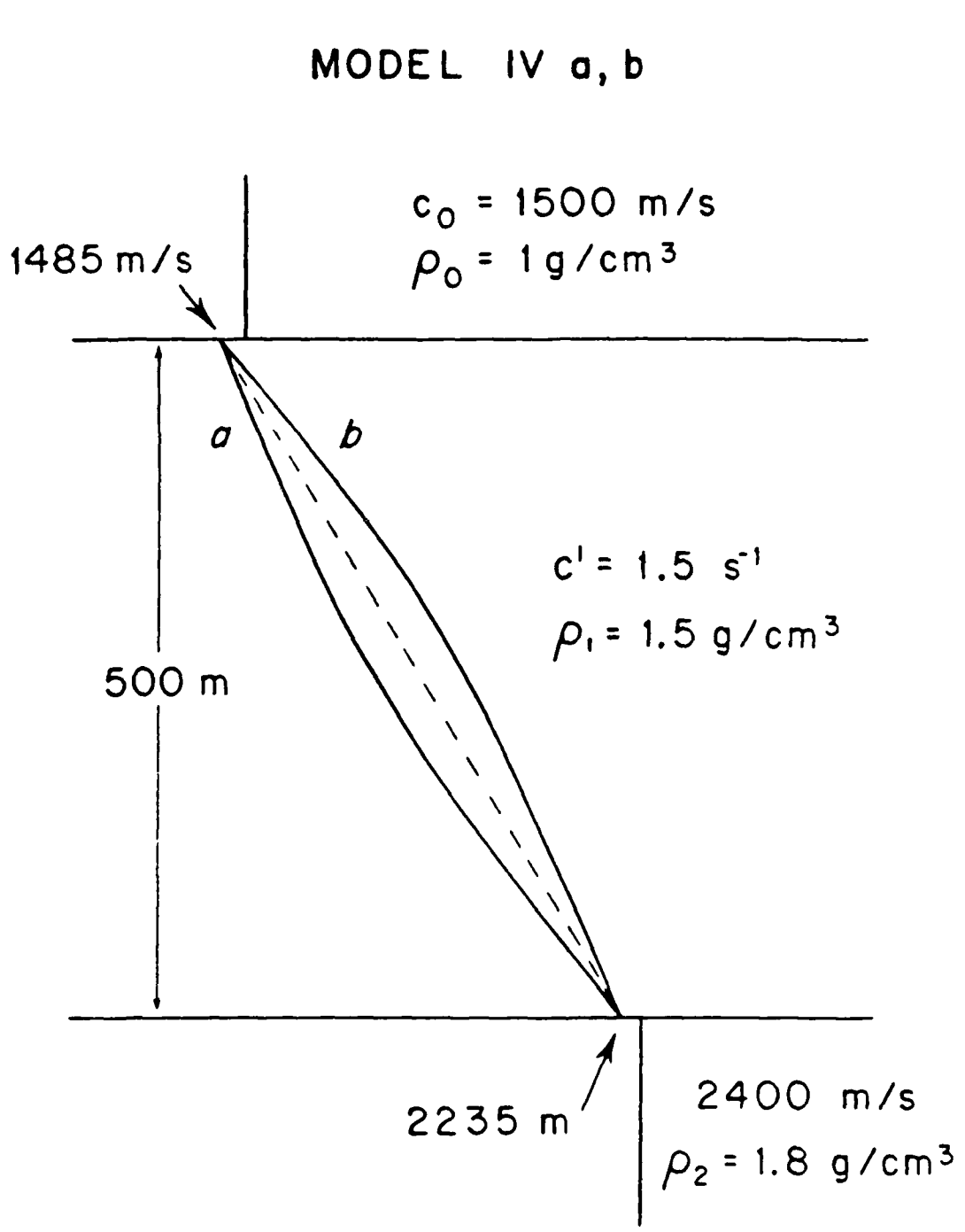

Fig. 3.14 A thick layer model with a 500-m layer where $g = 1.5\ s^{-1}$. (a) The $1/c^2$-linear profile and (b) the c^3-linear profile.

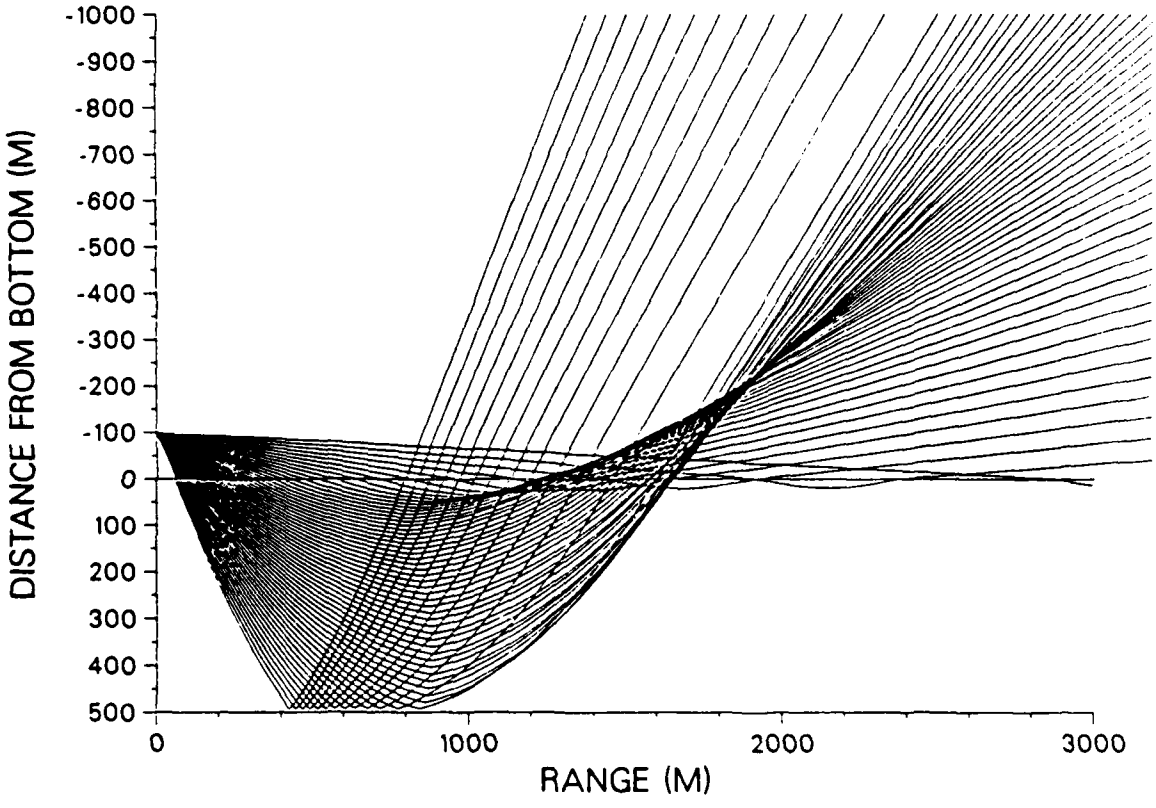

Fig. 3.15 A ray diagram of the primary reflections for the Model IVa.

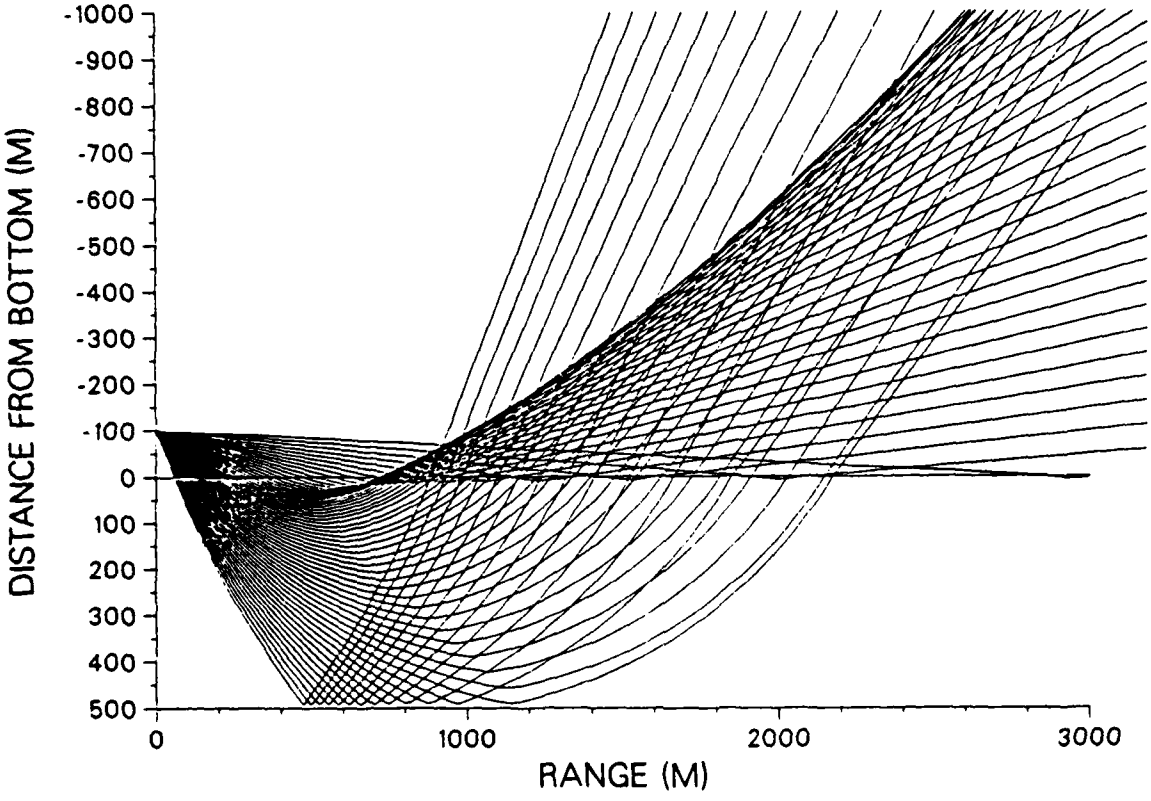

Fig. 3.16 A ray diagram of the primary reflections for the Model IVb.

ranges until the subbottom reflection terminates this behavior(cf. Fig. 3.16).

Comparing the reflected fields generated from both cases with different sound velocity gradients, we observe that the total field from Model IVb(cf. Fig. 3.17b), which has a larger gradient at the bottom than Model IVa(cf. Fig. 3.17a), shows lower amplitude levels beyond the primary caustic range. One may expect from our discussion in Sec. 3.2.1 that the primary reflection for a geoacoustic model with a larger sound velocity gradient should have a larger amplitude. However, for our typical source-receiver geometries, i.e. $Z > 100$ m, the condition given by Eq. (3.24) is violated and the water-path contribution to the total geometric spreading becomes substantially larger than that of the layer as the eigenray approaches grazing incidence.

Since α_0[cf. Eq. (3.24)] of the primary eigenrays reaching long ranges in Model IVb are smaller, an even greater water-path contribution is added to the total geometric spreading. As a result, the primary reflection from Model IVb has less amplitude than that of Model IVa. Furthermore, since the primary reflections are the dominant contributor and control the overall level of the total reflected fields for both cases, the total reflected field from Model IVb shows less relative amplitude even with the greater velocity gradient near the bottom.

Multiples, on the other hand, effectively reduce geometric spreading due to both the water-path and the layer-path, thus multiple contribution becomes larger from the geoacoustic model with a larger sound velocity gradient at the bottom. The multiple reflections also form similar interference patterns to the primary reflections and are respon-

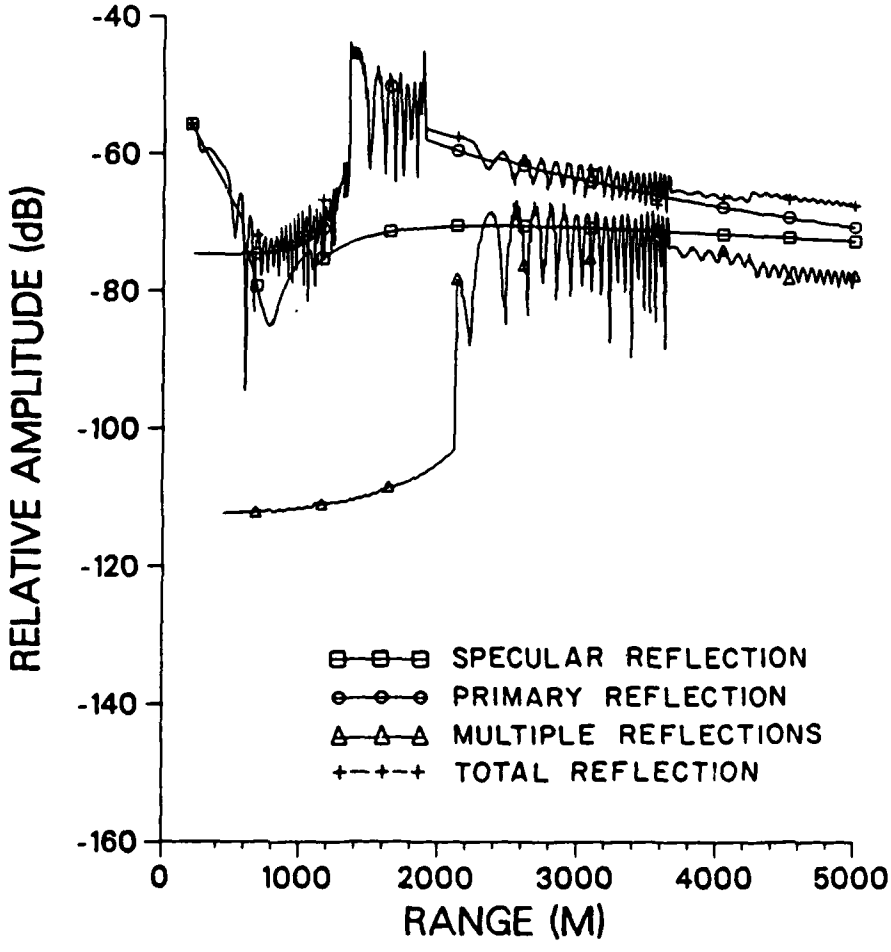

Fig. 3.17a The reflected fields for the Model IVa at $z + z_0 = 100$ m.

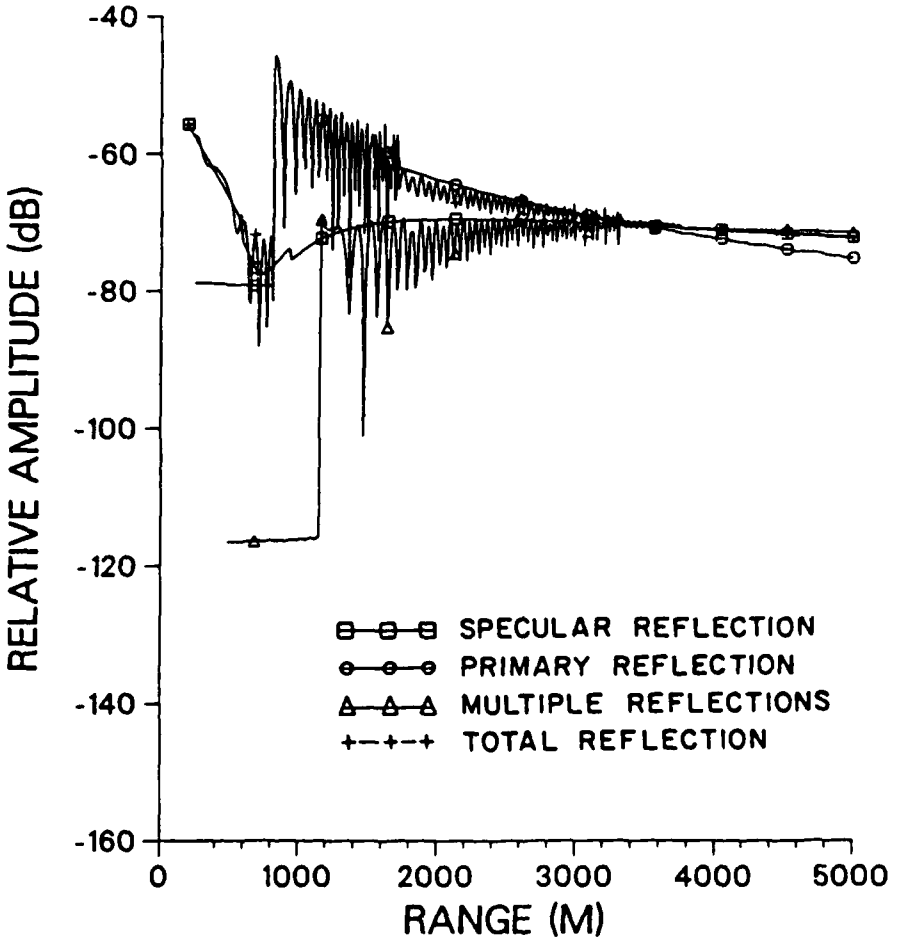

Fig. 3.17b The reflected fields for the Model IVb at $z + z_0 = 100$ m.

sible for the highly oscillatory patterns in the total reflected fields observed at long ranges beyond the primary caustic ranges for both models.

References:

[1] Frisk, G. V., Doutt, J. A. and Hays, E. E.,"Bottom interaction of low-frequency acoustic signals at small grazing angles in the ocean bottom," J. Acoust. Soc. Am., 69, 84-94 (1981).

[2] Hamilton, E. L., "Geoacoustic modeling of the sea floor," J. Acoust. Soc. Am., 68, 1313-1340 (1980).

[3] Kawahara, H. and Frisk, G. V., "A canonical ocean bottom sound velocity profiles," (Submitted to J. Acoust. Soc. Am.)

Chapter 4: Analytic Studies on Caustics

Due to the limitations of the method of steepest descents, the analytic evaluation of the reflected fields near caustics was excluded in Chapter 2. However, understanding the parametric dependence of the caustic shapes and the strength of the field near the caustics can help recover geoacoustic properties of the ocean bottom[2]. In this chapter we shall focus on this subject and discuss the caustic behavior, primarily in a qualitative manner, for the proposed sound velocity profile shapes.

4.1 The caustic equations for the proposed geoacoustic models

Brekhovskikh[1]* derived the equations of caustics formed in a homogeneous upper half-space overlying an inhomogeneous halfspace for the n^2-linear and c-linear profiles where the sound velocity is continuous across the boundary. This section is an extension of his work to derive a caustic equation for the case of the c^3-linear profile which provides a more realistic profile shape. The equations of caustics for all three cases are derived for the n-th multiples and therefore they are more general forms than those of Brekhovskikh. In this section we shall neglect the effect of the subbottom on caustic formation

---

* The results given in Ref. 1, Eqs. (46,21) through (46.23) appear to have errors. Our corrected formulas are given in Sec. 4.1.2 of this chapter.

and will reserve a discussion of that subject for Sec. 4.2.

The cases treated in this chapter are limited to the geoacoustic models where there is no discontinuity in sound velocity at the ocean bottom interface. Even though we have chosen less comprehensive geoacoustic models than those we have used earlier in order to make the algebra easier, we may still learn a great deal about the caustics from these special cases for the various inhomogeneities in the layer.

4.1.1 The caustic equations for the c^3-linear profile

The conditions for the caustic in the water column are given by Eqs. (2.40) and (2.44) when p_s is such that the left hand side of Eq. (2.44) vanishes. After Eqs. (3.15) and (3.16) are evaluated at the water-bottom interface and substituted in Eqs. (2.40) and (2.44) respectively, we obtain

$$-\frac{p_c}{\gamma_0}(z + z_0) + r_c + \frac{2n}{a_3 p_c}(1 - p_c^2 b_3^{2/3})^{1/2}(2p_c^{-2} + b_3^{2/3}) = 0 \qquad (4.1)$$

$$-\frac{z + z_0}{c_0^3 \gamma_0^3} - \frac{6n}{a_3 p_c^4}(2 - p_c^2 b_3^{2/3})(1 - p_c^2 b_3^{2/3})^{-1/2} = 0 \qquad (4.2)$$

where p_c is the horizontal slowness which satisfies the above equations, a_3 and b_3 are the coefficients in Eq. (3.13), and r_c is the caustic range. If the sound velocity in the lower half-space is given by

$$c^3(z) = a_3 z + c_0^3 \qquad (4.3)$$

where c_0 is the sound velocity in the upper half-space, Eqs. (4.1) and (4.2) may be reduced to

$$r_c = \frac{p_c}{\gamma_0}(z + z_0) - \frac{2n}{a_3 p_c}(1 - p_c^2 c_0^2)^{1/2}(2p_c^{-2} + c_0^2) \qquad (4.4)$$

$$\frac{z + z_0}{c_0^2 \gamma_0^3} + \frac{6n}{a_3 p_c^4}(2 - p_c^2 c_0^2)(1 - p_c^2 c_0^2)^{-1/2} = 0 \qquad (4.5)$$

Rewriting γ_0 and p_c in terms of the grazing angle α in the medium containing the incident wave, we then obtain

$$r_c = (z + z_0)\cot\alpha - \frac{2c_0^3 n}{a_3}\tan\alpha\left(\frac{2}{\cos^2\alpha} + 1\right) \qquad (4.6)$$

$$z + z_0 = -\frac{6nc_0^3}{a_3}\frac{\sin^2\alpha}{\cos^4\alpha}(2 - \cos^2\alpha) \qquad (4.7)$$

Solving for $\cos^2\alpha$ from Eq. (4.7), we obtain

$$\cos^2\alpha = \frac{3nc_0^3}{a_3(z + z_0) + 6nc_0^3}\left[3 \pm \left(1 - \frac{4a_3}{3nc_0^3}(z + z_0)\right)^{1/2}\right] \qquad (4.8)$$

Since $a_3 < 0$, there is no limit on $z + z_0$ and the caustic branch extends to infinity in the upper halfspace. Since $\cos^2\alpha \leq 1$, we must choose the minus sign for the square root for any $a_3(z + z_0)$.

Therefore, the location of the caustic may be obtained for a given z and z_0 by substituting

$$\alpha = \text{Arccos}\left\{\frac{3nc_0^3}{a_3(z + z_0) + 6nc_0^3}\left[3 - \left(1 - \frac{4a_3}{3nc_0^3}(z + z_0)\right)^{1/2}\right]^{1/2}\right\} \quad (4.9)$$

into Eq. (4.6) in order to obtain the caustic range r_c. Fig. 4.1a shows a plot of r_c vs. z for a source height of 50 m, c_0 = 1500 m/s, n = 1 (primary reflection) and $a_3 = -6.75 \times 10^6$ m^2/s^3.

4.1.2 The caustic equation for the $1/c^2$-linear profile

The caustic equation in the water column for the $1/c^2$-linear profile may be similarly derived and it is expressed by the following equations:

$$\alpha = \text{Arcsin}\left\{\frac{1}{2}\left[1 \pm \left(1 - \frac{2a_2(z + z_0)c_0^2}{n}\right)^{1/2}\right]^{1/2}\right\} \quad (4.10a)$$

$$r_c = \frac{4n}{a_1 c_0^2}\sin^2\alpha \cos^2\alpha \quad (4.10b)$$

where α is the grazing angle of the ray in the water column and a_1 is the coefficient of z in Eq. (3.1). For a given z and z_0, one may obtain α from Eq. (4.10a), and substitute it in Eq. (4.10b) to obtain the caustic range r_c. Since α has two values for a given z, z_0 and a_1, then r_c does also. This is a very important characteristic of the caustic shape generated by the $1/c^2$-linear profile whose caustic branches never extend to positive infinity in the upper halfspace. Instead they form a cusped caustic known as a butterfly caustic(cf. Figs. 4.2a,b).

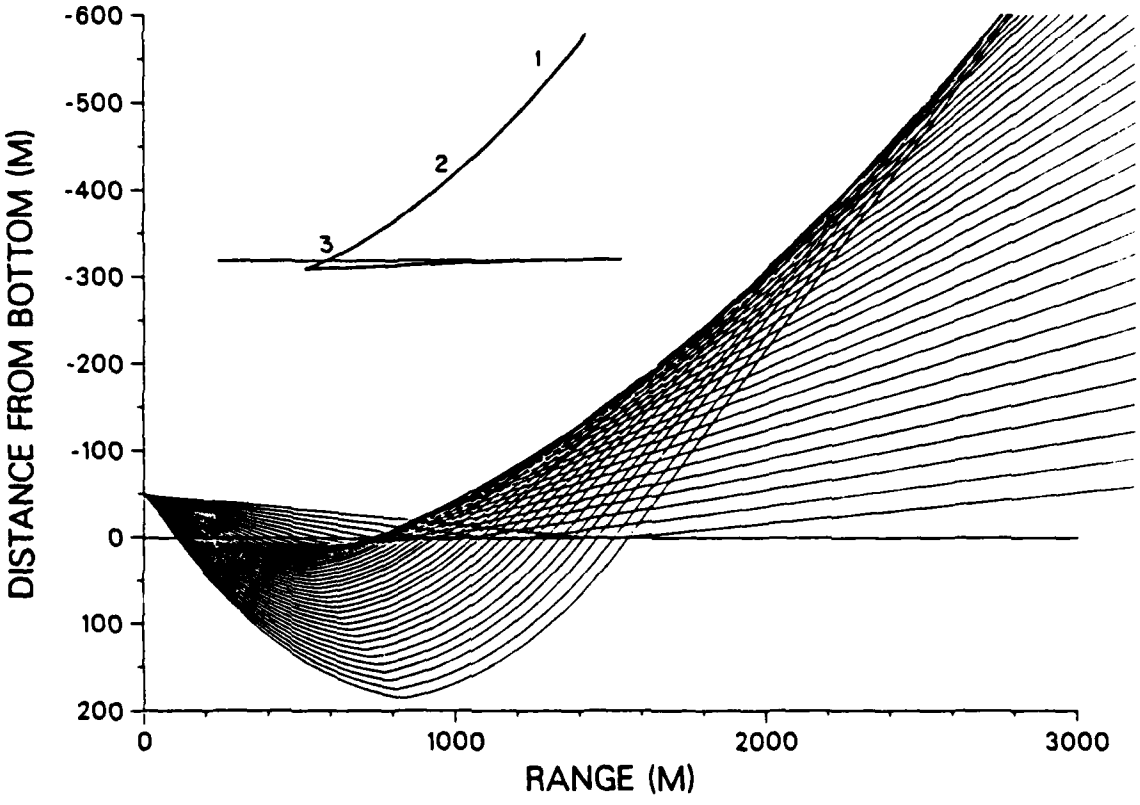

Fig. 4.1a,b A ray diagram of the primary reflections for the c^3--linear profile and the associated caustic curve.

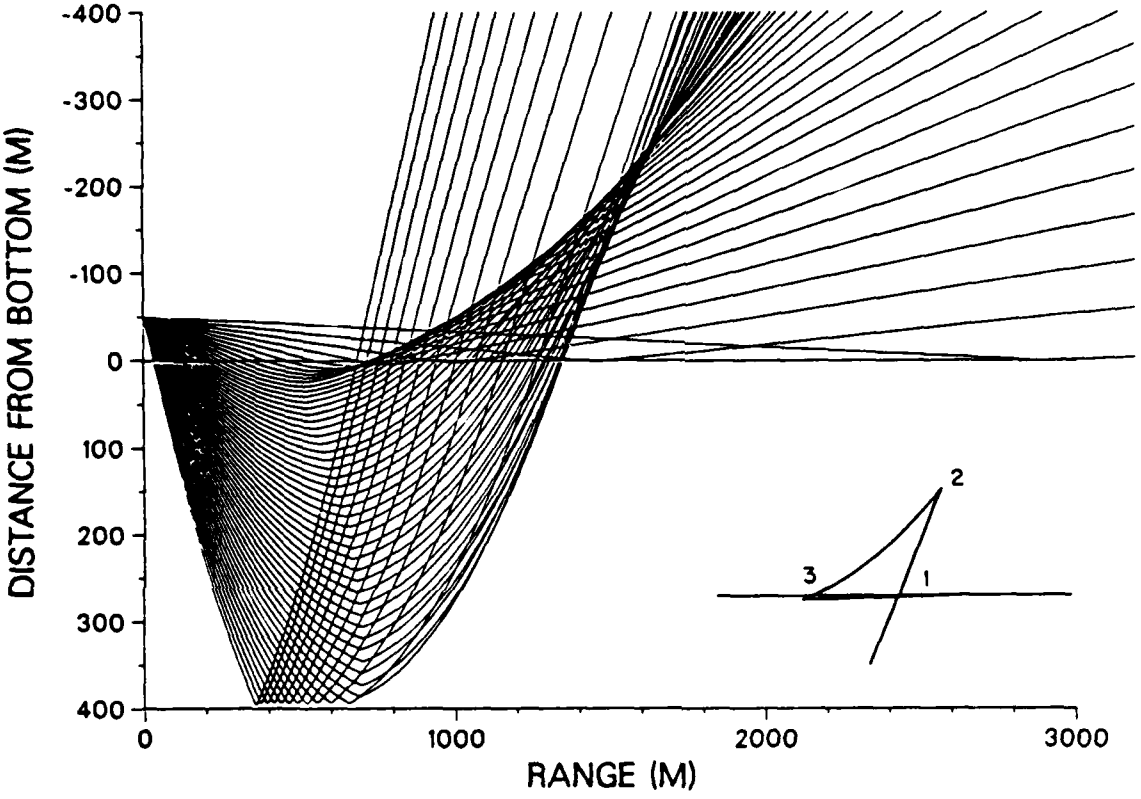

Fig. 4.2a,b A ray diagram of the primary reflections for the $1/c^2$-linear profile and the associated caustic curve.

At the cusp α has a single value satisfying the condition,

$$2a_1(z + z_0)\, c_0^2/n = 1 \tag{4.11a}$$

Thus, we obtain from Eq. (4.10)

$$\alpha = \pi/6, \qquad r_c = \frac{3^{3/2} n}{2a_i c_0^2} \tag{4.11b}$$

Equation (4.11) indicates that the grazing angle for the cusp is independent of $z + z_0$ and a_1, and is <u>always</u> 30 degrees. The regions of α which correcpond to separate branches of the caustic in the water column are given as

on the branch 2-3: $\alpha_1 < \alpha < \pi/6$

on the branch 1-2: $\pi/6 < \alpha < \alpha_2$

where $$\alpha_{1,2} = \text{Arcsin}\ \tfrac{1}{2}[1 \mp (1 - 2a_1 z_0 c_0^2/n)^{1/2}] \tag{4.12}$$

4.1.3 The caustic equation for the c-linear profile

The derivation of the caustic equation for the c-linear profile is straightforward and the result is given by

$$z + z_0 = -\frac{a_2}{8nc_0} r_c^2 \tag{4.13}$$

where a_2 is the coefficient of z in Eq. (3.7).

4.1.4 Caustic equations for small grazing angles

Fig. 4.3 shows the curves of the caustics in the water column for the three different profile shapes given that all of their sound velocity gradients at the ocean bottom interface are fixed at 1 sec^{-1} (cf. Fig. 4.4). Notice that all of them have very similar curves (considering the upper branch of the $1/c^2$-linear profile) especially near the ocean bottom. This is due to the fact that all of the caustic equations become identical as the grazing angles become very small. If small angle approximations are substituted in the pairs of caustic equations, Eqs. (4.6) and (4.7), and Eqs. (4.10a,b), they can be reduced to (Eq. (4.13) is exact):

for the $1/c^2$-linear profile: $$z + z_0 \cong \frac{a_1 c_0^2}{16n} r_c^2 \quad \text{(upper branch)} \tag{4.14}$$

for the c^3-linear profile: $$z + z \cong - \frac{a_3}{24nc_0^3} r_c^2 \tag{4.15}$$

where α is approximated by

$$\alpha \cong [\frac{(z + z_0)c'}{2nc_0}]^{1/2} \tag{4.16}$$

with $$c' = \frac{dc_i(0)}{dz}; \qquad i = 1, 3$$

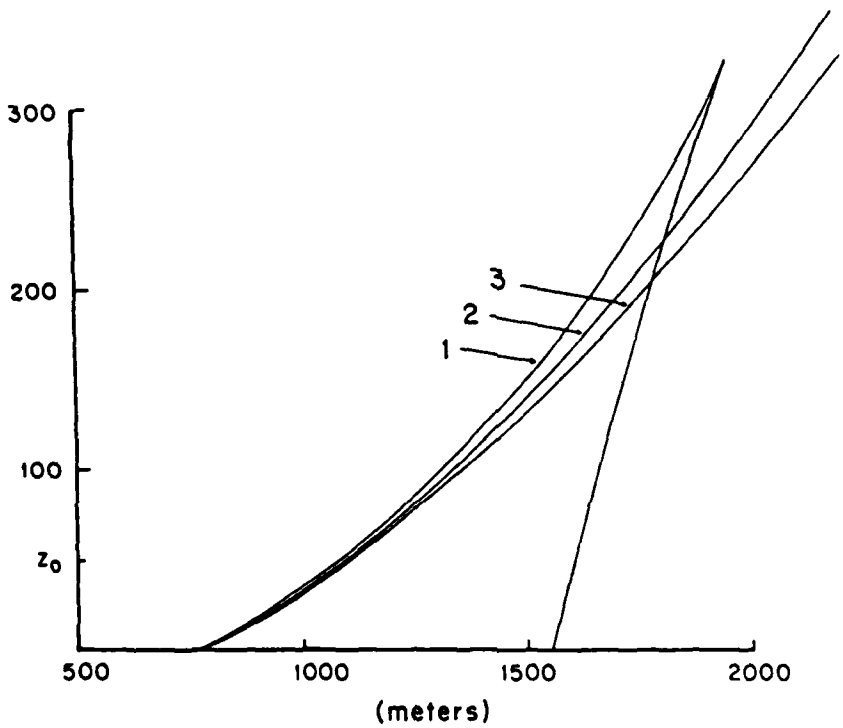

Fig. 4.3 Caustic curves of the (1) $1/c^2$, (2) c and (3) c^3-linear profiles for the same sound velocity gradient $g = 1\ s^{-1}$ at the bottom.

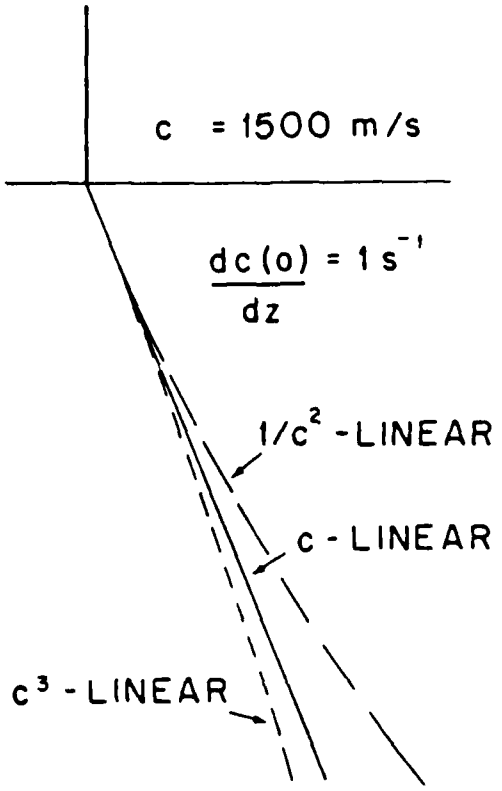

Fig. 4.4 The sound velocity profiles of the $1/c^2$, c and c^3-linear with depth for the same velocity gradient $g = 1\ s^{-1}$ at the bottom.

For the same gradient at the ocean bottom ($z = 0$), a_1 and a_3 may be given in terms of a_2 as

$$a_1 = 2a_2/c_0^3,$$

$$a_3 = -3a_2/c_0^2.$$

If a_1 and a_3 are substituted in Eqs. (4.14) and (4.15) respectively, they may be identically reduced to Eq. (4.13) for small grazing angles associated with caustics formed near the ocean bottom. Since small α corresponds to small $c'z_0$ [cf. Eq. (4.16)], we can conclude that the caustic curves near the ocean bottom(z is also small) are controlled by the gradient of the profile near the bottom, not the overall shape of the profile. This observation is particularly important when the subbottom in present since the caustics in the water column are formed only near the bottom for this case, which is discussed in the next section.

4.2 The effects of the subbottom interface on the caustic in the water column

In Section 4.1 the inhomogeneous medium was treated as an infinite halfspace for which caustics are formed by purely refracted rays. However, the presence of a subbottom reflector in the geoacoustic models under consideration serves to eliminate rays with certain ranges of horizontal slowness p from caustic formation. Brekhovskikh has delineated the regions of slowness for different branches of the caustics for the n^2-linear and c-linear cases. The presence of the subbottom simply

sets the limits on the regions of slowness forming the various caustic branches, but does not create additional branches.

For the case of the $1/c^2$-linear profile, the caustic branches will be eliminated in numerical order as labeled in Fig. 4.2a as the rays forming the caustic start reflecting off the subbottom interface. For the other two profile shapes, which share similar caustic curves with only two branches, the caustic branch extending into the water column away from the bottom will be eliminated. The order of disappearance of the caustic branch is again indicated by the numbers labeled along the caustic branches in Fig. 4.1a.

Thus, the branch of the caustic extending into the water column is cut off as the last caustic-forming refracting ray interacts with the subbottom. The location of the caustic cut-off may be easily obtained by substituting the p of the last turning ray into the ray equation, say Eq. (4.1) for c^3-linear profile, to obtain r_c, and then substituting r_c into the equation of the caustic to find the receiver depth z for a given z_0. Figs. 4.5a,b show ray trace diagrams with and without the subbottom for the c-linear profile in the lower half-space. Fig. 4.5a clearly shows the caustic cut-off in the water column where the rays start radiating into a wedge-shaped region without crossing each other.

4.3 The fields near caustics

As discussed in Chapter 2, the asymptotic solution derived in that chapter is not valid for the fields near the caustics where ϕ'' in Eqs. (2.41) and (2.42) becomes very small and vanishes completely at the caustics. The fields in these regions can be evaluated by numerical

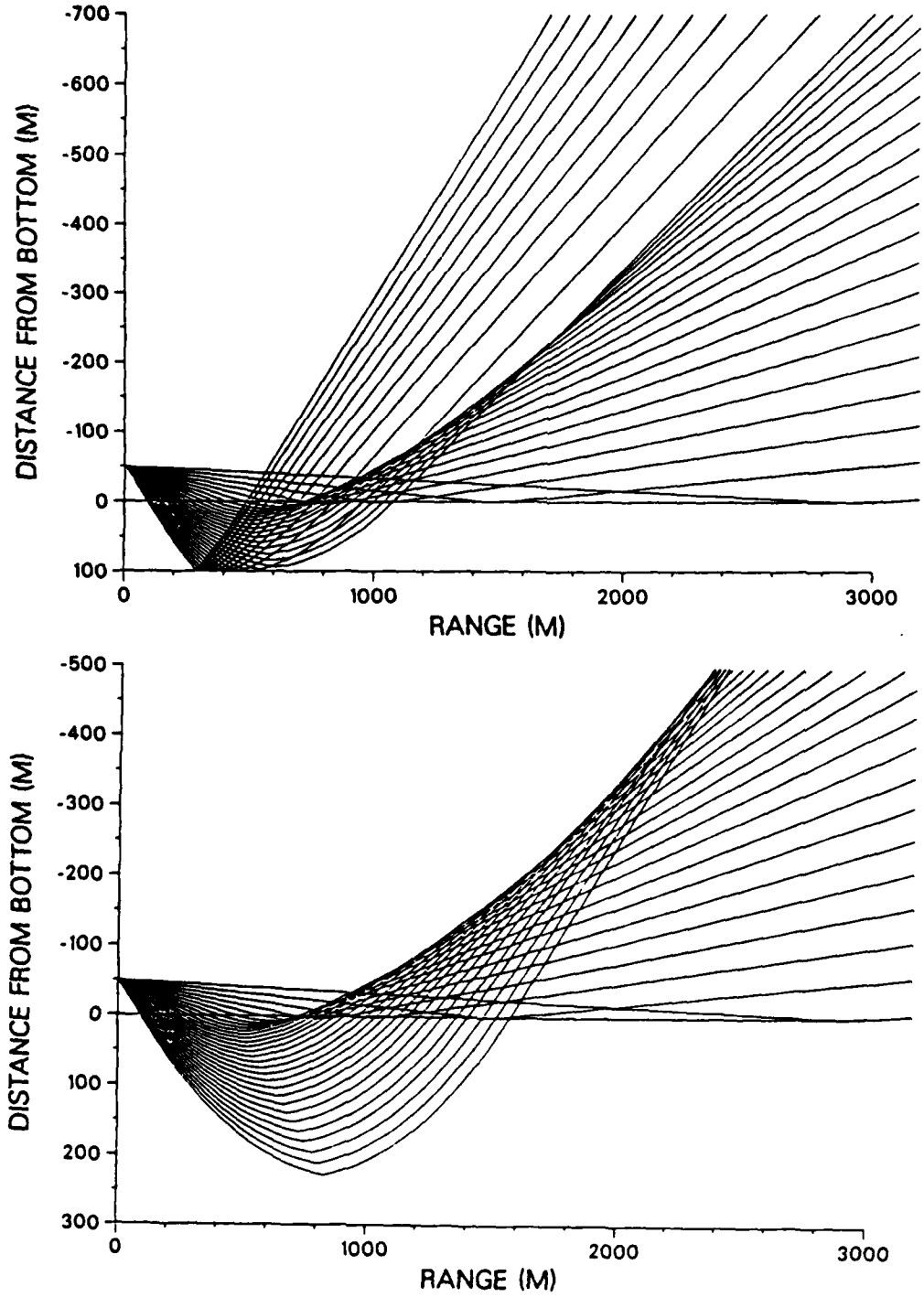

Fig. 4.5 Ray diagrams of the primary reflections for the c-linear profile (a) with the subbottom interface and (b) without the subbotm interface.

integration methods. Analytic solutions to such fields also exist with some limitations. Brekhovskikh's caustic correction to ray theory [3] is only valid for the fields very near the caustics. A uniform asymptotic solution such as the one by White and Pedersen[4] continuously valid across the caustic involves a great deal of mathematics, and it is rather difficult to obtain any physical interpretation of the fields.

In this section we shall emphasize the physical interpretation of the various caustics resulting from the different profile types discussed in Sec. 3.1. The shapes and locations of caustics in the water column have been discussed in Secs. 4.1 and 4.2. Our main interests in this section are to evaluate analytically the strength of the caustic and geometric decay of the fields near the caustic as one moves away from the caustic with horizontal range. Therefore, analytic solutions derived by Brekhovskikh which are only valid near the caustic serve our needs, and we shall discuss the above problems in terms of the three profile types having the same sound velocity gradients at the bottom(cf. Fig. 4.4).

We have modified Brekhovskikh's analytic solution to include the Langer reflection coefficient $R_n(p)$ to the fields near the first order caustic (i.e. $d\phi/dp = d^2\phi/dp^2 = 0$ but $d^3\phi/dp^3 \neq 0$ at $p = p_c$) to obtain

$$P_n \sim 2^{5/6}\omega^{1/6} e^{i\pi/4} \left(\frac{p_c}{r}\right)^{1/2} \frac{R_n(p_c)}{\gamma_0} \left| \frac{d^3\phi(p_c)}{dp^3} \right|^{-1/3} Ai(q) \qquad (4.17)$$

where Ai is the Airy function whose variable q is given by

$$q = \mathrm{sgn}[\phi'''(p_c)]\, 2^{1/3} \omega \left| \frac{d^3\phi(p_c)}{dp^3} \right|^{-1/3} (r - r_c) \qquad (4.18)$$

The value of p_c varies depending on the profile shapes and the source-receiver orientations. Thus, the coefficient of the Airy function in Eq. (4.17) involves many parameters to be examined. However, as discussed in Sec. 4.1.4, if the caustic fields of interest are relatively near the bottom, the variations in p_c, r and R_η are very small since the profile shapes at the top of the layer are very similar. Therefore, the most sensitive quantity is $|\phi'''|^{-1/3}$ which also plays an important role as the weighting factor in the argument of the Airy function, which dominates the variation with range of the field amplitude near the caustic.

In order to evaluate the relative strength of the caustic and the decay with horizontal range, it is useful to overlay the Airy function multiplied by $|d^3\phi/dp^3|^{-1/3}$ evaluated at the p_c corresponding to each profile shape, and plotted against the horizontal distance away from the caustic. For two different values of the source and receiver heights, z + z_0 = 250 m and 50 m, Figs. 4.6a,b show two sets of curves of the mentioned quantity for the three different profile types based on the geoacoustic models shown in Fig. 4.3. The frequency of the harmonic point source is 220 Hz.

For z_0 = 50 m, at z = 0 m all three caustic curves are very similar (cf. Fig. 4.3) and the quantities of $|\phi'''|^{-1/3}$Ai in Fig. 4.6b

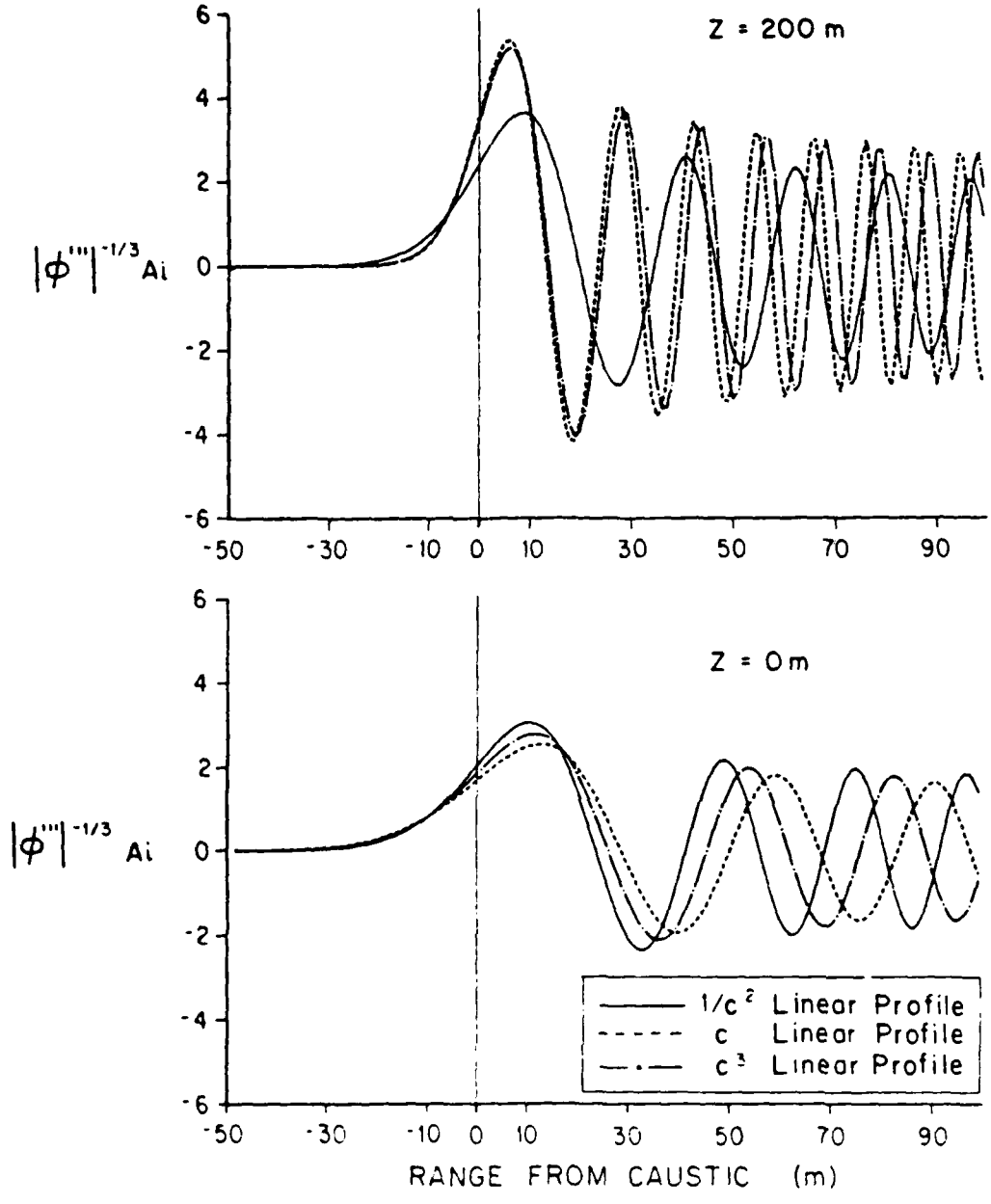

Fig. 4.6a,b The quantity $|\phi'''|^{-1/3}$ Ai vs. horizontal range from the caustic for each profile type at (a) z = 200 m and at (b) z = 0 m.

also show close similarlities among the three profile types. On the other hand, at z = 200 m $|\phi'''|^{-1/3}$Ai for the c and c^3-linear profiles similarly have greater amplitudes and spatial oscillations than at z = 0 m, but the behavior of the $1/c^2$-linear profile remains almost the same at both of the depths. Even though the caustic curves in Fig. 4.3 show well separated traces near z = 200 m, one can observe a similarity between the c and c^3-linear profiles in terms of the radius of curvature while the curve for the $1/c^2$-linear profile yields a sharper turning.

The difference in the field strength can be physically explained by ray interpretations as follows. Let us consider rays forming two types of caustics in a homogeneous medium. One of them is formed along a curve of a small radius of the curvature and the other is formed along a large radius of the curvature as shown in Figs. 4.7a and 4.7b, respectively. As seen in both figures, the rays forming the caustic with the larger radius of the curvature are more densely interacting with each other near the caustic. This results in larger and highly oscillatory interference field amplitude patterns near the caustic as observed in Fig. 4.6a for the c and c^3-linear profiles.

We can conclude from the above observations that when the caustic curves are similar, the associated fields near such caustics are also similar and they are more directly affected by the curvatures of the caustic curves than by the shapes of the profiles.

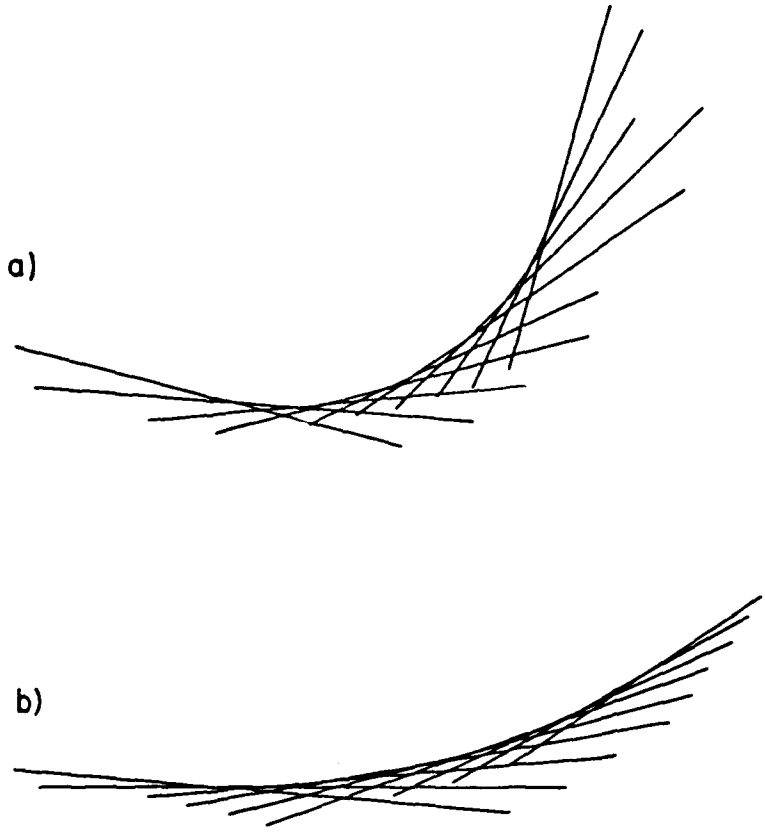

Fig. 4.7a,b Rays forming caustics with a (a) small and (b) large radius of curvature.

References:

[1] Breknovskikh, L. M., Waves in Layered Media, 2nd ed., Academic Press, New York, 1980.

[2] Frisk, G. V., "Determination of sediment sound speed profiles using caustic range information," Bottom-Interacting Ocean Acoustics, Ed. Kuperman, W. A. and Jensen, F. B., Plenum Publishing Corporation, New York, 1980.

[3] Reference [1], Sec. 45.

[4] White, D. W. and Pedersen, M. A., "Evaluation of shadow zone fields by uniform asymptotics and complex rays," J. Acoustical Soc. Amer. 69, 1029-1059 (1981).

Chapter 5: Analysis of Experimental Data

We have examined various geoacoustic models using an asymptotic expansion method based on the Langer reflection coefficients in Chapter 3. In this chapter we shall examine two sets of experimental data obtained from field experiments and estimate the geoacoustic properties of the ocean bottom from these data using the asymptotic expansion method. After finding geoacoustic models such that the resulting total fields agree with the measurements satisfactorily, we shall demonstrate the energy partitioning of the eigenrays with horizontal range, so that the physical mechanisms causing the real fields may be understood. We shall also discuss the effect of source/receiver geometry on the determination of geoacoustic models.

Data Set 1: Icelandic Basin

Field measurements were taken in the Icelandic Basin (59 31.0'N, 17 20.8'W) by Frisk and his co-workers[1]. The total acoustic pressure field due to a 220-Hz harmonic point source towed at an elevation of 157 m above the ocean bottom(cf. Fig. 1.2) was measured by a receiver moored at 54.6 m above the bottom. It has been found by Frisk[1](with modifications by the author) that the geoacoustic model shown in Fig. 5.1 seems to provide the best synthetic fields which match with these measurements. Both synthetic and real data are shown in Fig. 5.2.

We next generate reflected fields based on this geoacoustic model and group them into three ray types: specular, primary and multiple

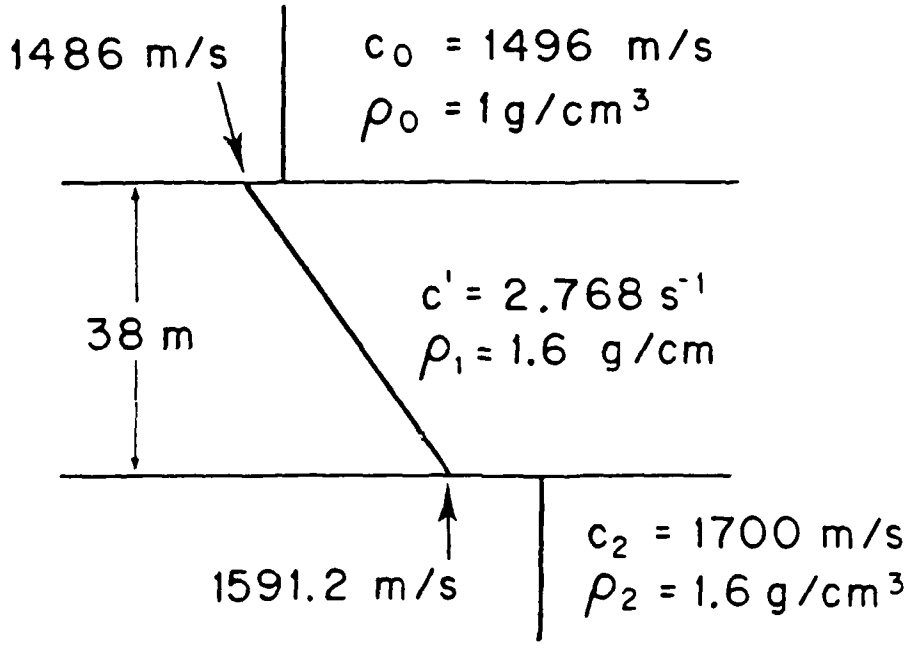

Fig. 5.1 Geoacoustic model for the Icelandic Basin.

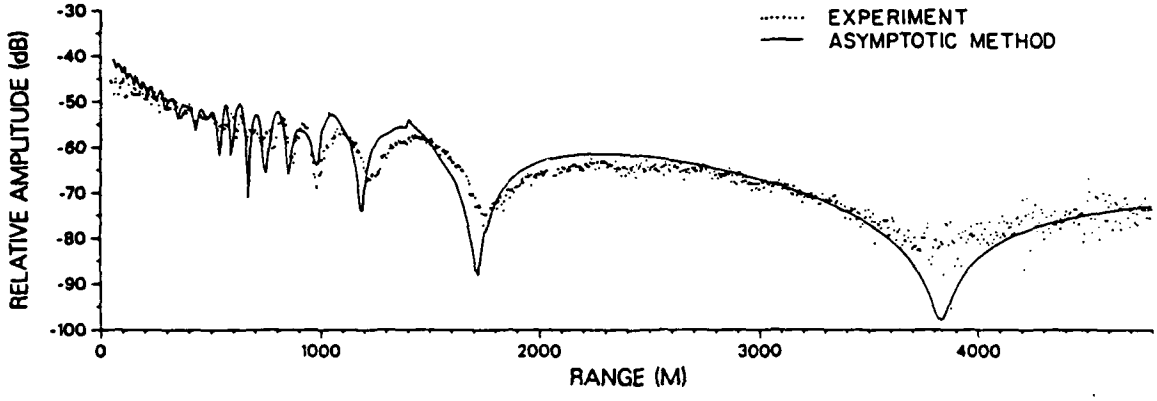

Fig. 5.2 A comparison between experiment and asymptotic method using the geoacoustic model shown in Fig. 5.1. The source frequency is 220 Hz and the source and receiver heights are 157 m and 54.6 m, respectively.

reflections. As shown in Fig. 5.3, the primary reflection clearly dominates the total reflected field (excluding the direct field) for ranges up to 5 km even though the sound velocity gradient is the largest we have examined so far and one would expect a greater contribution from the multiples(cf. Sec. 3.2.1). This is due to the fact that the water column occupies a large portion of the total ray path even for the multiples(cf. Fig. 5.4), and the condition given by Eq. (3.24) is violated (the R. H. S. of Eq. (3.24) is about 30 m, while $(z + z_0)$ is 211.6 m).

Therefore, although the geometric spreading due to the layer-path is relatively small for the steep sound velocity gradient at the bottom, this does not contribute much to reducing the total geometric spreading of the multiples. Given an insignificant contribution to the field amplitude from the steep sound velocity gradient at the bottom, the primary reflection which has the maximum reflection coefficient amplitude after critical incidence dominates the total reflected field.

Based on these observations we can also conclude that the sound velocity at the top of the layer and the gradient in the layer, which most affect the behavior of the primary reflection, particularly its geometric spreading, are mainly responsible for the nature of the total reflected field at these ranges. The geoacoustic model shown in Fig. 5.1 is the result of using such modeling criteria to determine the sound velocity at the top of the layer and the gradient in the layer to improve the agreement between the measurement and synthetic fields.

The fact that in this case geometric spreading is heavily dependent upon the water-path and not the layer-path makes the identification of geoacoustic models somewhat more difficult, particularly the shape of

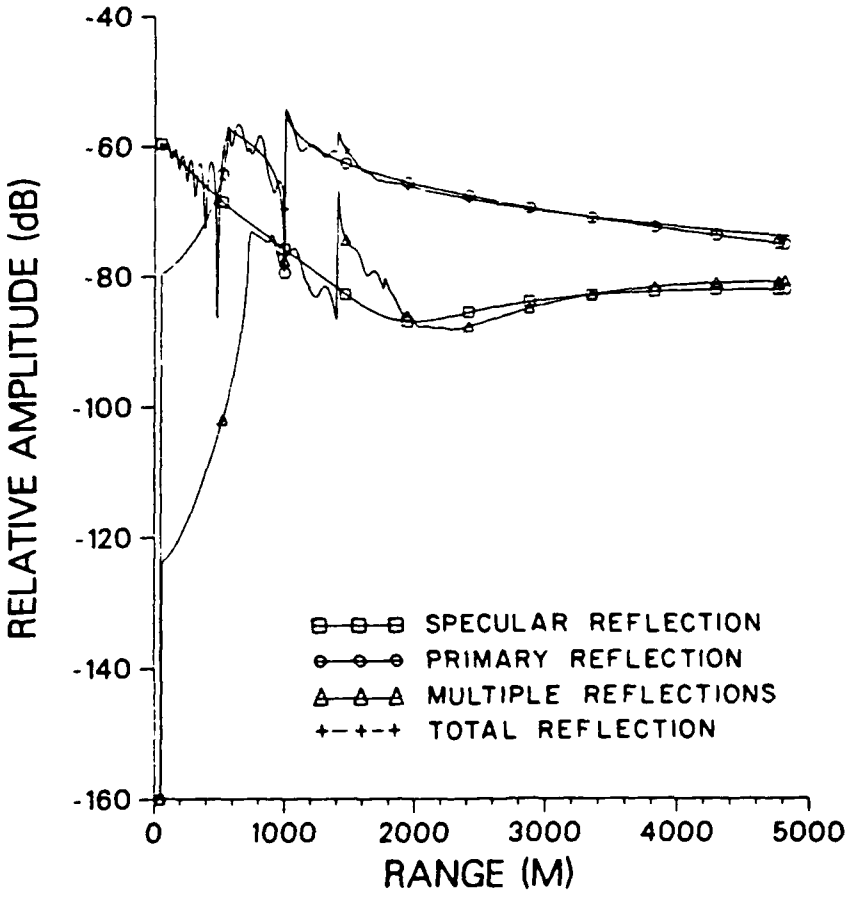

Fig. 5.3 The reflected fields for the geoacoustic model shown in Fig. 5.1. at $z + z_0 = 211.6$ m

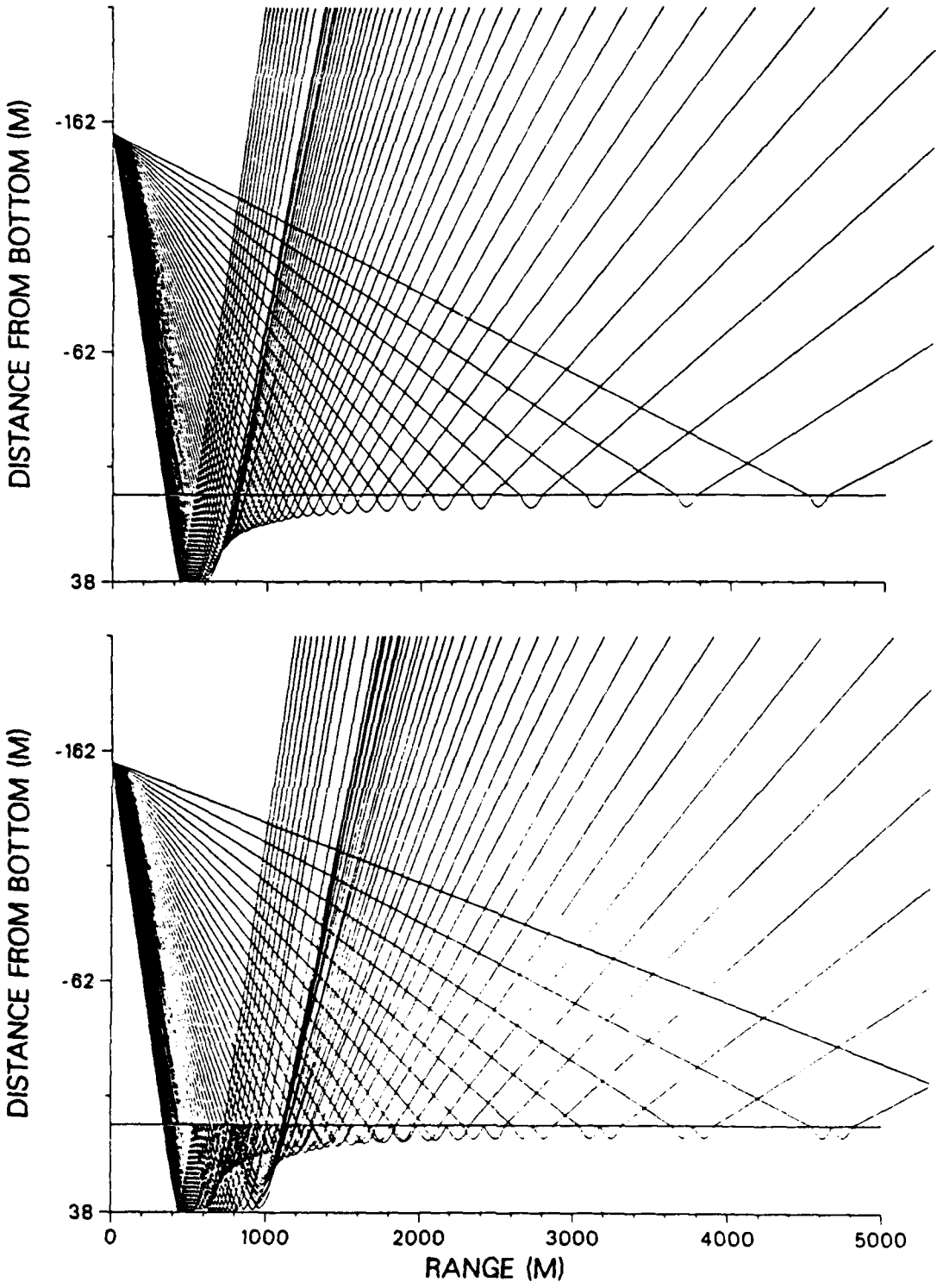

Fig. 5.4 Ray diagrams of the (a) primary reflections and (b) second multiple reflections for the model shown in Fig. 5.1.

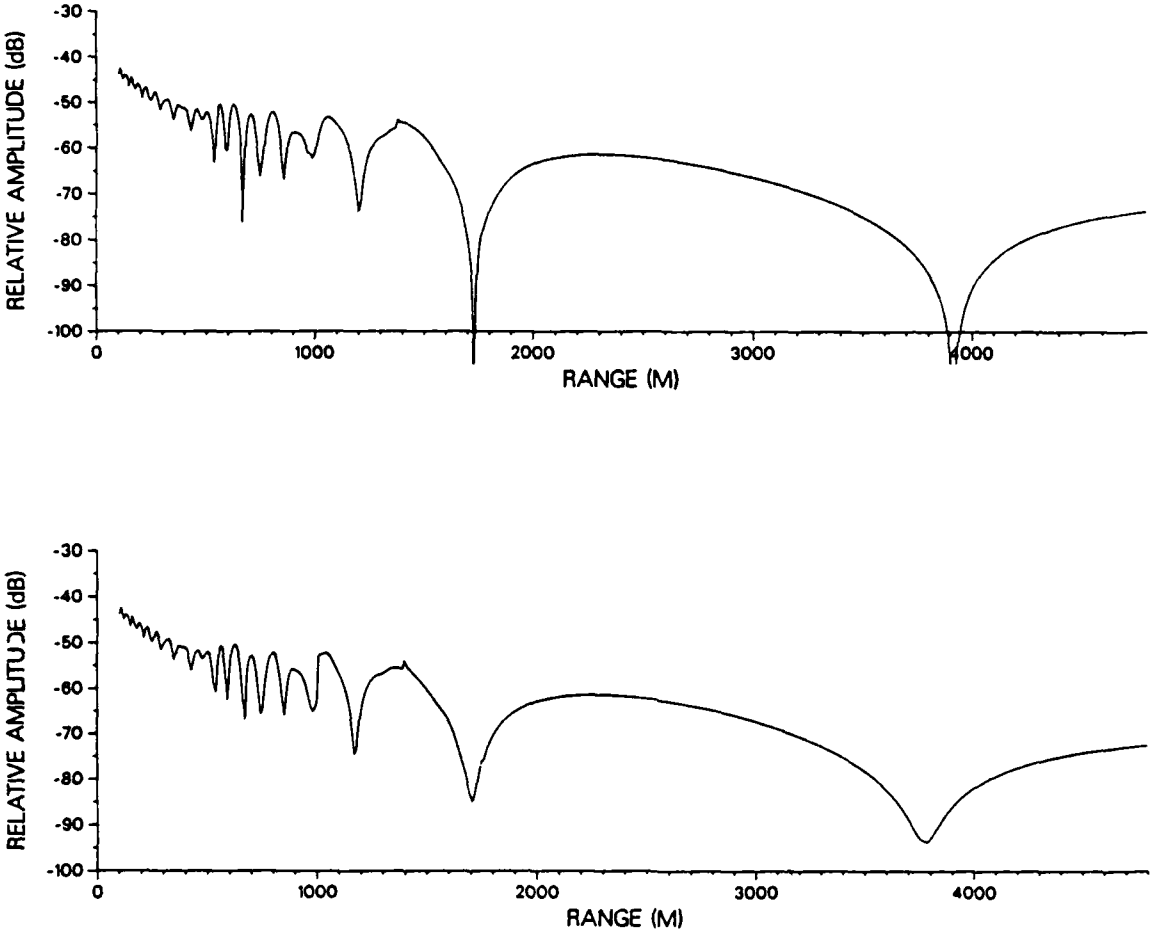

Fig. 5.5 Synthetic data for the (a) $1/c^2$-linear profile and (b) c^3-linear profile instead of the c linear profile in the layer shown in Fig. 5.1.

the profile associated with the sound velocity gradient at the bottom. This is not the same as saying that matching the synthetic fields to the measurements is difficult.

As an example, Fig. 5.5 shows two sets of the total field: one from the $1/c^2$-linear profile and the other from the c^3-linear profile for fixed endpoints of the sound velocity in the layer. It is evident that all of the total fields generated from the geoacoustic models with different profile types, including the one shown in Fig. 5.2, have good agreement with the measurements.

Therefore, when the source and receiver are placed at relatively high elevation above the bottom so that the water-path dominates the total geometric spreading, the total fields measured at these receiver locations are insensitive to the shape of the bottom layer profile, and thus the identification of this property of the bottom structure becomes very difficult. In the next example, we shall demonstrate that the effect of the profile shape is indeed significant when the source and receiver heights are reduced.

Data Set 2: Hatteras Abyssal Plain

We next examine experimental data collected in the Hatteras Abyssal Plain (34 00.0'N, 67 00.0'W) with the same experimental configuration as in the previ- ous example except that the source and receiver heights are now 180 and 2.7 meters, respectively. The estimated geoacoustic model for this region is shown in Fig. 5.6. where the average water sound velocity was used from the model by Frisk[2]. The measurement of the total field is shown along with the synthetic field based on our geoacoustic model in

Fig. 5.7. Due to the comparable size of the source plus receiver heights and the sediment layer thickness(c.f. Ray trace diagram in Fig. 5.8), this example demonstrates a sensitive dependence on the shape of the sound velocity profile in the layer despite the small reference sound velocity gradient($dc/dz = 1\ s^{-1}$ as opposed to a value of nearly $3\ s^{-1}$ for the previous example).

Except at ranges near r = 2000 m, both real and synthetic fields agree well. This agreement is especially good at very long ranges as the result of the c^3-linear profile being used for the sound velocity in the layer. If one instead takes the profile in the layer to be $1/c^2$-linear for the same fixed endpoints, the resulting synthetic field shows a very different behavior, as seen in Fig. 5.9. We note that the large peak at and just beyond the caustic has become narrower. As shown in Fig. 5.10, this is due to there being a narrower horizontal range band in which the primary reflections can interfere with each other.

The profile-dependent differences in the reflected field amplitudes seen at long range can be analyzed by comparing their grouped reflected fields, shown in Figs. 5.11 and 5.12 for the c^3 and $1/c^2$--linear profile shapes, respectively. Except near the caustic ranges, the gross variations of the field amplitudes of each reflection are almost the same. However, the total reflected field amplitude behaves somewhat differently in each case with respect to that of the primary reflection. This indicates that for each reflection there are more sensitive variations in phase rather than in amplitude due to the variation in profile shape.

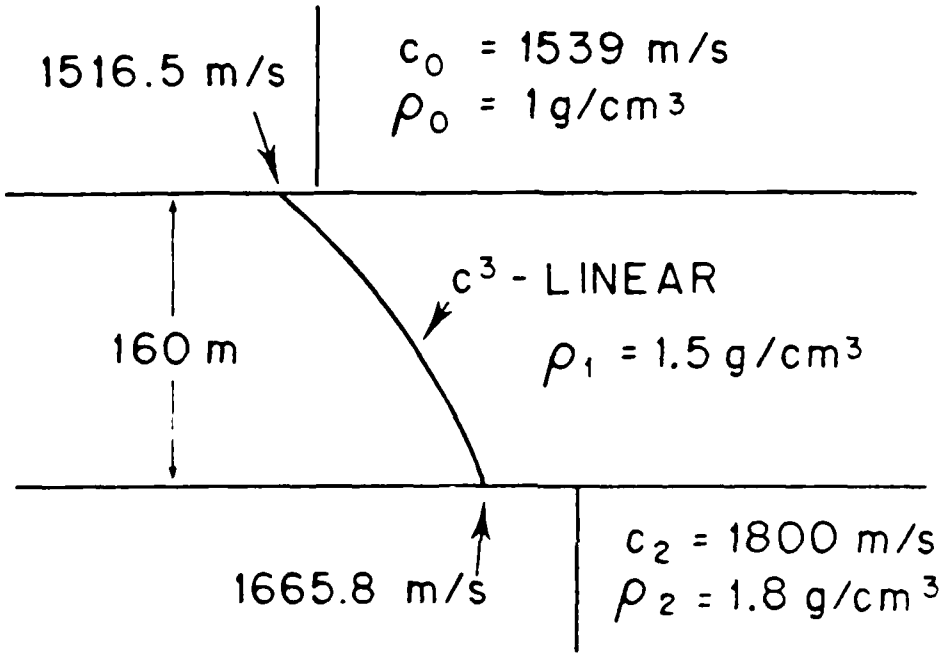

Fig. 5.6 Geoacoustic model for the Hatteras Abyssal Plain.

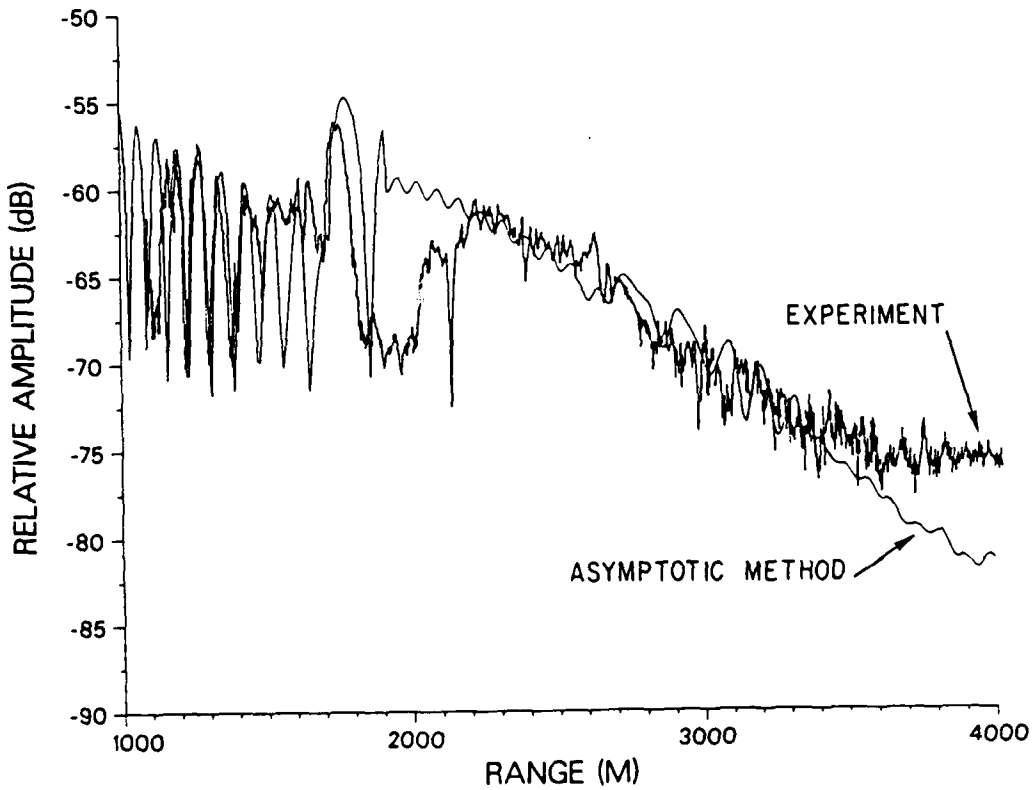

Fig. 5.7 A comparison between experiment and asymptotic method using the geoacoustic model shown in Fig. 5.6.

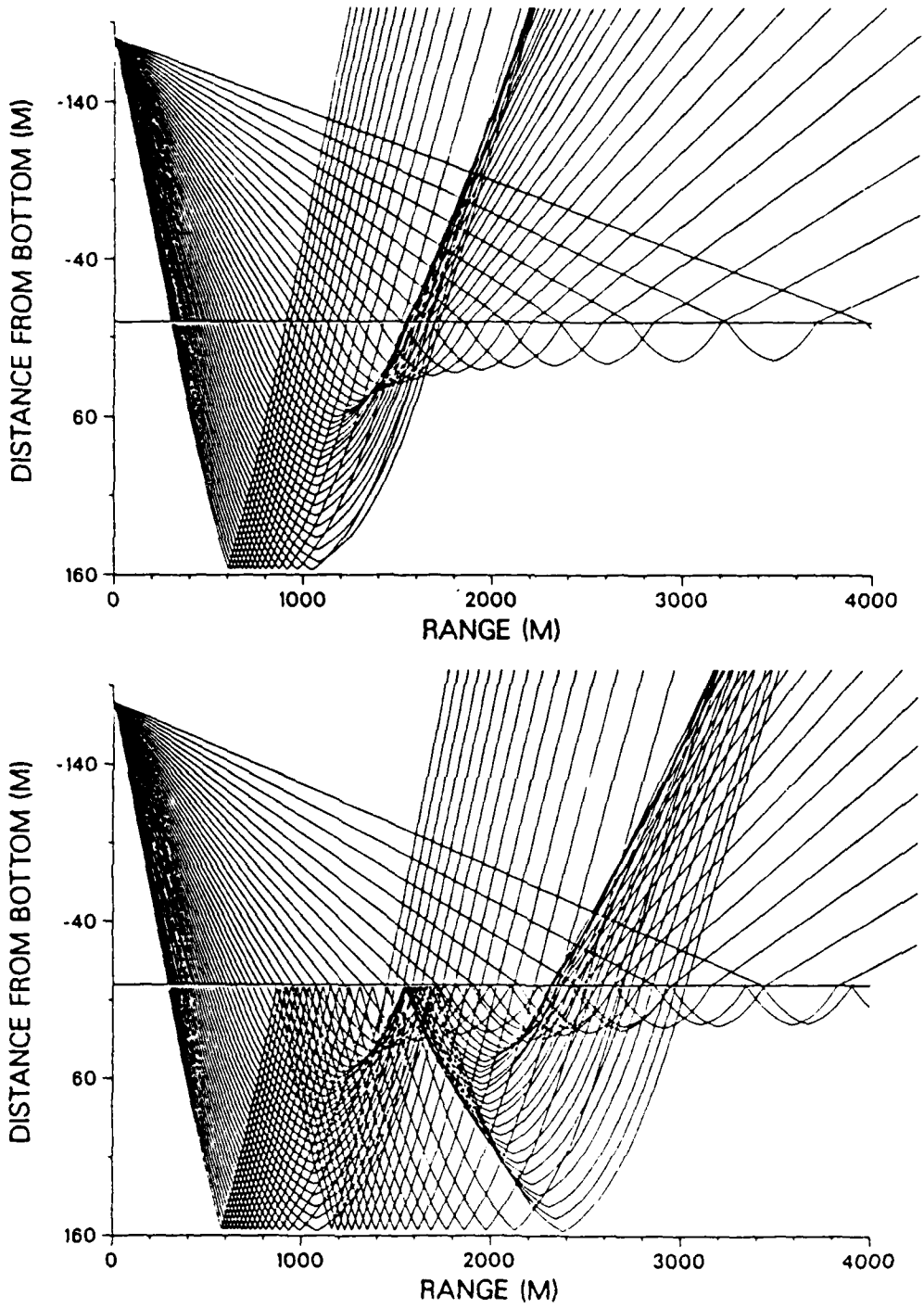

Fig. 5.8 Ray diagrams of the (a) primary and (b) second multiple reflections using the geoacoustic model shown in Fig. 5.6.

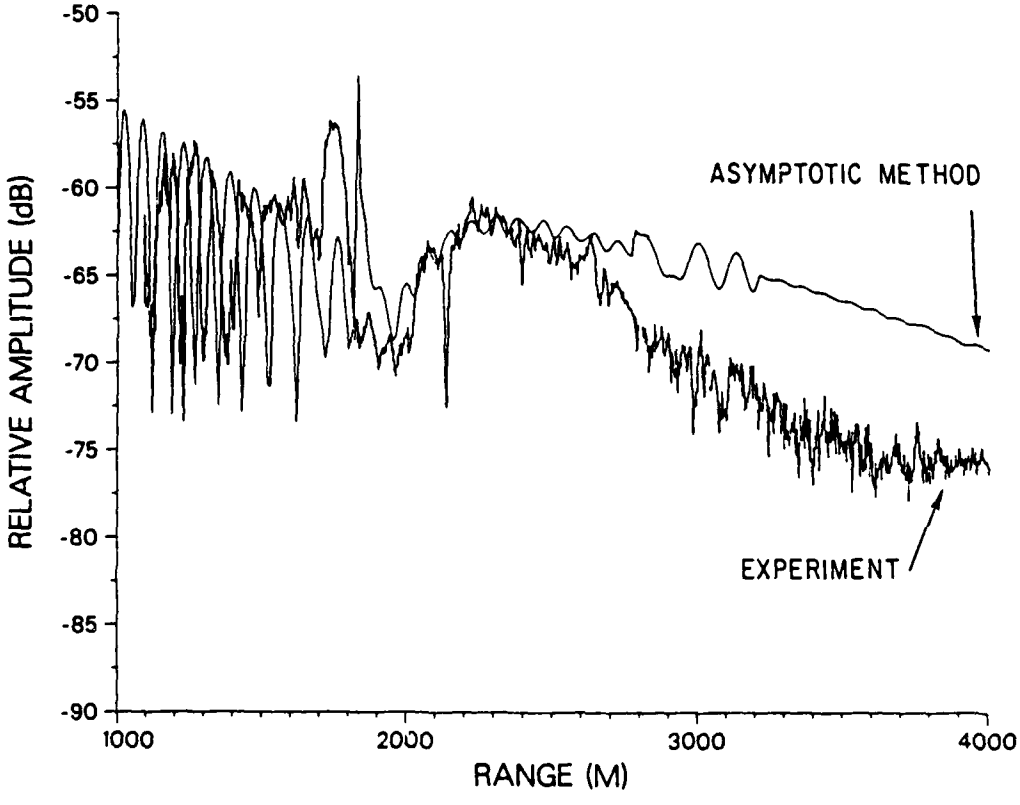

Fig. 5.9 A comparison between experiment and asymptotic method using the $1/c^2$-linear profile.

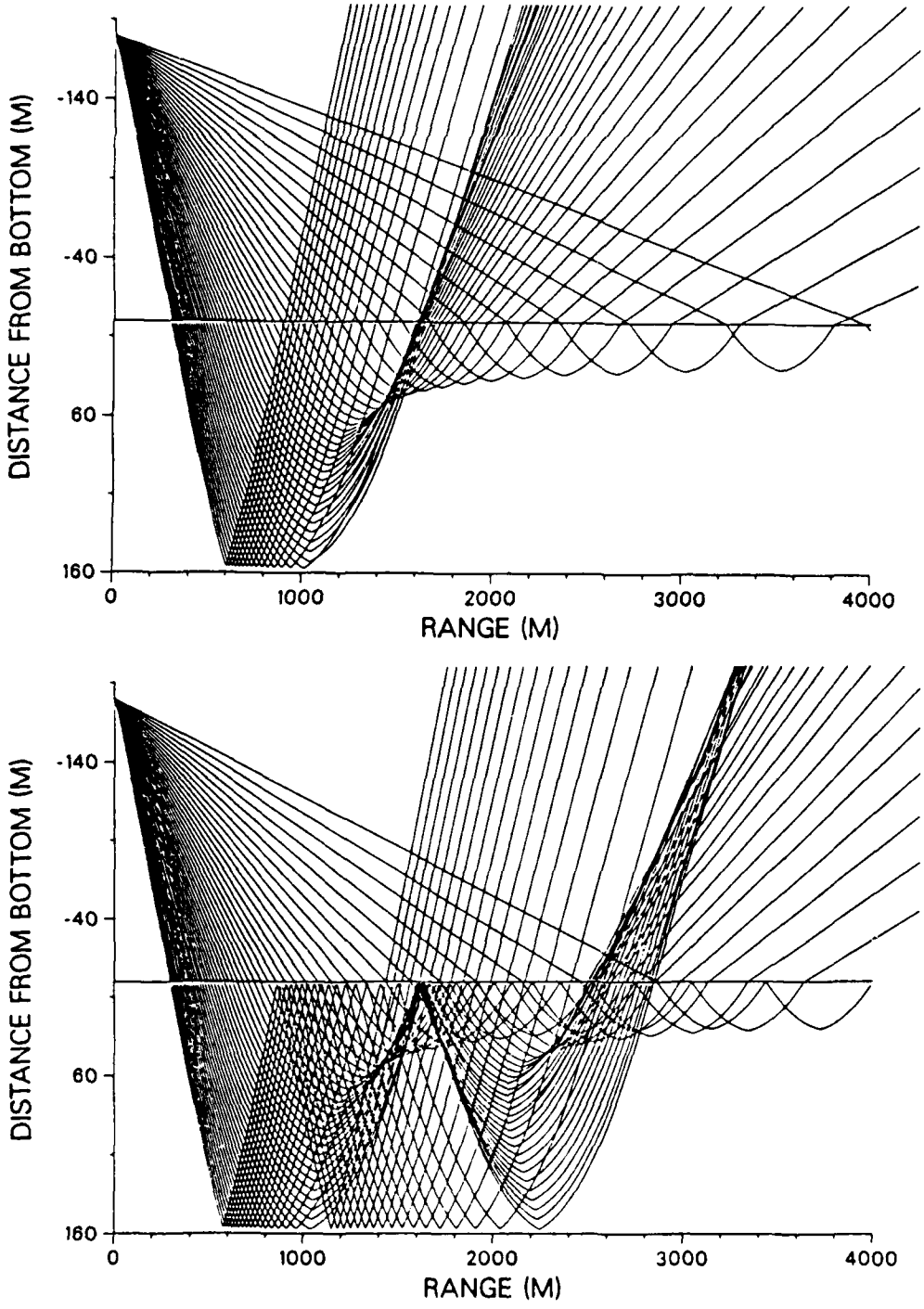

Fig. 5.10 Ray diagrams of the (a) primary and (b) second multiple reflections using the $1/c^2$-linear profile.

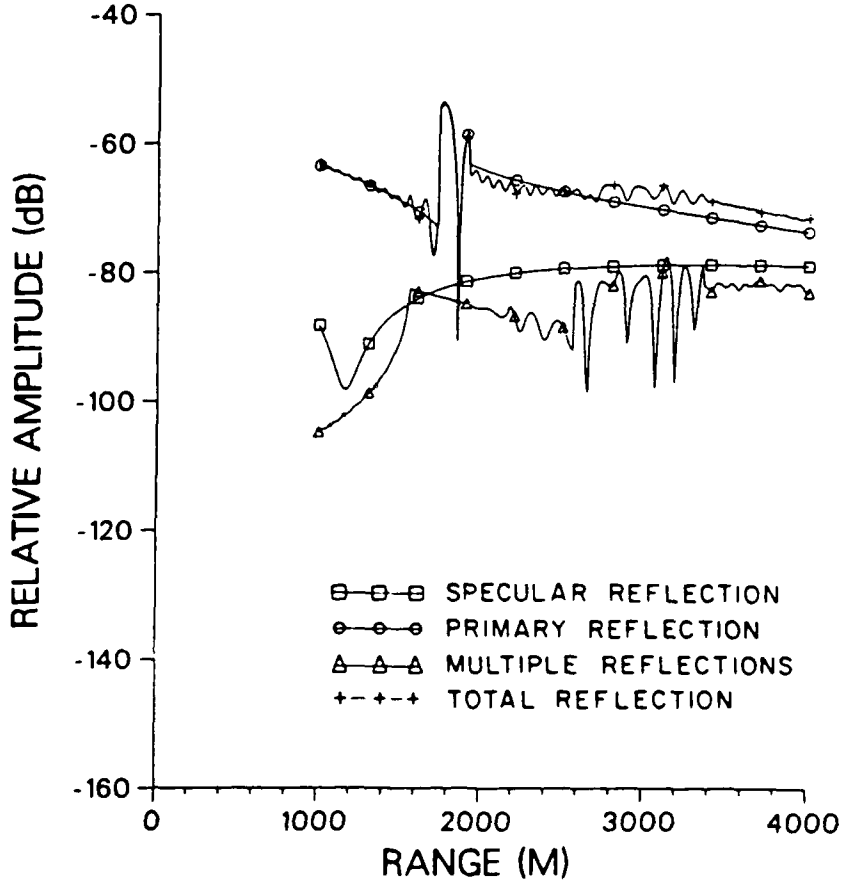

Fig. 5.11 The reflected fields for the geoacoustic model shown in Fig. 5.6 at $z + z_0 = 182.7$ m.

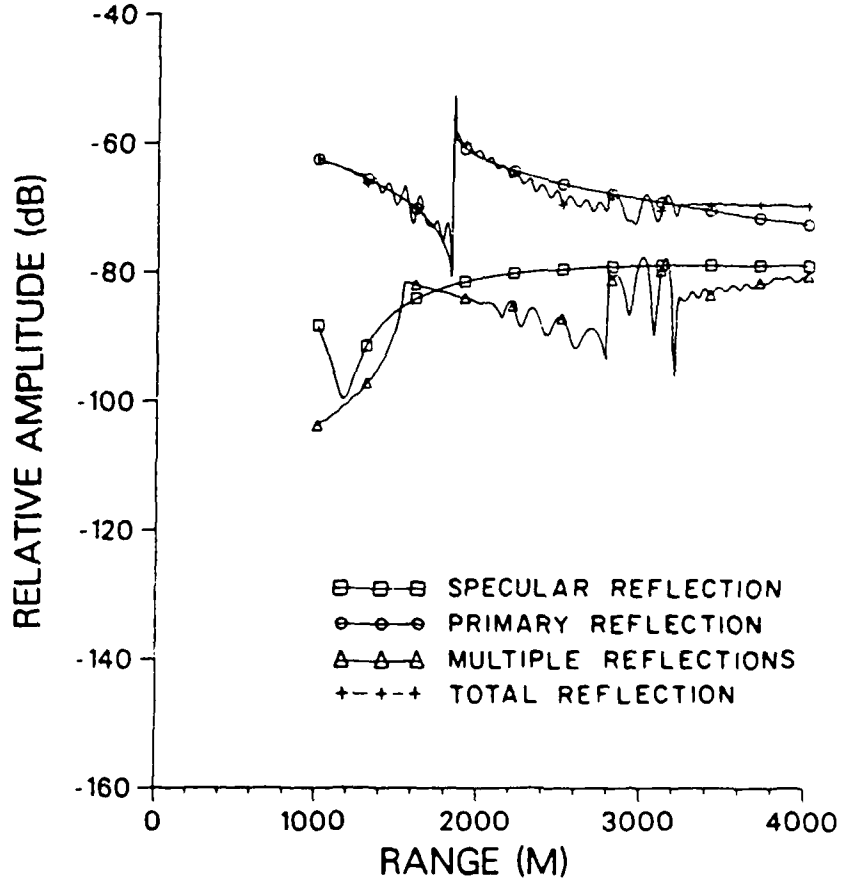

Fig. 5.12 The reflected fields for the $1/c^2$-linear profile at $z + z_0 = 182.7$ m.

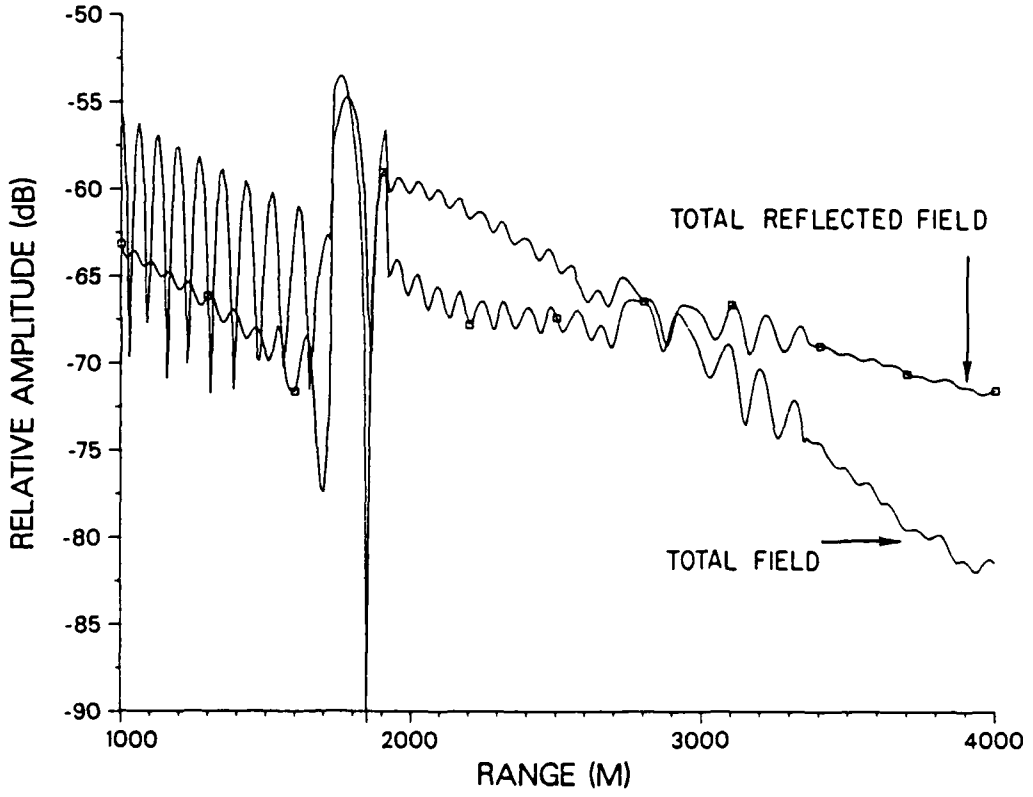

Fig. 5.13 A comparison between the total field and total reflected field for the c^3-linear profile.

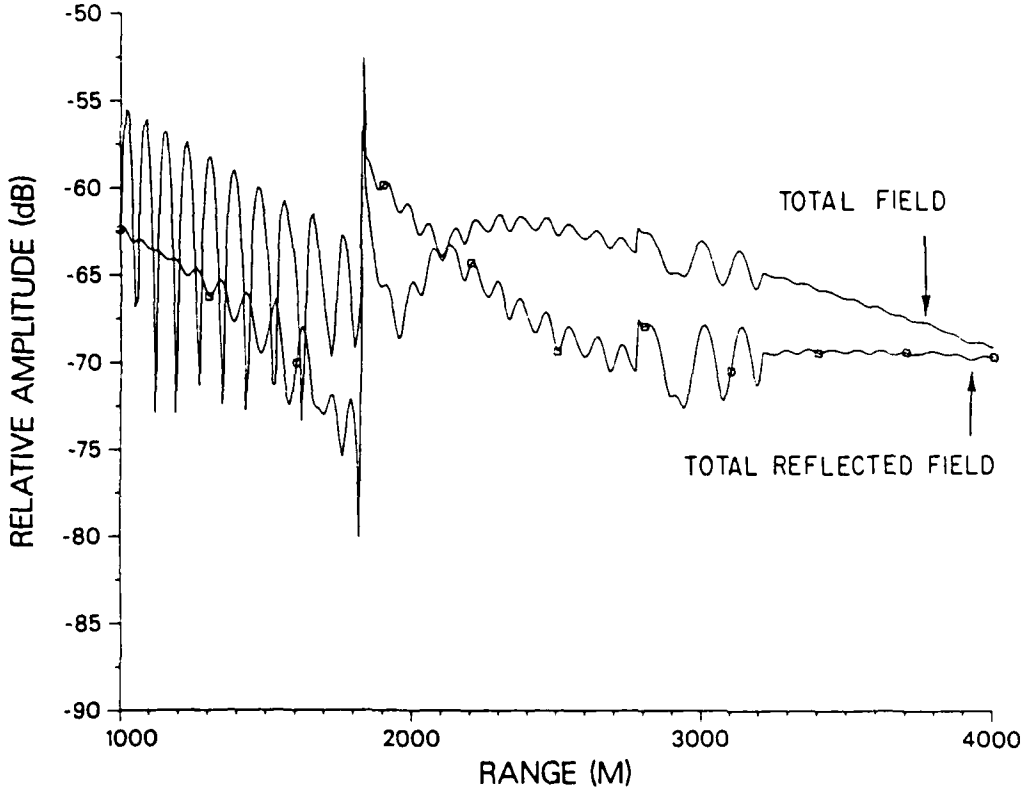

Fig. 5.14 A comparison between the total field and total reflected field for the $1/c^2$-linear profile.

When the total reflected fields interfere destructively with the direct field at long ranges($r > 2800$ m) as shown in Fig. 5.13, one sees a rapid amplitude decay with horizontal range in the measurement. For the $1/c^2$-linear profile, the total reflected field interferes constructively with the direct field at these ranges as shown in Fig. 5.14. One sees here that the change in profile shape makes the greatest contribution to the phase variations, and not to the amplitude, which can result in a large difference in the total field as the reflected fields interact with the direct field.

Summary:

In both examples, the primary reflection is found to be the major contributor to the total reflected field. In the first case, the sound velocity gradient at the bottom is large but the value of $(z + z_0)$ is also large. In the second case, the sound velocity gradient at the bottom is small but the value of $(z + z_0)$ is relatively small. Due to the large water-path geometric spreading in the first case and the small sound velocity gradient at the bottom in the second case, the multiple contributions become small. Also, the primary reflection coefficient amplitude remains large up to the range of interest so that the specular reflection coefficient amplitude stays lower for all ranges in both cases(cf. Fig. 3.10 for example). Therefore, in general, a large value for $(z + z_0)$ enhances the contribution from the primary reflection at long ranges.

It is also found that the major effect of the shape of the profile in the bottom layer is on the phase variation of the reflected field

which leads to the characteristic gross features of the total field amplitude as the direct water field is coherently added to the reflected field. However, this effect would be negligible if the water-path dominated the total geometric spreading as the source and receiver are placed at high elevations above the ocean bottom.

Geological data near the experimental sites:

In order to relate the physical features of the geoacoustic models used in this chapter to the actual geological properties of the experimental sites, seismic and core sample data from the Deep Sea Drilling Project(D.S.D.P.) were searched. The major objective was to identify the subbottom reflector in our geoacoustic models from the D.S.D.P. data.

The seismic reflection data at 60-320 Hz taken near the D.S.D.P. sites 116 and 117, which are the closest locations to the experimental site, indicate the first reflector depth varying from 150 to 275 meters even though their physical locations are very close to each other[3]. It is therefore inappropriate to extrapolate the depth of the first reflector, namely the subbottom interface, from these data which were collected at least 2.5 degrees in latitude away from the actual site. The presence of a subbottom reflector at 38 meters below the waterbottom interface at the experimental site was confirmed by 3.5 kHz normal incidence records taken at the site. Also yellow mud, and yellow mud and shells were collected from 19-foot and 25-foot core samples, respectively, at two different locations within the area[1].

In the case of the Hatteras Abyssal Plain the depth of the subbottom interface agrees reasonably well with that of the first acoustic

horizon A^T from the drilling site 387 on the western Bermuda Rise[4]. Horizon A^T correlates approximately with the top of a sequence of middle Eocene siliceous turbidites (lithologic sub-unit 3A) which underlies upper Eocene radiolarian mud (Unit 2). Other acoustic reflectors were also well defined and their geological correlations could be determined from the core samples with reasonable confidence. The subbottom depths resulting from seismic reflection and refraction profiling by Emery et. al.[5] and Houtz and Ewing[6] near the experimental site were 130 meters and 215 meters, respectively, and consistent with Frisk's estimate of 160 meters. Therefore, it suggests that the subbottom interface may correspond to the first acoustic horizon A^T observed near the drilling site. The information on geological properties of deep ocean sediments is often not available; thus performing the bottom acoustic experiments near well logged D.S.D.P. sites may increase confidence in geoacoustic modeling and testing of theoretical results.

References:

[1] Frisk, G. V., private communication.

[2] Frisk, G. V., Doutt, J. A. and Hays, E. E., "Bottom interaction of low-frequency acoustic signals at small grazing angles in the deep ocean," J. Acoust. Soc. Am. 69, 84-94 (1981).

[3] Davies, T. A. ed., Initial Reports of the Deep Sea Drilling Project, Vol. XII, National Science Foundation, Washington, D. C., 1972.

[4] Kaneps, A. ed., Initial Reports of the Deep Sea Drilling Project, Vol. XLIII, National Science Foundation, Washington, D. C., 1979.

[5] Emery, K. O., Uchupi, E, Phillips, J. D., Bowin, C. O., Bunce, E. T., and Knott, S. T., "Continental Rise off Eastern North America," Am. Assoc. Petrol. Geol. Bull. 54, 44-108 (1970).

[6] Houtz, R. E. and Ewing, J. I., "Detailed Sedimentary Velocities from Seismic Refraction Profiles in the Western North Atlantic," J. Geophys. Res. 68, 5233-5358 (1963).

Chapter 6: Contributions and Related problems

In this final chapter we shall summarize the results obtained in Chapters 2 through 5 and discuss the contributions made here to the field of ocean bottom acoustic interaction. We shall also discuss other related problems raised during this research and possible techniques to solve them.

6.1 Contributions

Most of the mathematical discussion in this thesis was devoted to the analytic evaluation of ocean bottom reflected acoustic fields given in the form of the Sommerfeld integral. Within the formulation we used realistic geoacoustic models and examined the sensitivity of the fields generated to the geoacoustic parameters.

The asymptotic method for approximating the Sommerfeld integral was derived in Chapter 2. The total reflected fields were given by a series of asymptotic solutions to the fields associated with eigenrays. Since the reflection coefficients as weight factors in the integrand were derived analytically based on realistic geoacoustic models using Langer uniform asymptotic approximation, the resulting asymptotic solutions were also analytic expressions for these geoacoustic models.

The accuracy of the method was confirmed by comparison with numerical Hankel transform results except in regions where critical incidence and caustic formation take place. We have also derived the asymptotic expressions based on the Langer reflection coefficients for the inter-

face wave propagating along the subbottom interface corresponding to the n-th multiple reflection.

In Chapter 3, a new canonical analytic expression for the sound velocity profile was introduced. We demonstrated in Appendix D that a sound velocity c expressed by c^3-linear in depth provides a very similar profile shape to the one observed from field measurements. Using the analytic expression for the phase integral for this profile type, we obtained complete analytic solutions to the reflected fields based on this geoacoustic profile shape as well as for the cases of the $1/c^2$ and c-linear types.

We then applied the above results to examine several types of geoacoustic models varying in layer thickness, sound velocity gradient, profile shapes and source-receiver geometry and demonstrated complex features of energy partitioning of eigenrays with horizontal range. Because of the accuracy of the plane wave reflection coefficients we derived, our method should be valid even for geoacoustic models with a thin layer(i.e. thickness less than a wavelength) where ray theory is believed not to be valid.

The effect of the sound velocity gradient at the bottom on the geometric spreading for near-grazing incidence was qualitatively discussed. The conditions under which the layer-path of the n-th multiple dominates the total geometric spreading were also derived for this case. It was proved that the differences in profile shape were minimal for a small gradient and/or a small layer thickness for fixed endpoints of the sound velocity in the layer. However, in the case of a large layer thickness and small gradient, slight differences in profile shape

caused relatively large differences in caustic position though the field amplitudes were very similar including the fields near the caustics.

In Chapter 4, we derived the caustic equations for the $1/c^2$ and c^3-linear profiles. We found that the cusp of the caustic from the $1/c^2$-linear profile always corresponds to a grazing angle of $\pi/6$ independent of the source-receiver geometry and the sound velocity gradient. We also demonstrated that the leading term of the asymptotic expansion for the fields near the caustic is directly influenced by the amount of curvature in the caustic curve.

Two sets of field measurements were discussed in Chapter 5. The energy partitioning of the eigenrays was analyzed and it was found that the primary reflection dominated the total reflected field at most ranges for both cases. We also discussed the accuracy obtained in modeling the ocean bottom relative to the geometric orientation of the source and receiver for given bottom structures.

While the density and sound velocity discontinuities at the boundary interfaces determined the gross features of the amplitudes of the reflected fields, sensitive ray-phase variation due to the shape of the profile in the layer became important as the direct field was coherently added to the total reflected field. However, when the source-receiver heights were large so that the variation of the water-path with respect to that of the layer-path became large, the total field amplitude became insensitive to the profile shape. The discussion on this issue will be continued in the next section.

The group of acoustic properties of the bottom which affect the reflected fields given in this thesis is clearly not complete. We have

just started to deal with mathematical models representing the basic acoustic properties of a horizontally stratified bottom that one may find in the real world. Without even complicating these models there are still many problems remaining. A survey of such problems will be discussed next.

6.2 Related problems

Additional aspects of acoustic bottom interaction will be discussed in this section. Some of these are experimental subjects, others are purely mathematical.

6.2.1 Suggested deployment depths of the receiver system and an iterative inverse scheme

We extend here the discussion given in Chapter 5 and propose a simple scheme to recover the acoustic properties of the ocean bottom using a forward modeling technique such as the one developed in this thesis. We have concluded in Chaps. 3 and 5 that in order to model the bottom accurately, including the profile shape, one should minimize the sum of the source and receiver heights to enhance the layer-path over the water-path.

This indicates that it might be desirable to make a preliminary estimate of the layer thickness by means of standard vertical profiling (such as measuring the travel time of a pulsed signal propagating normal to the ocean bottom), and then to deploy the system of receivers according to the estimated layer thickness for oblique incidence work. One receiver should be deployed at the depth where the source-receiver sum

does not exceed the layer thickness. The other should probably be located at a higher elevation off the bottom. We realize from the discussion in Sec. 3.2.1 that the source-receiver sum should be determined from the sound velocity gradient at the bottom, not from the layer thickness. However, since this quantity is not known at this stage of the experiment, estimating the lower end of the sum of the source and receiver heights from the layer thickness is the best one can be expected to do.

We have seen that the fields measured at long ranges by the top receiver are dominated by the interaction between the refracting rays of primary reflection and the direct water-path field (the other types of reflections are suppressed by their greater geometric spreading). This indicates that it may be possible to match the sum of the direct and primary reflection to the gross feature of the real data at long ranges by using an even simpler geoacoustic model with a monotonically increasing sound velocity profile (of the c-linear type for example) in the lower halfspace without the subbottom interface. As both models (with and without the subbottom) show reasonable agreement, we are obviously measuring most sensitively the sound velocity and sound velocity gradient at the water bottom interface. The success Frisk had in obtaining a geoacoustic model using the parabolic equation method[1] can be explained by these same arguments, since specular reflection was not explicitly included in those calculations and the effect of the subbottom (they modeled it as a soft boundary) was negligible at long ranges.

By matching the fields at both receivers at short ranges with the specular reflection included (but not multiples), one fixes the subbot-

tom interface. Finally, by matching the fields at long ranges at the lower receiver with multiples now included, one can "fine-tune" the profile shape as well as the sound velocity discontinuity at both interfaces.

Of course, the actual search for geoacoustic models which match the data is not quite as straightforward as the procedure described here, which is based on purely mathematical models. It may also prove impossible to suspend the source very close to the bottom to see layers of small thickness.

6.2.2 Application of the Langer reflection coefficient to a numerical method

It was noted that the evaluation of the plane wave reflection coefficient via the propagator-matrix method involves some difficulties, both in selecting a step size for the profile and in computing time[2]. As shown in Fig. 2.2, the accuracy of the Langer reflection coefficient is quite good and as long as the geoacoustic model is of the type considered in this thesis, the (total or partial) Langer reflection coefficient could be substituted in the Sommerfeld integral to be evaluated numerically by the Hankel transform method[3,4]. This scheme should also be a good alternative to the asymptotic method introduced here when it fails at critical incidence and caustics where more accurate fields are desirable.

6.2.3 A partial expansion of the total Langer reflection coefficient

We expanded the total Langer reflection coefficient before the evaluation of the Sommerfeld integral. This approach was suitable to distinguish one ray-type field contribution from the others. However, it is not necessarily the most efficient method for computing the total reflected fields. Specifically, the multiple contributions involve long, tedious summations, and we are often only interested in the total contribution of the multiples, but not in the separate multiple reflections.

Therefore, the following expansion is suggested instead:

$$R(p) = \frac{A_0^{(2)} - B_0^{(2)}}{A_0^{(2)} + B_0^{(2)}} + \frac{4\rho_0\rho_1\gamma_0 S_0}{\pi(A_0^{(2)} + B_0^{(2)})^2} \frac{A_H^{(2)} - B_H^{(2)}}{A_H^{(2)} - B_H^{(2)}}$$

$$\times \left[1 - \frac{(A_0^{(1)} + B_0^{(1)})(A_H^{(2)} - B_H^{(2)})}{(A_0^{(2)} + B_0^{(2)})(A_H^{(1)} - B_H^{(1)}) - (A_0^{(1)} + B_0^{(1)})(A_H^{(2)} - B_H^{(2)})}\right] \tag{6.1}$$

where the first and second terms represent specular and primary reflections respectively, as calculated in Eq. (2.27), but the last term is a composite expression of the rest of the multiples.

The first two terms may be substituted in the Sommerfeld integral to be evaluated asymptotically; these provide ray-type field solutions. However, the last term involves singularities for which the normal mode representation may prove ideal. The evaluation of the total contribution due to the multiples would then involve locating residues in the

complex p-plane. This procedure, though it may involve numerical difficulties, would probably be more efficient than the one used in this thesis, particularly when a large number of multiples contribute to the field.

6.2.4 Limiting cases of interference head waves[2]

In the discussion of interface waves in Sec. 2.3.3, we argued that the fields associated with those waves propagating along the water-bottom interface are due to the saddle point contributions of the multiples. This is true whether the sound velocity at the top of the layer is less than or greater than that of the water column.

However, if the sound velocity profile in the layer approaches a constant and the layer medium becomes identically homogeneous, the physical characteristics of the interface waves become completely different depending on the sound velocity difference at the water-bottom interface. Only when $c_0 < c_1(0)$, do they become the classical head wave associated with a branch cut contribution[5].

It is also of some interest to show analytically that the pole--type singularities from the total Langer reflection coefficient become the branch cut due to the branch point at $1/c_1(0)$ as $c_1(z)$ approaches $c_1(0)$ for all z.

keferences:

[1] Frisk, G. V., Doutt, J. A. and Hays, E. E., "Bottom interaction of low-frequency acoustic signals at small grazing angles in the deep ocean," J. Acoust. Soc. Am., 69, 84-94 (1980).

[2] Frisk, G. V., private communication.

[3] Mook, D. R., "The numerical synthesis and inversion of acoustic fields using the Hankel transform with application to the estimation of the plane wave reflection coefficient of the ocean bottom,", Sc.D. Thesis, MIT/WHOI Joint Program in Oceanography/ Oceanographic Engineering (January 1983).

[4] Mook, D. R., Frisk, G. V. and Oppenheim, A. V., "A Hybrid Numerical/Analytic Technique for the Computation of Wave Fields in Stratified Media Based on the Hankel Transform," to be published in J. Acoust. Soc. Am. (June 1984).

[5] Brekhovskikh, L. M., Waves in Layered Media, 2nd ed., Academic Press, New York, 1980.

Appendix A: Accuracy of The Langer uniform asymptotic approximation

Quantitative error analysis of the Langer uniform asymptotic approximation is discussed in this appendix. We have discussed that $E(z)G(z)$ vanishes asymptotically in Chapter 2. The exact expression for $E(z)$ is given by

$$E(z) = \frac{\Psi''}{\Psi} \tag{A.1}$$

where $$\Psi = Q^{-1/2}\,\eta^{1/6} \tag{A.2}$$

Thus $E(z)$ may be further reduced to

$$E(z) = -\frac{5}{36}\,Q^2\eta^{-2} + \frac{3Q'}{4Q^2} - \frac{Q''}{2Q} \tag{A.3}$$

The condition for the Langer solutions to be valid is

$$\frac{E(z)}{\omega^2 Q^2} \ll 1 \tag{A.4}$$

where the denominator is given by the second term in (2.3).

Substituting (A.3) in (A.4), we obtain

$$\omega^{-2}\left[-\frac{5}{36}\,\eta^{-2} + \frac{3Q'}{4Q^4} - \frac{Q''}{2Q^3}\right] \ll 1 \tag{A.5}$$

When η is very large, i.e. when z is away from a turning point z_t so that

$$\eta = \int_{z_t}^{z} Q(z')\, dz' \gg 1,$$

the above condition may be further reduced to

$$\omega^{-2}\left[\frac{3Q'}{4Q^4} - \frac{Q''}{2Q^3}\right] \ll 1 \qquad (A.6)$$

This is nothing but the error criterion for the WKBJ method[1]. (A.5) and (A.6) are valid only when $Q \neq 0$ and $\eta \neq 0$, and Q' and Q" are not large, i.e. when z is away from z_t in a slowly varying medium.

In order for the Langer solutions given by Eq. (2.7) to be valid anywhere, we must show that Ψ never becomes zero even at the turning point although one might expect such condition by substituting $\eta = 0$ in Eq. (A.2). Let us assume near the turning point that

$$Q^2 = az \qquad \text{as} \qquad z > 0 \qquad (A.7)$$

where $z_t = 0$ is assumed for convenience and a is a constant gradient. Then,

$$\eta = \int_0^z (az)^{1/2}\, dz = \frac{2}{3a}(az)^{3/2}; \qquad Q = (az)^{1/2}$$

Hence becomes

$$\Psi = \left(\frac{2}{3a}\right)^{1/6}$$

which is constant at the turning point, thus E(z) vanishes. Therefore, is non-zero anywhere.

The Langer uniform asymptotic approximation is equivalent to the WKBJ approximation with an Airy function correction for depths near the turning point. However, when the WKBJ method is applied, it is necessary to determine where to switch from the WKBJ solution to the Airy function solution in order to obtain solutions across the turning depth. The greatest advantage of L.U.A.A. is that it provides a general closed form solution valid anywhere without requiring the determination of this boundary and continuously switches one solution type to the other.

It is also important to note that when $Q^2(z)$ is linear everywhere, Ψ is constant and E(z) vanishes entirely, and therefore the L.U.A.A. reduces to the exact solution of (2.1).

References:

[1] Bender, C. M. and Orszag, S. A., Advanced Mathematical Methods for Scientists and Engineers, McGraw-Hill, New York, 1978.

[2] Langer, R. E., "Asymptotic solutions of a differential equation in the theory of microwave propagation," Commun. Pure Appl. Math. 3, 427-438 (1950).

Appendix B: The Modified Method of Steepest Descents for the Sommerfeld Integral with Langer Reflection Coefficients

The method of steepest descents (M.S.D.) is an expansion technique to evaluate asymptotically an integral of the form,

$$I = \int_{-\infty}^{\infty} F(p)\, e^{i\omega\phi(p)}\, dp; \qquad \omega \to \infty \tag{B.1}$$

where

$$F = V_n p^{1/2} \gamma_0^{-1}$$

with

$$V_n = R_n e^{-2i\omega n\mu}$$

where R_n is a partial Langer reflection coefficient defined by Eq. (2.30) and μ is a layer-phase defined by Eq. (2.39).

However, F(p) given by Eq. (2.36) should be written as

$$F = F(p,\omega)$$

because the modified reflection coefficient V_n is a function of p and ω. The reason why we may still apply the basic method of steepest descents technique is that V_n behaves as if it were a function of p alone when its asymptotic behavior for $\omega \to \infty$ (i.e. the dependence of F on ω is very weak). Although we may treat V_n as a function of p alone, it is still important to verify if V'_n and V''_n have the ap-

propriate behavior as a part of the correction term N in Eq. (2.41) so that N/ω asymptotically vanishes as ω approaches infinity[1]. For the simplest example, let us consider the specularly reflected field P_0 and compare its correction term N to that of Lamb's problem studied by Brekhovskikh[2]. Since both share the same phase ϕ, we need only consider the Rayleigh plane wave reflection coefficient given by Eq. (2.31) and the Langer reflection coefficient R_0 in Eq. (2.29). We have already observed that R_0 in Eq. (2.29) may be reduced to Eq. (2.31) when the asymptotic approximations of the Fock functions are substituted, but this is not the case for their derivatives. We shall examine the asymptotic behavior of V'_n and V''_n, and justify the expansion necessary for the method of steepest descents.

First, before we consider the Langer reflection coefficient V_0 ($= R_0$), i.e. the plane wave reflection coefficient for specular reflection, we shall review the leading order behavior of its asymptotic approximation which identically becomes a local plane wave reflection coefficient at the ocean bottom interface given by

$$R_r = \frac{\rho_1 \gamma_0 - \rho_0 Q_0}{\rho_1 \gamma_0 + \rho_0 Q_0} \tag{B.2}$$

whose first derivative with respect to p is given by

$$R'_r = \frac{2\,\rho_0 \rho_1 p}{(\rho_1 \gamma_0 + \rho_0 Q_0)^2} \left(\frac{Q_0}{\gamma_0} - \frac{\gamma_0}{Q_0}\right) \tag{B.3}$$

where the subscript r indicates that this is the Rayleigh reflection coefficient.

Now we differentiate V_0 with respect to p and obtain

$$V_0' = R_0' = \frac{2(A_0^{(2)'}B_0^{(2)} - A_0^{(2)}B_0^{(2)'})}{(A_0^{(2)} + B_0^{(2)})^2} \tag{B.4}$$

which has the leading order asymptotic behavior

$$V_0' \sim \frac{2\rho_0\rho_1 p}{(\rho_1\gamma_0 + \rho_0 Q_0)^2}\left(\frac{\gamma_0}{Q_0} - \frac{Q_0}{\gamma_0} + \frac{\mu' Q_0\gamma_0}{3p\mu}\right) \tag{B.5}$$

The last term within the parenthesis is introduced in addition to the result from Eq. (B.3). Interestingly, when the sound velocity profile in the layer has the form $1/c^2$-linear, the first and third terms exactly cancel out and Eq. (B.5) becomes

$$V_0' \sim -\frac{2\rho_0\rho_1 p}{(\rho_1\gamma_0 + \rho_0 Q_0)^2}\frac{Q_0}{\gamma_0}. \tag{B.6}$$

This could be significantly different from the value given by Eq. (B.3) because the terms within the parenthesis in Eq. (B.3) tend to cancel each other when c_0 and $c_1(0)$ have similar values, and the difference can become a fraction of the order of each term. In any case Eq. (B.6) is still independent of ω and behaves well in the correction term N.

We shall next consider the second derivative of V_0,

$$\frac{V_0''}{V_0} = \frac{2\,(A_0^{(2)''}B_0^{(2)} - A_0^{(2)}B_0^{(2)''})}{A_0^{(2)2} - B_0^{(2)2}} - \frac{V_0'}{V_0}\,\frac{2\,(A_0^{(2)'} + B_0^{(2)'})}{A_0^{(2)} + B_0^{(2)}} \qquad (B.7)$$

where $A_0^{(2)}$, $B_0^{(2)}$, $A_0^{(2)'}$ and $B_0^{(2)'}$ are given by Eqs. (2.21-22), (2.51-52), respectively. Also $A_0^{(2)''}$ and $B_0^{(2)''}$ are given by

$$A_0^{(2)''} = -i\rho_1[(\frac{1}{c_0^2\gamma_0^3} + \gamma_0\nu_0\nu_0'^2)\,W^{(1),(2)}(\nu_0) + (\gamma_0\nu_0'' - \frac{2p}{\gamma_0}\nu_0')\,W'^{(1),(2)}(\nu_0)] \qquad (B.8)$$

$$B_0^{(2)''} = -\rho_0[2\,S_0'\nu_0\nu_0' + S_0\nu_0'^2 + S_H\,\nu_0\nu_0'']\,W^{(1),(2)}(\nu_0) + [S_0'' - S_0\nu_0\nu_0'^2]\,W'^{(1),(2)}(\nu_0) \qquad (B.9)$$

Again, after substituting the asymptotic approximations of the Fock functions in Eq. (B.7), we obtain

$$V_0'' \sim -\frac{2\rho_0\rho_1 p}{(\rho_1\gamma_0 + \rho_0 Q_0)^3}\,[(\rho_1\gamma_0 + \rho_0 Q_0)\,\frac{Q_0}{pc_0^2\gamma_0^3} - \frac{2i\rho_1 pQ_0}{\gamma_0^2} - 2\omega\eta'(i\rho_0\gamma_0 + (1-i)\rho_1 Q_0 + \frac{i\rho_1\gamma_0^2}{Q_0})] \qquad (B.10)$$

where there is a term ω which leads to the violation of the criterion imposed for the asymptotic expansion given by Eq. (2.42). In an analogous manner, one can show that asymptotically V_n' is independent of ω while V_n'' depends on ω for $n > 0$.

The direct cause of this problem is due to the mathematical property of the Airy functions A which satisfy the Airy equation

$$\frac{d^2A(x)}{dx^2} = x\, A(x) \tag{B.11}$$

where x contains the term dependent on ω. As the terms in V_n containing the Airy functions are differentiated twice, these quantities appear in the asymptotic form of V_n without being canceled out. Thus, unfortunately, a direct application of the M. S. D. fails at the inclusion of the second derivative of the Langer reflection coefficient.

However, we know that V_n is a very slowly varying function of p and it would not make much physical sense to expect a large value from the second derivative of V_n with respect to p compared to the first derivative. We also know that in practice, the major source of limitation of the M. D. S. is due to a large value of V'_n which is the only place where V''_n could be appreciably large (ex. the Langer reflection coefficient at critical incidence). All of the above suggests that the basic approach of the M. S. D. is still valid. We, therefore, set V''_n to zero, which is equivalent to limiting the Taylor expansion of F in Eq. (2.41) to somewhat lower order by rewriting the truncated series as

$$F(p) \cong F(p_s) + F'(p_s)(p - p_s) + \frac{1}{2}[V_n'(\frac{2p_s^{3/2}}{\gamma_0^3} + \frac{1}{p_s^{1/2}\gamma_0})$$

$$+ V_n p_s^{1/2}\gamma_0^{-1}(2\gamma_0^{-2} + \frac{3p_s^2}{\gamma_0^4} - \frac{1}{4p_s^2})](p - p_s)^2 \qquad (B.12)$$

We note that F" in Eq. (2.48) is the coefficient of $(p - p_s)^2$ in the above expansion.

Reference:

[1] Bender, C. M. and Orszag, S. A., Advanced Mathematical Methods for Scientists and Engineers, McGraw-Hill, New York, 1978.

[2] Brekhovskikh, L. M., Waves in Layered Media, 2nd ed., Academic Press, New York, 1980.

Appendix C: Asymptotic approximation of Fock functions

Asymptotic expansions of Fock functions are derived in this appendix as follow:

$$W^{(1),(2)}(\nu) = Ai(-\nu) \mp i\, Bi(-\nu)$$

$$= (\nu/3)^{1/2} e^{\pm i\pi/6} H_{1/3}^{(1),(2)}(x) \qquad (C.1a,b)$$

$$\sim (2\nu/3\pi x)^{1/2} e^{\pm i(x - \pi/4)}$$

$$= \nu^{-1/4} \pi^{-1/2}\, e^{\pm i(x - \pi/4)} \qquad (C.2a,b)$$

$$W'^{(1),(2)}(\nu) = \frac{dAi(-\nu)}{d(-\nu)} \mp i\frac{dBi(-\nu)}{d(-\nu)}$$

$$= -\frac{\nu}{3^{1/2}}\, e^{\mp i\pi/6} H_{2/3}^{(1),(2)}(x) \qquad (C.3a,b)$$

$$\sim -\nu(2/3\pi x)^{1/2} e^{\pm i(x - 3\nu/4)}$$

$$= -\nu^{1/4}\, \pi^{-1/2}\, e^{\pm i(x - \pi/4)} \qquad (C.4a,b)$$

where $\nu = (\frac{3}{2} x)^{2/3}$

The regions of validity of the argument x are

$$-\pi < \arg x < 2\pi \qquad \text{for the first kind, (1)}$$

$$-2\pi < \arg x < \pi \qquad \text{for the second kind, (2)}$$

Reference:

Abramowitz, M. and Stegun, I. A., Handbook of Mathematical Functions, Natl. Bur. Stand. Appl. Math. Ser. 55, Washington, D. C., 1964, Eqs. (10.4.23), (10.4.24), (10.4.28), (10.4.29), (9.2.3) and (9.2.4).

Appendix D: Approximation of Hamilton's Profile

Sound velocity profiling in ocean bottom sediments from sonobuoy data is given in terms of the one-way travel time t of a pulse signal penetrating through the bottom structures. It has been found from measurements that the depth z may be expressed by the third order polynomial in t as[1]

$$z = At + Bt^2/2 + Ct^3/3. \tag{D.1}$$

By differentiating both sides, we obtain sound velocity v in t given by

$$v = dz/dt = A + Bt + Ct^2. \tag{D.2}$$

Unlike the case where z is a quadratic function of t[2], it is not possible to eliminate t from the above equations to obtain v as a function of z. Hamilton does provide an expression for sound velocity as a function of depth which is the result of a regression of points generated by the above equations for many values of t and is expressed by third order polynomials[1]. However, it is not in a form for which the phase integral and ray equations(travel time, intensity, etc.) can be computed analytically.

In this appendix we shall introduce an approximate method to obtain a simple analytic depth dependent expression for the sound velocity from which these analytical expressions can be obtained

easily[3]. The results of this simple velocity function are accurate enough to model ocean bottom sound velocity structure based on the measurements.

We first propose the following quadratic function in z versus sound velocity V to the third power:

$$V^3 = \alpha + \beta z + \gamma z^2 \qquad (D.3)$$

The above expression for V has been chosen because the shape of V is similar to that of Hamilton's profile. We have also assumed 3 unknown coefficients, α, β and γ, to be consistent with the 3 parameters given in (D.1) and (D.2) though it will be shown later that the last term on the right hand side may be dropped without sacrificing much accuracy. As a result, the ray equations and the phase integral can be expressed in simple analytic forms as given in Sec. 3.1.

After we substitute z given by (D.1) in (D.3) and retain terms through t^2, (D.3) becomes

$$V^3 \cong \alpha + \beta\, At + (\beta\, B/2 + \gamma\, A^2)t^2. \qquad (D.4)$$

Since A, B and C are on the order of unity[1] and t is typically less than 1 sec, and α, β and γ are also on the order of unity (which will be verified shortly), V given by (D.4) is a good approximation to Eq. (D.3).

We next cube both sides of (D.2) and compare the coefficients of each order of t, and finally obtain

$$\alpha = A^3$$

$$\beta = 3AB$$

$$\gamma = 3(C + B^2/2A).$$

From the example given by Hamilton of terrigenous sediments whose instantaneous velocity in km/sec is given by the form of (D.2) with A = 1.511, B = 1.041 and C = -0.372 (Table III of Ref. 1), we get α = 3.450, β = 8.989, γ = 1.630. From these numbers it can be easily shown that the higher order terms of t which have been neglected in (D.4) are in fact much smaller than the rest.

Furthermore, since z is typically less than 1 km, the z^2-term may be dropped in (D.3) and we finally obtain

$$V^3 = \alpha + \beta z \qquad (D.5)$$

When z is .1 km, V computed from (D.5) has less than 0.2% error compared to Hamilton's formula, and even at z = 1 km where the maximum error is expected, it has less than 1% error. Hamilton's profile and (D.5) are plotted in Fig. D.1.

References:

[1] Hamilton, E. L., "Geoacoustic modeling of the sea floor," J. Acoust. Soc. Am., 68(5), 1313-1340 (1980).

[2] Houtz, R. E. and Ewing, J. I., "Detailed Sedimentary Velocities from Seismic Refraction Profiles in the Western North Atlantic," J. Geophys. Res., 68(18), 5233-5258 (1963).

[3] Kawahara, H. and Frisk, G. V., "A canonical ocean bottom sound velocity profile," (Submitted to J. Acoust. Soc. Am.)

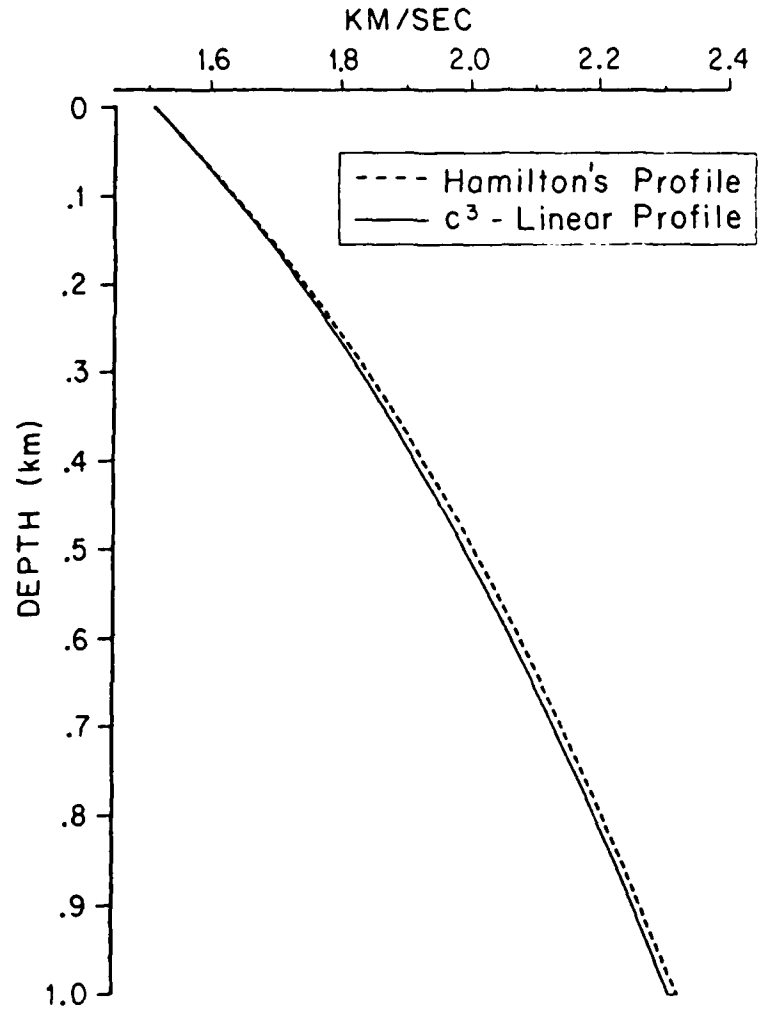

Fig. D.1 A comparison between Hamilton's profile and c^3-linear profile for terrigenous sediments (cf. Table III of Ref. 1).

50272-101

REPORT DOCUMENTATION PAGE	1. REPORT NO. WHOI-84-23	2. A144449	3. Recipient's Accession No.

4. Title and Subtitle
Asymptotic Analysis of Ocean Bottom Reflected Acoustic Fields

5. Report Date
May 1984

6.

7. Author(s)
Hiroshi Kawahara

8. Performing Organization Rept. No.
WHOI-84-23

9. Performing Organization Name and Address
Woods Hole Oceanographic Institution
Woods Hole, Massachusetts 02543 and
Massachusetts Institute of Technology
Cambridge, Massachusetts 02139

10. Project/Task/Work Unit No.

11. Contract(C) or Grant(G) No.
(C) N00014-82-C-0152
(G)

12. Sponsoring Organization Name and Address
Office of Naval Research
Environmental Sciences Directorate
Arlington, Virginia 22217

13. Type of Report & Period Covered
Ph.D. Thesis

14.

15. Supplementary Notes
This thesis should be cited as: Hiroshi Kawahara, 1984. Asymptotic Analysis of Ocean Bottom Reflected Acoustic Fields. Ph.D. Thesis. MIT/WHOI, WHOI-84-23.

16. Abstract (Limit: 200 words)

Pronounced spatial acoustic interference patterns versus horizontal range were observed near the deep ocean bottom from a 220-Hz CW point source also located near the bottom. This is a result of the direct water wave field interacting with a strongly reflected field from the ocean sediments. If the bottom structures are horizontally stratified media, the reflected field can be expressed by the Sommerfeld integral whose integrand is weighted by a total plane wave reflection coefficient.

In this thesis the reflected fields are analytically evaluated in order to understand the physical mechanism of the propagating waves through the bottom layer structure. Based on a canonical geoacoustic model, the Langer uniform asymptotic approximation is applied to evaluate the total plane wave reflection coefficient accurately. Then the Sommerfeld integral is evaluated by the method of steepest descents. The expression for the reflected field is fully analytic and provides physical insight into the understanding of energy partitioning in the sediments. With inclusion of the new method to analytically express a sound velocity profile shape based on measurements, the approximate solution provides a full analytic expression of the reflected field based on a realistic geoacoustic model.

Various geoacoustic models, with emphasis on changes in the shape of the sound velocity profile in the sediment layer, are examined and their parametric dependences on the associated reflected fields are investigated. The conditions necessary for the shape of the profile to be important are also quantitatively defined and are demonstrated in theoretical data as well as in real data.

17. Document Analysis a. Descriptors

1. bottom acoustics
2. acoustic reflection
3. asymptotic analysis

b. Identifiers/Open-Ended Terms

c. COSATI Field/Group

18. Availability Statement:	19. Security Class (This Report)	21. No. of Pages
Approved for publication; distribution unlimited.	UNCLASSIFIED	177
	20. Security Class (This Page)	22. Price

END

FILMED

DTIC